EUSKAL HERRIKO U NIBERTSITATEA - UNIVERSIDAD DEL PAIS VASCO
MATERIALEN FISIKA SAILA - DEPARTAMENTO DE FÍSICA DE MATERIALES

Infrared nanospectroscopy and hyperspectral nanoimaging of organic matter

Iban Amenabar Altuna

- PhD Thesis -

Thesis supervisor
Prof. Rainer Hillenbrand

2017

(c)2017 IBAN AMENABAR ALTUNA

This PhD thesis has been conducted in CIC NanoGUNE

by

Iban Amenabar Altuna

1 Summary

Infrared spectroscopy is a highly valuable tool for materials characterization in widely different fields, ranging from polymer sciences to biomedical imaging. When interacting with matter, infrared light can excite, for example, molecular and crystal vibrations and consequently gets absorbed, which allows for highly sensitive spectroscopic studies of chemical and structural properties. Most of the vibrational excitations are found in the so-called "finger-print" region of the infrared spectrum, which spans from 5 to 20 μm wavelength (corresponding to 400-2000 wavenumbers [cm^{-1}]).

The standard technique for measuring the infrared response of materials in a broad range of frequencies is Fourier transform infrared (FTIR) spectroscopy, which will be briefly introduced in chapter 3 of this thesis. However, diffraction limits the spatial resolution of FTIR spectroscopy, thus preventing the study of nanoscale materials and composites, as well as of single biological macromolecules.

One solution to achieve nanoscale resolved infrared imaging is scattering-type scanning near-field optical microscopy (s-SNOM). It is the only imaging technique that provides wavelength-independent resolution in the order of 20 nm, which has been demonstrated with visible, infrared and THz radiation. In chapter 4 of this thesis the basic principles of s-SNOM will be introduced. It is typically based on atomic force microscopy (AFM), where the tip is illuminated with a focused monochromatic laser beam. Simultaneously to topography, the radiation backscattered by the tip is detected interferometrically, that is, both amplitude and phase of the scattered light are recorded. When the tip is brought into contact or very close to a sample, the strong optical near-field interaction between the tip and sample modifies the backscattered radiation, allowing for probing the local complex-valued dielectric properties of the sample.

In order to obtain local spectral information, Fourier transform infrared nanospectroscopy (nano-FTIR) has recently been introduced. It combines the nanoscale spatial resolution of s-SNOM with the analytical power of FTIR spectroscopy. The basic principles of nano-FTIR will be introduced in chapter 5 of this thesis. In nano-FTIR, the s-SNOM tip is illuminated by broadband infrared radiation from a thermal source, infrared laser supercontinuum, or synchrotron. Fourier transform spectroscopy of the backscattered light is performed, yielding local infrared amplitude and phase spectra (i.e. nano-FTIR spectra) of the sample surface with a spatial resolution of about 20 nm. It has been shown that nano-FTIR phase spectra of organic materials can be well interpreted with the help of far-field FTIR absorbance spectra, allowing for materials characterization and identification based on standard infrared references. However, nano-FTIR is a relatively new technique and its suitability and applicability in many specific application fields has not been explored yet. For instance, although conventional FTIR spectroscopy is widely used to analyze protein morphology and secondary structure, broadband nano-FTIR spectra of protein complexes had not been studied before this thesis.

In chapter 6 we demonstrate that nano-FTIR can probe protein secondary structure on the nanometer scale and with sensitivity to individual protein complexes. To this end, we have chosen to study the amide bands of individual tobacco mosaic viruses (TMVs) and ferritin complexes for their well-defined, robust and dominantly α-helical protein structure, insulin aggregates for exhibiting β-sheet structure and purple membranes (PMs) because of the well-defined orientation of the transmembrane α-helices. On the TMV and ferritin samples, we verify the ability of nano-FTIR to measure nanoscale broadband infrared spectra of the amide I and II bands over the range from 1400 to 1800 cm^{-1}. In particular, IR spectra of a ferritin complex indicate that nano-FTIR is sensitive to about 4000 amino acids, corresponding to about 5000 C=O and N-H bonds, respectively. Furthermore, the spectra recorded on PM, show that nano-FTIR primarily probes molecular vibrations that oscillate perpendicular to the sample surface, with a spatial resolution of about 30 nm and high reproducibility. Most importantly, we found that the amide I band in the nano-FTIR spectra can be analyzed and interpreted in the framework of standard infrared spectroscopy. We demonstrate the biological application potential of nano-FTIR by exploring the still not fully clarified protein conformation in individual insulin fibrils. We find clear evidence that 3-nm-thin amyloid-like fibrils contain a large amount of α-helical structure.

To gain further insights into the structure of the samples, spectroscopic information at each pixel of an image is desirable, that is hyperspectral imaging. In chapter 7 we introduce hyperspectral infrared nanoimaging by nano-FTIR with a tunable difference frequency generation (DFG) laser continuum , and describe the key implementations of the technique. For hyperspectral nanoimaging we record a 2D array of nano-FTIR spectra with a spectral bandwidth determined by the output spectrum of the DFG laser continuum (about 400 cm^{-1} effective bandwidth), that is, a hyperspectral data cube. To increase the spectral bandwidth, we record data cubes at three different DFG output spectra and stitch together at each pixel the corresponding normalized nano-FTIR spectra. This is enabled by sample drift correction during the spectra acquisition. As a result, a broadband hyperspectral data cube is obtained. We succeeded to obtain about 400 cm^{-1} broad nano-FTIR spectra of organic materials in 1.66 seconds, which allowed us for the first time to record nanoscale-resolved hyperspectral infrared images comprising about 5000 nano-FTIR spectra that cover a spectral range from 1000 to 1900 cm^{-1} in about 7.5 hours.

Having developed the hyperspectral infrared nanoimaging technique, in chapter 8 we demonstrate its application potential with a polymer blend and a human hair cross-section. We demonstrate that in combination with multivariate data analysis, hyperspectral infrared nanoimaging provides nanoscale-resolved chemical and compositional maps, yielding valuable insights into the spatial distribution of polymers. More important, it enables the identification and spatial mapping of nanoscale-size areas where chemical interactions between polymers occur. Furthermore, our studies of a hair cross-section demonstrate the capacity of hyperspectral infrared nanoimaging to identify and chemically analyze melanin molecules within their granula, without requiring deleterious extraction or tagging processes.

In conclusion, within this thesis we establish a solid foundation for infrared nanobiospectroscopy, which is a prerequisite for nano-FTIR applications in biochemical and biomedical research. Further, we introduce broadband hyperspectral infrared nanoimaging, which in combination with multivariate data analysis yields nanoscale-resolved chemical and compositional maps, including the detection of nanoscale localized chemical interaction. We foresee a wide application potential of hyperspectral infrared nanoimaging in various fields of science and technology, ranging from materials sciences and pharmaceutical applications to biomedical imaging, and from fundamental research to quality control.

2 Laburpena

Infragorriko (IR) espektroskopia oso tresna erabilgarria da materialen karakterizaziorako eta horregatik arlo desberdinetan erabiltzen da, esate baterako polimeroen zientzian edo eta aplikazio biomedikoetan. Materialarekin elkar-eragiterakoan, argi infragorriak bibrazio molekularrak kitzika ditzake eta ondorioz materialak argi infragorria xurgatzen du. Xurgapen honek, ezaugarri kimiko eta estrukturalen inguruko azterketa espektroskopiko oso sentsibleak egitea ahalbidetzen du. Bibrazio molekular gehienak espektroaren infragorriko eskualde konkretu batean aurkitzen dira, zein "hatz marken eskualdea" ("finger-print region") bezala ezagutzen den. Eskualde hau, 5 eta 20 μm uhin luzeren artean aurkitzen da (400-2000 cm^{-1}, uhin zenbakien artean).

Materialen argi infragorriarekiko erantzuna frekuentzia espektro zabal batean neurtzeko teknika estandarra Fourier-en transformatuaren infragorriko (FTIR) espektroskopia da. Teknika hau, tesi honetako 3 kapituluan aurkeztuko da. Alabaina, difrakzioak FTIR espektroskopiaren bereizmen espaziala mugatzen du, nanoegituren nahiz makromolekula biologiko indibidualen azterketa optikoa eragotziz.

Nanoeskalako infragorriko irudiak lortzeko soluzio bat sakabanaketa motako eremu-hurbileko eskaneatze mikroskopio optikoa (s-SNOM) da. Teknika honek 20 nm inguruko bereizmen espaziala eskaintzen du. Honetaz gain, uhin luzerarekiko independentea den bereizmen espaziala ematen duen teknika bakarra da eta Terahertzioetako argiarekin nahiz argi ikuskor eta infragorriarekin frogatua izan da. s-SNOM teknikaren oinarrizko printzipioak tesi honetako 4 kapituluan aurkeztuko dira. Teknika hau, normalean indar atomikozko mikroskopian (AFM) oinarritzen da, non AFM punta, fokatutako infragorriko argi monokromatiko batez argiztatua den. Topografiarekin batera, puntak bueltan sakabanatutako argia interferometria bidez detektatzen da, hau da, sakabanatutako argiaren anplitudea nahiz fasea grabatzen dira. Punta laginetik oso gertu edo laginarekin kontaktuan jartzen denean punta eta laginaren arteko eremu hurbileko elkarrekintza optiko indartsuak sakabanatutako irradiazioan eragina dauka. Honek laginaren balio konplexuko ezaugarri dielektriko lokala neurtzea ahalbidetzen du.

Espektro-informazio lokala lortzeko, orain gutxi Fourier-en transformatuaren infragorriko nano-espektroskopia (nano-FTIR) garatu da. Teknika honek, s-SNOM-aren bereizmen espazial nanometrikoa eta FTIR espektroskopiaren ahalmen analitikoa uztartzen ditu. Nano-FTIR teknikaren oinarrizko printzipioak tesi honen 5 kapituluan aurkeztuko dira. Nano-FTIR teknikan, s-SNOM punta espektro zabaleko irradiazio infragorriaz argiztatzen da. Irradiazio mota hau, iturri termiko batetatik, infragorriko laser jarraitu batetatik, nahiz sinkrotroi batetatik lor daiteke. Puntak sakabanatutako argiaren Fourier-en transformatuaren espektroskopia eginez laginaren infragorriko anplitudearen eta fasearen espektro lokala lortzen da. Hau nano-FTIR espektroa deitzen da, eta 20 bat nm-tako bereizmen espaziala dauka. Frogatua izan da, material organikoen nano-FTIR espektroak ezagunak eta oso erabiliak diren FTIR xurgatze espektroekin alderatuta interpreta daitezkeela. Honek nano-FTIR bidezko materialen

identifikazioa eta karakterizazioa ahalbidetzen du FTIR espektro estandarrak erreferentziatzat hartuta. Alabaina, nano- teknika berri bat izaki, nano-FTIR-aren balioa eta erabilgarritasuna aplikazio eremu askotan oraindik ez da ikertu. Adibidez, FTIR espektroskopia oso erabilia den arren proteinen morfologia nahiz bigarren mailako egitura aztertzeko, proteinen nano-FTIR espektroa tesi hau burutu arte ez zen inoiz neurtu eta aztertu.

6 kapituluan nano-FTIR teknikak proteinen bigarren mailako egitura eskalan nanometrikoan eta proteina konplexu bakar bateko sentsibilitateaz neur dezakeela frogatzen dugu. Honetarako ondorengo nanoegituren amide xurgatze bandak aztertu ditugu: tabako mosaikoaren birusa (TMV) eta ferritina konplexuak, nagusiki α-helize erakoa den ongi definitutako egitura dutelako, intsulina agregatuak, β-xafla egitura dutelako eta mintz morea (PM), bere α-helizeek ongi definitutako orientazioa dutelako. TMV eta ferritina laginetan nano-FTIR teknikak amide I eta II bandak neurtzeko balio duela egiaztatu dugu 1400 cm^{-1} eta 1800 cm^{-1} bitarteko nano-FTIR espektroa neurtuaz. Ferritina konplexu bakar batean neurtutako IR espektroak frogatu du nano-FTIR teknikak 4000 aminoazido baino ez dituen proteina konplexu bat neurtzeko adinako sentsibilitatea duela, hau da, 5000 C=O eta N-H lotura inguru. Honetaz gain, mintz morean neurtutako espektroek erakusten dutenez, nano-FTIR teknikak laginaren gainazalarekiko elkarzut oszilatzen duten bibrazio molekularrak detektatzen ditu, 30 nanometrotako bereizmen espazialaz eta erreproduzigarritasun handiaz. Aipagarria da, neurtutako nano-FTIR espektroak infragorriko espektroskopiaren testuinguruan interpretatuak eta analizatuak izan daitezkeela erakutsi dugula. Bukatzeko, aplikazio biologikoetarako nano-FTIR teknikak duen potentziala frogatu asmoz, oraindik guztiz ondo ulertzen ez den intsulina zuntzexken egitura aztertu dugu. Azterketa honetan, 3 nm-tako zuntzexkek α-helize erako egitura kantitate handia dutela erakutsi da.

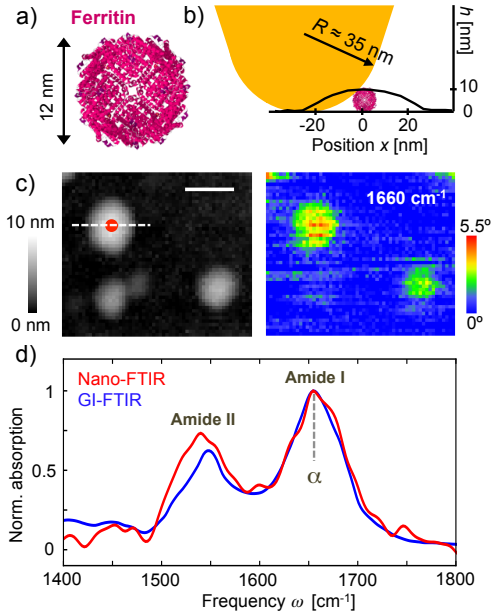

1 irudia: **Ferritina konplexu indibidualen infragorriko nanoespektroskopia**. **(a)** Ferritinaren proteina egituraren ilustrazioa. **(b)** Ferritina partikula baten punta bidezko eskaneatzearen ilustrazioa. Grafikoak puntak 1c irudian markatutako etenkako marran zehar neurtutako altuera profila *h* erakusten du. **(c)** Siliziozko substratuan pausatutako bi ferritina partikulen eta ferritinaz inguratu gabeko nukleo baten topografia eta infragorriko eremu hurbileko fasearen irudia φ. Eskala barra, 50 nm. **(d)** Ferritinaren nano-FTIR espektroa (gorria, 1a irudiko puntu gorrian neurtua) eta arraseko-FTIR (GI-FTIR) xurgatze espektroa.

Laginen egituraren inguruan xehetasun gehiago jakiteko, irudi batetako pixel bakoitzean informazio espektroskopikoa edukitzea garrantzitsua da. Hau hiperespektroskopia bezala ezagutzen da. 7 kapituluan nano-FTIR teknikan oinarritutako nanoeskalako infragorriko hiperespektroskopia aurkezten dugu, non frekuentzia desberdintasuneko sorketa (DFG) bidez lortutako laser jarraitu bat erabiltzen den. Nanoeskalako infragorriko hiperespektroskopia aurkezteaz gain, berau posible egin duten funtsezko garapen teknikoak ere deskribatuko ditugu. Hiperespektroskopiako irudiak lortzeko, nano-FTIR espektroz osatutako bi dimentsiotako matrize bat neurtzen dugu, hau da, datu kubo hiperespektrala. Datu kubo honetako nano-FTIR espektroen banda zabalera DFG laserraren espektroak zehazten du (400 cm^{-1} ingurukoa). Banda zabalera handitzeko, hiru datu kubo neurtu ditugu DFG laserraren hiru espektro desberdinekin, eta pixel bakoitzean dagokion hiru nano-FTIR espektroak batean itsatsi ditugu. Itsasketa hau ahalbidetzeko, laginaren noraezeko berezko mugimendua behin eta berriz zuzentzen dugu datu kuboak neurtzerakoan. Horrela, banda zabaleko data kubo hiperespektral bat lortzen da. Tesi honetan, material organikoetan 400 cm^{-1} inguruko banda zabalera duen nano-FTIR espektroa neurtzea lortu dugu 1.66 segundotan. Honek, 5000 bat nano-FTIR espektroz osaturiko nanoeskalako irudi infragorri hiperespektralak 7.5 ordutan neurtzea ahalbidetu digu. Neurtutako espektroek 1000 cm^{-1}-tik 1900 cm^{-1}-rako banda zabalera dute.

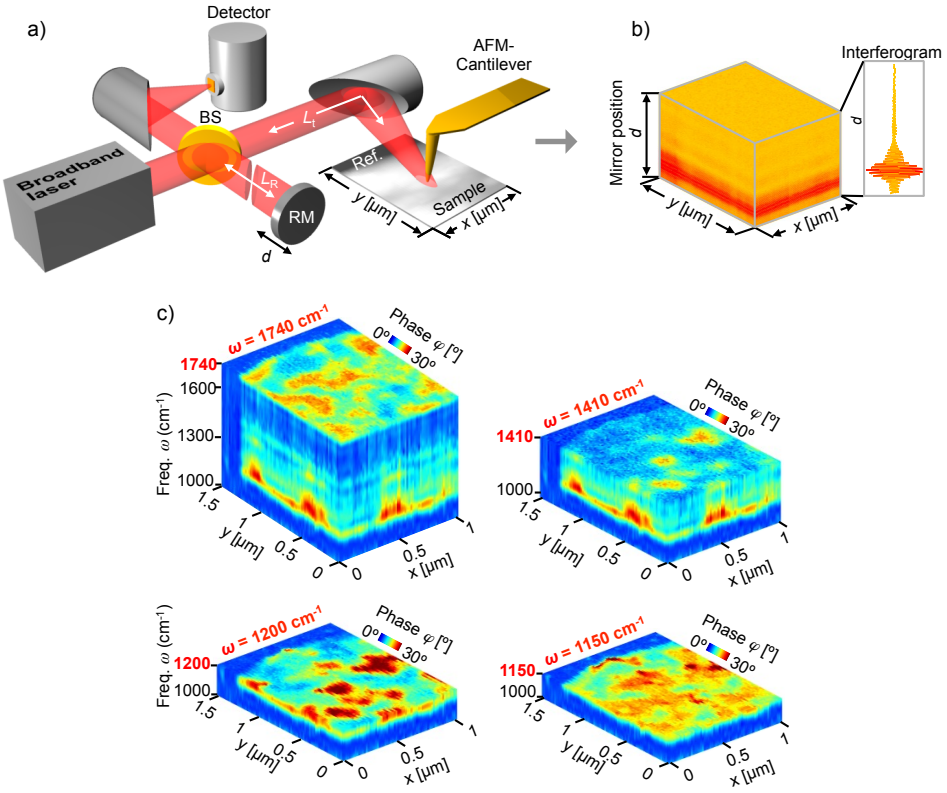

2 irudia: **Nanoeskalako infragorriko hiperespektroskopia. (a)** Konfigurazio esperimentala, non puntaren argiztapenerako infragorri ertaineko laser jarraitu bat erabiltzen den. Puntak laginaren gainazala eskaneatzen du. Bien bitartean, pixel bakoitzean puntatik sakabanatutako argia aztertzen da. Konfigurazioak izpi zatitzaile bat (BS), erreferentzia ispilu bat (RM) eta detektagailu bat dauzka. **(b)** Interferogramaz osatutako bi dimentsiotako matrizea. **(c)** Infragorriko datu kubo hiperespektrala, frekuentzia ω desberdinetan moztua.

Behin nanoeskalako infragorriko hiperespektroskopia garatuta, 8 kapituluan bere aplikazio potentziala frogatzen dugu, horretarako polimero nahasketa bat eta giza ilearen sekzio bat aztertuaz. Aldagai anitzeko datu analisiarekin konbinatuz, nanoeskalako infragorriko hiperespektroskopia bidez mapaketa nanometriko kimiko eta konposizionala posible dela frogatzen dugu. Honek, polimeroen banaketa espazialaren inguruko xehetasun baliagarriak ematen ditu. Gainera, polimeroen arteko elkarrekintza kimikoa gertatu deneko nanoeskalako tamaina duten areak identifikatu eta kokatzen ditu. Bestalde, giza ilearen sekzioan egindako analisiei esker nanoeskalako infragorriko hiperespektroskopiak melanina aletxoak identifikatu eta kimikoki aztertzeko gaitasuna duela frogatzea lortu da, erauzketa narriatzaile eta markatze prozesurik gabe.

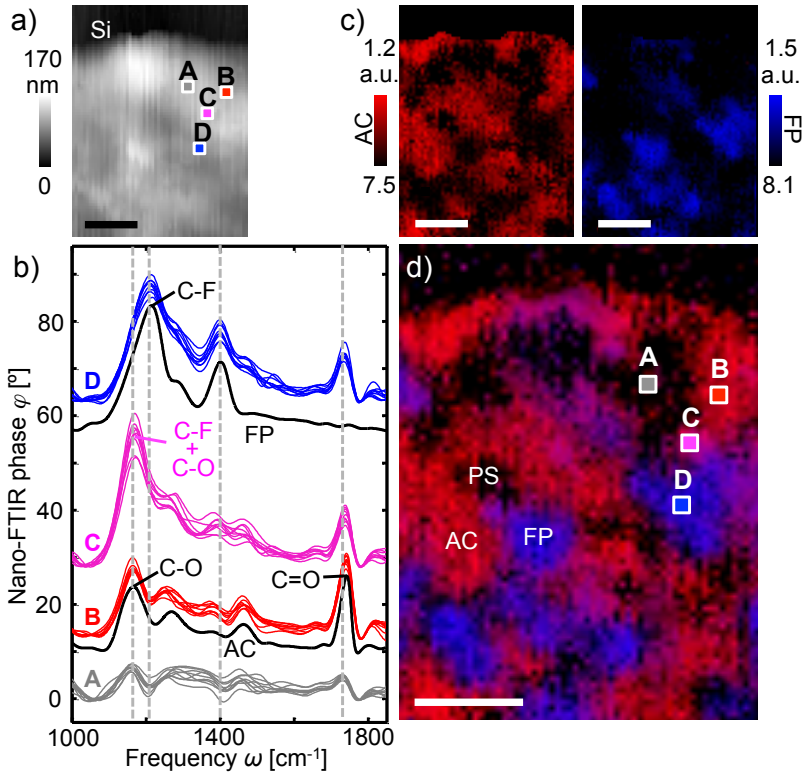

3 irudia: **Hiru osagaitako polimero nahasketa baten nanoeskalako mapaketa kimikoa**. **(a)** Laginaren topografia. **(b)** Kurba beltzek fluorrezko kopolimeroz (FP) eta kopolimero akrilikoz (AC) osatutako erreferentzia laginen nano-FTIR espektroa erakusten dute. Kolorezko kurbak 3a eta 3d irudietan A, B, C eta D letrekin markatutako areatako 9 nano-FTIR espektro erakusten dituzte, denak 2c iruditik atereak. Espektro guztiak bertikalki desplazatuak daude. **(c)** FP eta AC-ren mapaketa espaziala. (d) 3c irudian erakutsitako mapaketa espazialen gainjartze bidez lortutako mapaketa konposizionala. Eskala barra guztiak, 50 nm.

Laburbilduz, tesi honetan infragorriko nanoespektroskopiarako oinarri sendoak ezarri ditugu. Hau derrigorrezko pauso bat da nano-FTIR teknika ikerkuntza biokimiko edo biomedikoetan erabiltzeko. Honetaz gain, nanoeskalako banda zabaleko infragorriko hiperespektroskopia aurkeztu dugu, zeinek aldagai anitzeko datu analisiarekin konbinatuz, nanoeskalako mapaketa kimiko eta konposizionala ahalbidetzen duen; adibidez, elkarrekintza kimiko lokalizatuen mapaketa. Nanoeskalako infragorriko hiperespektroskopiak arlo askotan aplikazio potentzial handia izango duela aurreikusten dugu, hasi materialen zientziatik eta aplikazio farmazeutiko nahiz biomedikoetaraino.

3 Introduction to Fourier transform infrared (FTIR) spectroscopy

In this chapter infrared spectroscopy will be introduced and the Fourier transform infrared (FTIR) spectroscopy technique will be described, which is one of the most widely used techniques to measure infrared spectra. A Michelson interferometer, which is the core of most FTIR spectrometer setups, will be introduced as well as the key processing steps (i.e. apodization, zero-filling, Fourier transformation, normalization) involved in the experimental formation of infrared spectra. Furthermore, the different FTIR spectroscopy techniques and their singularities will be briefly introduced.

3.1 Introduction

In infrared (IR) spectroscopy the infrared region of the electromagnetic spectrum is used (see Fig. 3.1), that is light with lower energy than visible light, to analyze a wide range of material properties [1], [2].Importantly, the photon energies at this part of the spectrum match with the vibrational energies of molecules in a material. Thus, when interacting with matter, infrared light efficiently excites molecular vibrations on the material and gets absorbed providing chemical information about the material.

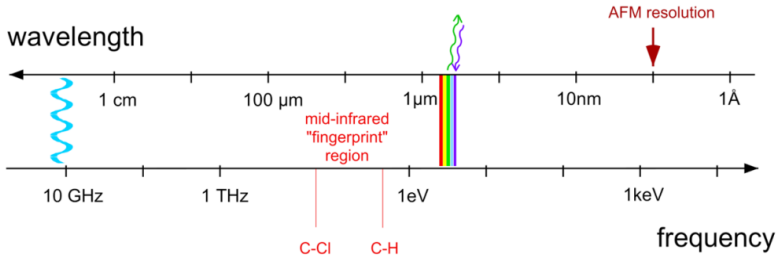

Fig. 3.1: **Electromagnetic Spectrum**. The mid-infrared part is also called the “fingerprint region”, because many materials exhibit unique vibrational modes in this frequency range, which can be exploited for material identification and characterization. Taken from [3].

In infrared spectroscopy, broadband infrared light is used to illuminate a material and the transmitted or reflected light is recorded with a spectrometer. Due to light-matter interaction, the recorded spectrum shows which frequencies have been absorbed and how much. The atoms in a molecule can vibrate in several different ways (different combinations of relative translational and rotational motion), which are called vibrational modes. As most materials consist of many different atoms, several

characteristic vibrational modes are usually excited by infrared light. Thus, infrared absorption spectra are usually very complex and provide a unique so-called "infrared fingerprint" of a material. Interestingly, nowadays huge databases of infrared spectra are available, which allow for the identification of unknown substances by simply comparing their spectra with the spectra in databases.

One of the most common techniques to perform infrared absorption spectroscopy is Fourier transform infrared (FTIR) spectroscopy, which allows for measuring the infrared absorption in a broad range of frequencies. In this chapter, we describe the working principle and theoretical background of FTIR spectroscopy, conceptually following the description of the book *Fourier Transform Infrared Spectrometry* [4]. We also briefly describe the most common experimental configurations of FTIR spectroscopy.

3.2 Michelson interferometer

The core of a FTIR spectrometer is an interferometer, which is typically a Michelson interferometer (originally introduced in 1891 by Michelson [5], [6]). In the following we will describe how a basic Michelson interferometer [7] is used to record infrared spectra. The simplest design of a Michelson interferometer is shown in Fig. 3.2.

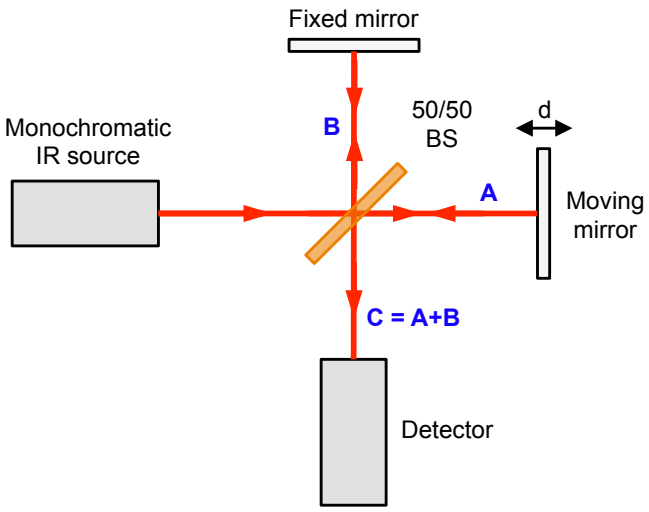

Fig. 3.2: **Michelson Interferometer**. A collimated beam emitted from a light source is split by a beamsplitter (BS) in two equal beams. One beam (B) is reflected at the BS and the other beam (A) is transmitted. Both beams are back-reflected on two independent planar mirrors and they are superpositioned at the BS (C). The beam C is focused onto a detector.

The incident beam of light emitted by the source is split by the beamspliter (BS) into two beams, one is transmitted through the BS (beam A) and the other one is reflected (beam B). After following different paths and back-reflecting on two independent planar mirrors, the two beams are superpositioned at the beamsplitter. The resulting beam finally hits the detector and its intensity is measured. One of the mirrors is fixed (marked as "fixed mirror" in Fig. 3.2), while the other mirror (marked as "moving mirror" in Fig. 3.2, usually referred as reference mirror) is moved (along the beam direction) creating a path difference, Δd, between the two arms of the interferometer. The optical path difference (OPD) due to the path difference Δd is called the *retardation*, δ, and is given by $\delta = 2\Delta d$. By changing the retardation δ, the interference between the two beams (A and B) leads to a variation of the intensity measured at the detector. This intensity variation is measured as a function of the retardation to form the so-called interferogram, from which the output spectrum of the incident light can be obtained as shown in detail in the following.

Let us first consider an infinitely narrow monochromatic source that emits a perfectly collimated infrared beam. Let the wavelength of the source be λ_0, so that the wavenumber (or spatial frequency) ω_0 is $\omega_0 = \frac{1}{\lambda_0}$. The source intensity at this wavenumber is I_0.

The electric field of the emitted infrared beam is $\mathrm{E}_0 = |\mathrm{E}_0|\mathrm{e}^{\mathrm{i}\omega_0 \mathrm{t}}$ while the intensity is $I_0 \propto |\mathrm{E}_0|^2$. The fields of beams A and B are given by

$$\mathrm{E}_A = |\mathrm{E}_A|\mathrm{e}^{\mathrm{i}\omega_0 \mathrm{t}} \text{ and } \mathrm{E}_B = |\mathrm{E}_B|\mathrm{e}^{\mathrm{i}\omega_0 \mathrm{t}+\varphi} \tag{3.1}$$

where $\varphi = 2\pi\omega_0\delta$ is the phase difference between the two fields due to the retardation δ.

The intensity at the detector is given by $\mathrm{I}_{det} \propto |\mathrm{E}_{det}\mathrm{E}_{det}{}^*|$ where $\mathrm{E}_{det} = \mathrm{E}_A + \mathrm{E}_B$. It follows:

$$\mathrm{I}_{det}(\delta) \propto |\mathrm{E}_A|^2 + |\mathrm{E}_B|^2 + 2|\mathrm{E}_A||\mathrm{E}_B| \cos 2\pi\omega_0\delta \tag{3.2}$$

Considering that we use an ideal beamsplitter with reflectance and transmittance of exactly 50% (i.e. $\mathrm{I}_A = \mathrm{I}_B = 0.5\mathrm{I}_0$), we obtain:

$$I_{det}(\delta) = 0.5I_0(1 + \cos(2\pi\omega_0\delta)) \tag{3.3}$$

When the retardation is a multiple of λ_0, the two beams are perfectly in phase and they interfere constructively, yielding $I_{det} = I_0$ (see eq. (3.3)). However, if the retardation is for instance $\delta = 1/2\lambda_0$ (i.e. $\Delta d = 1/4\lambda_0$), the two beams have a phase difference of

180º and thus they interfere destructively ($I_{det} = 0$). Thus, if the reference mirror moves linearly with a constant velocity, the interference of the two beams will vary periodically from constructive to destructive interference, resulting in an intensity at the detector that will vary sinusoidal.

In real experiments the signal that is recorded at the detector is affected by several experimental factors (i.e. beamsplitter efficiency, detector response, amplification characteristics of the detector, etc). The influence of these factors, however, is constant in subsequent measurements performed with a given system configuration and can be described by a wavenumber-dependent correction-factor R_0.

$$I_{det}(\delta) = 0.5 R_0 I_0 (1 + \cos(2\pi\omega_0\delta)) \tag{3.4}$$

In FTIR spectroscopy, the modulated component (i.e. AC signal) of the signal recorded at the detector (while moving the reference mirror at a constant velocity) is called an *interferogram*, $U(\delta)$. By defining $B_0 = 0.5 R_0 I_0$, the interferogram for a monochromatic source is given by

$$U(\delta) = B_0 \cos(2\pi\omega_0\delta). \tag{3.5}$$

Eq. (3.5) shows that in the particular case of a monochromatic radiation, the wavenumber ω_0 (or wavelength) of the source can be measured directly from the sinusoidal interferogram $U(\delta)$. Furthermore, the amplitude of the sinusoidal interferogram B_0, is directly related to the intensity of the source I_0 (it is only modified by the instrument characteristics R_0).

3.3 Fourier transform spectroscopy

Having described the processes that occur in a Michelson interferometer with a simple monochromatic source, we will now consider infrared sources with a more complex spectrum. The intensity spectra, $I(\omega)$, of several exemplary light sources and the corresponding simulated interferograms, $U(\delta)$, are shown in Fig. 3.3. Note that the interferogram is defined as the modulated component of the detector signal (no DC component) and therefore the interferograms shown in Fig. 3.3 have negative values. It should also be noted that for a better understanding, in Fig. 3.3 only a short part of the interferograms is shown, which were simulated by analytical calculations.

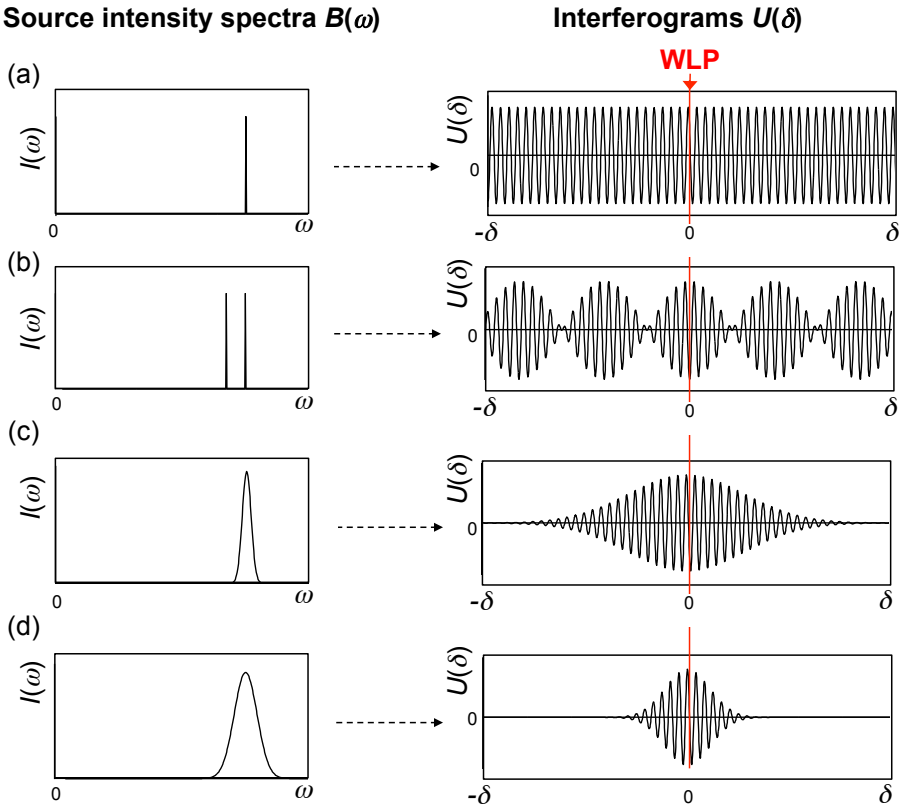

Fig. 3.3: **Different source intensity spectra I(ω) and corresponding interferograms U(δ)**: **(a)** a infinitesimally narrow line; **(b)** two infinitesimally narrow lines of equal intensity; **(c)** narrow Gaussian band; **(d)** wide Gaussian band.

When the source emits a broadband continuum radiation, the interferogram $U(\delta)$ can be represented in a more general way by the integral

$$U(\delta) = \int_{-\infty}^{+\infty} B(\omega)\cos(2\pi\omega\delta)\, d\omega. \qquad \textbf{(3.6)}$$

Following the Fourier inversion theorem, the spectrum of the interferogram $B(\omega)$, is thus given by

$$B(\omega) = \int_{-\infty}^{+\infty} U(\delta)\cos(2\pi\omega\delta)\, d\delta. \qquad \textbf{(3.7)}$$

The position of the reference mirror at which the path difference between the two arms of the interferometer is equal to zero ($\Delta d = 0 \rightarrow \delta = 0$) is called the *white light position* (WLP, marked in Fig. 3.3). At WLP, all frequencies of the emitted radiation interfere constructively, resulting in the highest possible intensity at the detector. Fig. 3.3a shows the intensity spectrum of a monochromatic source and the corresponding sinusoidal interferogram. Fig. 3.3b shows the intensity spectrum of a source that emits at two

narrow spectral lines. The corresponding interferogram is a superposition of two cosine waves, each of them originating from one of the spectral emission lines of the source. Fig. 3.3c and d show two broadband sources with a Gaussian intensity spectra and their corresponding interferograms. Both interferograms are a superposition of many different cosine waves that are in phase at WLP, yielding a sinusoidal interferogram with a maximum value at WLP and a Gaussian envelope. The narrower the width of the intensity spectrum, the wider is the envelope of the interferogram (Fig. 3.3c), and vice versa (Fig. 3.3d).

Eq. (3.7) shows that by measurement of the interferogram and subsequent Fourier transformation, a basic Michelson interferometer allows for recording the intensity spectrum of a broadband radiation. It should be noted that the measured spectra, $B(\omega)$, is unavoidably affected by instrumental factors and therefore the actual intensity spectrum emitted by the source, $I(\omega)$, is not measured. In Fourier transform infrared (FTIR) spectroscopy the instrumental effects are effectively removed by normalization, as will be described in chapter 3.4.1. Eq. (3.7) also shows that theoretically the intensity spectrum can be measured at infinitely high spectral resolution and bandwidth (i.e. from 0 to ∞ cm^{-1}). However, in FTIR spectroscopy there are several practical limitations (i.e. finite retardation of the recorded interferogram) that affect the recorded infrared spectrum, and thus need to be taken into account. In the following we will describe how such practical limitations affect the spectral resolution and the maximum frequency of the obtained spectra.

Spectral Resolution

In real experiments, the reference mirror cannot move an infinitely long distance, thus yielding an interferogram with limited total retardation, which in turn limits the spectral resolution of the recorded spectra. The spectral resolution $\Delta\omega$ obtained with an interferogram of total retardation δ_t is given by

$$\Delta\omega = \frac{1}{\delta_t} \qquad \textbf{(3.8)}$$

For instance, if the reference mirror moves a distance of 600 μm (i.e. δ_t = 1200 μm), the spectral resolution will be $\Delta\omega$ = 1/0.12 cm = 8.3 cm^{-1}.

In Fig. 3.4 we illustrate that the spectral resolution is determined by the total retardation of the recorded interferogram. To this end, three spectra were calculated by FT of three interferograms with different total retardation. The three interferograms were extracted from one and the same interferogram U(δ), which is a superposition of two cosine waves with equal amplitudes, similar to what is shown in Fig. 3.3b. It is clearly seen that the spectral resolution increases for higher total retardation of the interferogram.

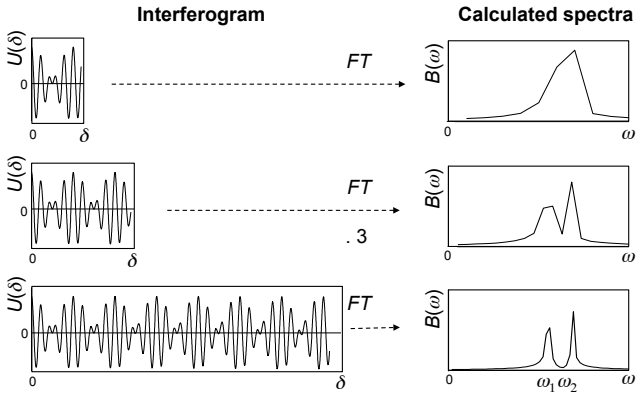

Fig. 3.4: **Spectral resolution in FTIR spectroscopy**. (Left) Interferograms U(δ) composed of two cosine waves with equal amplitudes recorded with different total retardation. (Right) Corresponding calculated spectra B(ω) The lower the total retardation of the interferogram, the lower the spectral resolution. The two lines are not resolved in the upper graph.

Bandwidth

Practically, the interferogram is measured by a data acquisition card (DAQ) with a limited acquisition speed. Thus, the detector signal is recorded at finite sampling intervals, $\Delta\delta$, returning a data set with a discrete and limited number of data points. This limits the maximum frequency ω_{max} that can be measured, which is called the spectral *bandwidth*. An interferogram measured with sampling interval $\Delta\delta$ yields a spectral bandwidth ω_{max} that is given by

$$\omega_{max} = \frac{1}{\Delta\delta}. \tag{3.9}$$

Note that the spectrum calculated by FT of the interferogram ranges from 0 to ω_{max} but as described by the Nyquist theorem only information about the first half (0 to $\omega_{max}/2$) is obtained, as the second half is simply its conjugate [8], [9].

Apodization

In order to analyze the influence of a limited total retardation δ_t on the obtained spectra, a simulated interferogram with infinitely long retardation (see Fig. 3.5a) is multiplied by a truncation function known as *boxcar truncation function*, $D(\delta)$ (see Fig. 3.5b), that is

$$D(\delta) = \begin{cases} 1 & \text{if } -\delta_t \leq \delta \leq +\delta_t \\ 0 & \text{if } |\delta| > \delta_t \end{cases} \tag{3.10}$$

The resulting interferogram and its spectrum are shown in Fig. 3.5c. In this case, the spectrum is given by

$$B(\omega) = \int_{-\infty}^{+\infty} D(\delta)U(\delta)\cos(2\pi\omega\delta)\,d\delta \qquad \textbf{(3.11)}$$

It is known from Fourier mathematics that the Fourier transform (FT) of the product of two functions is the convolution of the Fourier transformation of each of the functions [8]–[10]. Thus, due to the limited retardation (i.e. effective multiplication by a boxcar function), the spectrum of an infinitely long interferogram (Fig. 3.5a) is convoluted by the spectrum of the boxcar function (Fig. 3.5b), yielding the spectrum $B(\omega)$ shown in Fig. 3.5c. In particular, the line shapes of the two peaks are broadened compared to the spectrum shown in Fig. 3.5a, and furthermore oscillations can be observed in the spectrum.

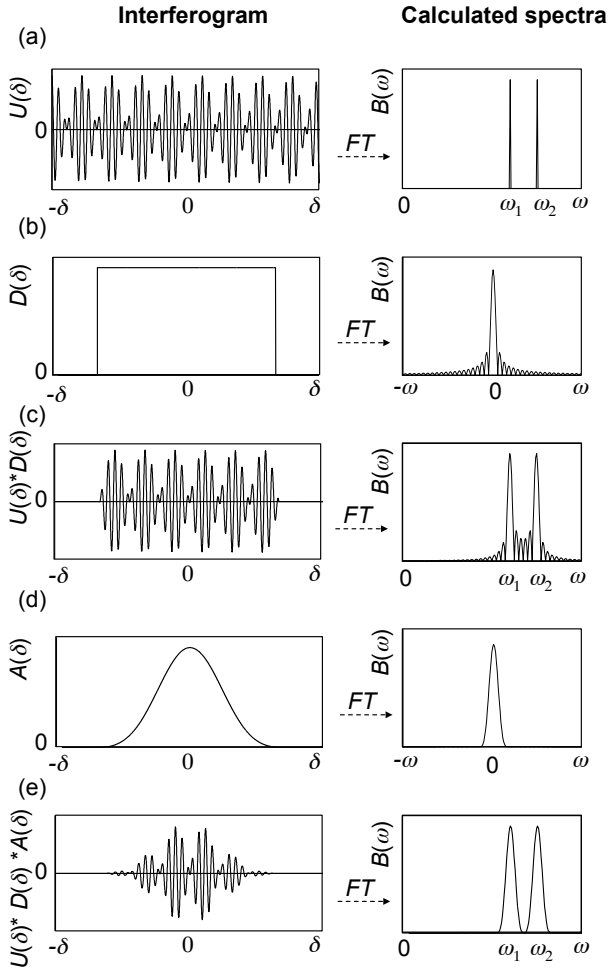

Fig. 3.5: **Apodization in FTIR spectroscopy**. **(a)** An interferogram composed of two cosine waves with equal amplitudes and resulting spectra. Only a short part of the calculated infinitely long interferogram is shown. **(b)** Boxcar truncation function and its corresponding spectra. **(c)** Interferogram of (a), multiplied by the boxcar function of (b) and the resulting spectrum. The two peaks are still resolved, but oscillations due to the truncation appear. **(d)** Apodization function (Black-Man Harris 3-term) and its corresponding spectra. **(e)** Interferogram of (a), multiplied by the apodization function of (d) and the resulting spectrum. The two peaks appear broader than in (c), but the oscillations obtained in (c) vanish.

The oscillations observed in Fig. 3.5c can be minimized by *apodization* of the measured interferogram. Apodization is performed by multiplying the interferogram $U(\delta)$ by an apodization function $A(\delta)$. Any function that has a value of unity at the center of the interferogram and decreases down to zero at the edges can in principle serve as an apodization function. As an example, in Fig. 3.5d we show a "*blackman harris 3 term*" apodization function [4] (see chapter 5.6 for more details) and its Fourier transform. It can be clearly seen that (contrary to the boxcar function) there are no oscillations in the spectrum of this apodization function (right panel of Fig. 3.5d). Fig. 3.5e, left, shows the interferogram from Fig. 3.5c that has been multiplied with the apodization function shown in Fig. 3.5d. The spectrum of the apodized interferogram (Fig. 3.5e, right), does not exhibit the oscillations that are observed in Fig. 3.5c. However, apodization unavoidably suppresses the information near the edges of the interferogram, which has a detrimental effect in the spectral resolution. This can be observed by the broader lineshape obtained for the two spectral lines in Fig. 3.5e compared to Fig. 3.5c.

Zero filling

As illustrated in Fig. 3.4 an interferogram measured with limited total retardation δ_t, yields a spectrum with data points that are spaced by $\Delta\omega = 1/\delta_t$. Thus, two spectral features that are spaced by $1/\delta_t$ cannot be properly recognized. This issue can be addressed by zero filling, which consists of artificially increasing the total retardation of the interferogram, δ_t, by adding zeros to both ends of the interferogram. The zero filling procedure is shown in Fig. 3.6.

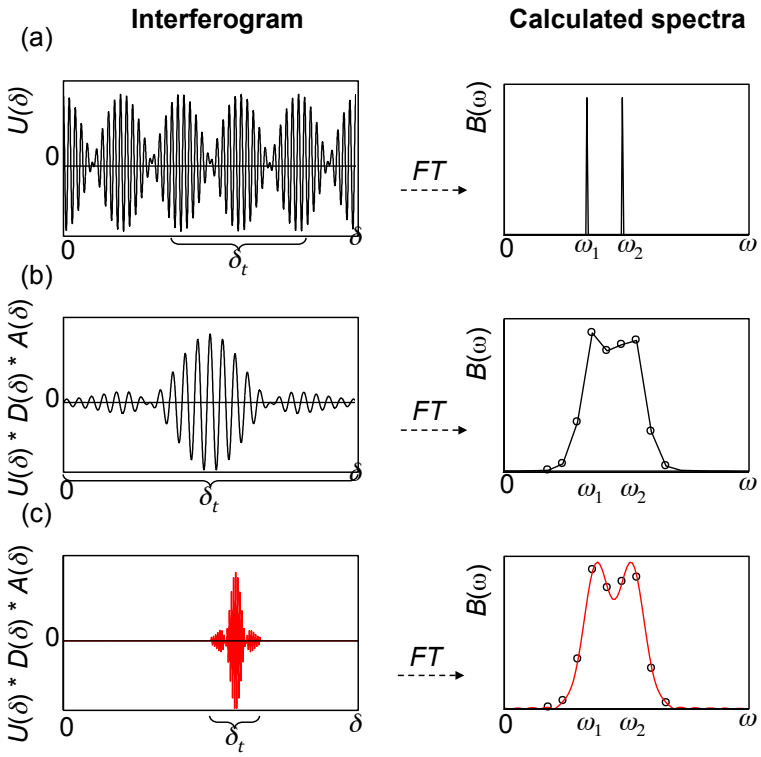

Fig. 3.6: **Zero-filling in FTIR spectroscopy**. **(a)** an interferogram composed of two cosine waves with equal amplitudes and resulting spectrum. Only a short part of the simulated infinitely long interferogram is shown. **(b)** Part of the interferogram (marked in (a)) multiplied by a "*blackman harris 3 term*" apodization function and the corresponding spectrum. **(c)** The interferogram of (b) which has been extended by a factor of 6, by adding zeros at both ends. On the right side, the resulting spectrum is shown. The black dots in the spectrum mark the data points of the (b) spectrum, to illustrate that zero-filling does not change the original data points, but adds new intermediate points.

In Fig. 3.6a we show an interferogram $U(\delta)$ (similar to Fig. 3.5a), which is a superposition of two cosine waves with equal amplitudes. The corresponding spectrum is shown on the right. In Fig. 3.6b part of the interferogram of Fig. 3.6a with a length of δ_t (marked in Fig. 3.6a) has been multiplied with a "*blackman harris 3 term*" apodization function with the same length. The resulting spectrum is shown on the right. The relatively long distance between adjacent spectral points in Fig. 3.6b does not allow for recognizing the two spectral lines shown in Fig. 3.6a. In Fig. 3.6c the interferogram of Fig. 3.6b has been extended by a factor of 6 by adding zeros on both sides. It can be clearly seen that the resulting spectrum has more data points (i.e. they are more closely spaced), and that the two intensity peaks shown in Fig. 3.6a can now be identified as separate peaks. It is important to note that the spectral resolution is not increased by zero-filling. However more spectral points are obtained per cm^{-1} and the spectra become smoother, which allows for a better visualization of the peaks that are spaced closely to the resolution limit. The black circles in spectra of Fig. 3.6b and Fig. 3.6c show that original data points are not changed, but only new data points are added by zero-filling.

3.4 FTIR spectroscopy techniques

The fundamental parameter that governs light-matter interaction is the complex refractive index, which is given by

$$\tilde{n}(\omega) = n(\omega) + i\kappa(\omega) \tag{3.12}$$

where $n(\omega)$ is the real part of the refractive index at ω (referred usually, and in this thesis, simply as to the refractive index), $\kappa(\omega)$ is the imaginary part of the refractive index at ω [4](referred usually, and here, as to the absorption index).

In Fig. 3.7 we show examples of refractive index $n(\omega)$ and absorption index $\kappa(\omega)$ spectra of liquid water (data taken from http://refractiveindex.info and published in [11]). Both spectra show two clear spectral signatures at 1650 cm^{-1} and 3390 cm^{-1} (marked with dashed red lines in Fig. 3.7), which indicate the presence of vibrational resonances at these frequencies. In particular, $\kappa(\omega)$ shows bell-shaped features, while $n(\omega)$ shows dispersion-like features. Importantly, the peak positions in the absorption spectrum allow for extracting the frequency of the vibrational resonances (peak maximum), while the relative height of the bands provides information about the relative strength of the resonances (i.e. the higher the band, the stronger the resonance).

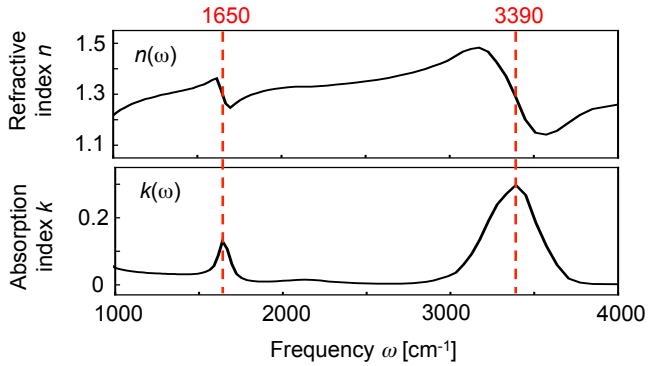

Fig. 3.7: **Spectrum of refractive index**. Spectra of the real and imaginary parts of the refractive index of liquid water at 25ºC, taken from "*http://refractiveindex.info*"

3.4.1 Transmission-FTIR spectroscopy

We first describe the most conventional way to perform FTIR spectroscopy, that is, transmission-FTIR spectroscopy, where a broadband infrared beam passes through a Michelson interferometer and subsequently is transmitted thought the sample, as illustrated in Fig. 3.8. An infrared detector measures the transmitted light.

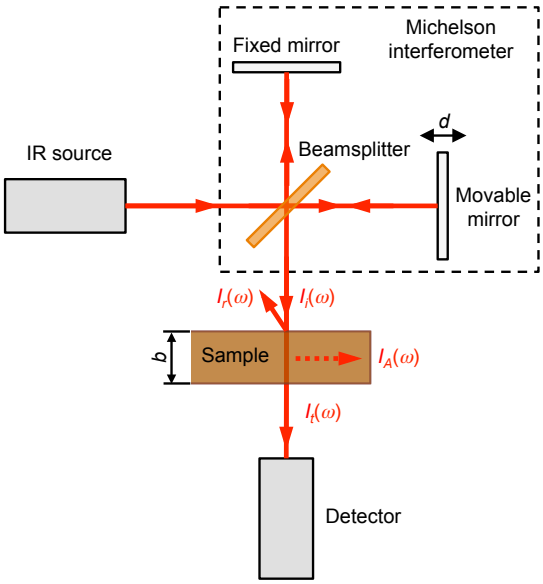

Fig. 3.8: **Setup of transmission-FTIR spectroscopy**. Infrared radiation from a broadband infrared source is passed through a Michelson interferometer, comprising a beamsplitter (BS) and a fixed and a moving mirror. After the interferometer, the light is passed through the sample and then focused onto the detector.

The incident light can in principle be partially reflected at the surface of the sample, absorbed by the sample, or transmitted through the sample. However, the samples are prepared using standard and specific sample preparation procedures, which ensure that only a negligible part of the incident light is reflected, $I_r(\omega) \sim 0$. Thus, the difference between the intensities of the incident, $I_i(\omega)$, and transmitted, $I_t(\omega)$, beams in a good approximation exclusively yields absorption of the sample.

In transmission-FTIR spectroscopy, the ratio between the intensities of the incident and transmitted beams is measured, which is called *transmittance*. It is given by

$$T(\omega) = \frac{I_t(\omega)}{I_i(\omega)} \tag{3.13}$$

Following the basic operation principle of FTIR spectroscopy, an interferogram is measured by recording the detector signal while the movable mirror is moved linearly. Subsequent Fourier transformation of the interferogram yields the spectrum, $B(\omega)$, .

In transmission-FTIR spectroscopy experiments two spectra are measured, one with the sample inside the spectrometer $B_s(\omega)$ and the other one without any sample at the spectrometer $B_0(\omega)$, usually referred as sample and reference spectra, respectively. By normalizing the sample spectrum to the reference spectrum, the transmittance $T(\omega)$ of the sample is obtained. Importantly, such normalization allows for correcting for the instrumental characteristics (described by the correction factor, $R_0(\omega)$, see chapter 3.2) and extracting the pure sample response.

$$T(\omega) = \frac{B_s(\omega)}{B_0(\omega)} = \frac{I_t(\omega)R_0(\omega)}{I_i(\omega)R_0(\omega)} = \frac{I_t(\omega)}{I_i(\omega)} \tag{3.14}$$

Let us now describe how the intensity of light decreases depending on the complex refractive index of the medium in which it is propagating. An electric field of a plane electromagnetic wave that travels in the x direction through a medium is given by

$$E(x,t) = Re\left[E_0 e^{i(\tilde{k}x-\omega t)}\right] \tag{3.15}$$

where $\tilde{k}$ is the complex wave number. The complex wave number $\tilde{k}$, is related to the complex refractive index $\tilde{n}$ of the medium by $\tilde{k} = \frac{2\pi\tilde{n}}{\lambda}$, with λ being the vacuum wavelength at ω. It follows

$$E(x,t) = E_0 Re\left[e^{i\left(\frac{2\pi\tilde{n}}{\lambda}x-\omega t\right)}\right] = E_0 e^{-\frac{2\pi\kappa x}{\lambda}} Re\left[e^{i\left(\frac{2\pi n}{\lambda}x-\omega t\right)}\right] \tag{3.16}$$

Eq. (3.16) clearly shows that when a plane electromagnetic wave is traveling through a medium with a non-zero absorption index (κ), its electric field decays exponentially with the penetration distance x. As the intensity of transmitted light is measured in FTIR spectroscopy, we find

$$I(x) = {E_0}^2 e^{-\frac{4\pi\kappa(\omega)x}{\lambda}} = I_0 e^{-\alpha(\omega)x} \tag{3.17}$$

where $\alpha(\omega) = \frac{4\pi}{\lambda}\kappa(\omega)$ is the *linear absorption coefficient* (cm^{-1}) at ω, which is proportional to the absorption index.

Thus, by combining eq. (3.14) and (3.17), we obtain the transmittance measured in transmission-FTIR spectroscopy experiments. It is given by

$$T(\omega) = \frac{I_t(\omega)}{I_i(\omega)} = \frac{I_0 e^{-\alpha(\omega)x}}{I_0} = e^{-\alpha(\omega)x} \tag{3.18}$$

In order to obtain a spectrum that is proportional to the absorption index, $\kappa(\omega)$, the absorbance $A_t(\omega)$, is defined as

$$A_t(\omega) = log_{10}\frac{1}{T(\omega)} = \frac{1}{ln10}\alpha(\omega)x \tag{3.19}$$

3.4.2 Grazing incidence FTIR (GI-FTIR) spectroscopy

Grazing incidence FTIR (GI-FTIR) spectroscopy uses an alternative experimental configuration that allows for measuring infrared spectra of thinner samples than in transmission-FTIR spectroscopy [4]. After passing through a Michelson interferometer the infrared beam illuminates the sample at an angle of incidence of around 86° and the reflected beam is measured at the detector. In order to increase the reflected intensity, a thin layer of the sample is deposited in a highly infrared-reflective metallic substrate (i.e. Au), at which the infrared beam is reflected. The setup of a GI-FTIR spectrometer is schematically illustrated in Fig. 3.9.

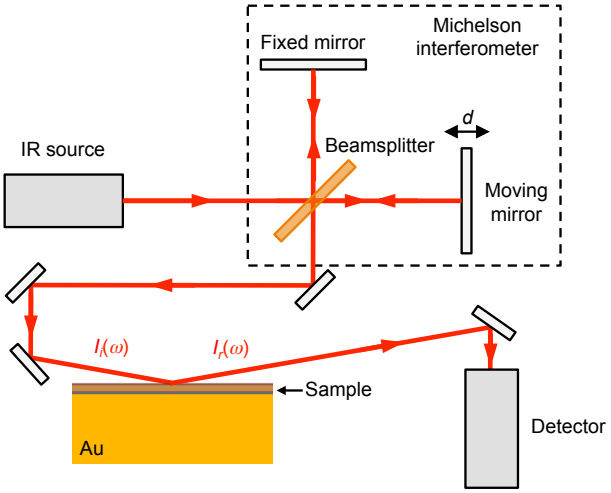

Fig. 3.9: **Setup of grazing incidence-FTIR (GI-FTIR) spectroscopy**. Infrared radiation from a broadband infrared source is passed through a Michelson interferometer, comprising a beamsplitter (BS) and a fixed and a moving mirror. After the interferometer, the light illuminates the sample at an angle of incidence of around 86°. The reflected beam is focused onto the detector.

When reflecting on the metallic surface, the reflected electromagnetic wave undergoes a polarization-dependent phase shift compared to the incident electromagnetic wave and thus, the interference between the two waves near the surface is also polarization dependent. The s-polarized radiation (i.e. electromagnetic field parallel to the surface) interferes destructively resulting in no electric field parallel to the surface. However, p-polarized radiation (i.e. electromagnetic field almost perpendicular to the surface) interferes constructively resulting in an electric field at the surface with a large component perpendicular to the surface [12]. Such electric field efficiently excites the molecular vibrations close to the surface, which results in an absorption of the p-polarized infrared radiation. Interestingly, the increase of the p-polarized electric field near the surface allows for measuring infrared spectra of thinner samples than in transmission-FTIR spectroscopy. Furthermore, it allows for selectively mapping the vibrations perpendicular to the surface. Due to the destructive interference near the

surface, the s-polarized light is negligibly absorbed by the sample. Thus, it is usually removed (i.e. with a polarizer) to improve the signal to noise ratio (SNR) of the measurement.

In GI -FTIR spectroscopy the ratio between the intensities of the incident and reflected beams is measured, which is called *reflectance* . It is given by

$$R_{GI}(\omega) = \frac{I_r(\omega)}{I_i(\omega)}, \tag{3.20}$$

where $I_i(\omega)$ and $I_r(\omega)$ are the intensities at ω of the incident and reflected beams, respectively.

Similar to transmission-FTIR spectroscopy (see chapter 3.4.1), two spectra (that is, sample and reference spectra) are measured following the basic operation principle of FTIR spectroscopy. The sample spectrum is measured by recording the infrared light reflected at the sample, which is deposited on a metallic substrate. For the recording of the reference spectrum, the infrared light is simply reflected at the clean metallic substrate without any sample. Thus, normalization to the reference spectrum corrects for all the instrumental characteristics and yields the pure sample response.

Let us now analyze how in GI-FTIR spectroscopy the intensity of the reflected infrared beam changes depending on the complex refractive index of the sample. Due to the reflection configuration, part of the infrared beam is reflected at the sample. The reflectivity of the sample surface is mainly determined by its refractive index $n(\omega)$ [4], which spectrum shows dispersion-like features at the absorbing frequencies (see Fig. 3.7). Further, the infrared beam that penetrates the sample is reflected at the metallic substrate. Due to excitations of vibrations near the metallic surface, the penetrating beam gets absorbed. Thus, strictly speaking, the reflectance spectrum measured in GI-FTIR spectroscopy is a superposition of $\kappa(\omega)$ (due to absorption) and $n(\omega)$ (due to reflection at the sample).

However, the spectral intensity variations due to absorption are much higher than the variations due to the reflectivity. Thus, the reflectance spectra measured in GI-FTIR spectroscopy show the absorption bands similar to transmittance spectra measured in transmission-FTIR spectroscopy. Still, it is important to bear in mind that due to the influence of the light reflected at the sample the peak positions at GI-FTIR spectroscopy may be blue shifted compared to transmission-FTIR spectroscopy [4].

In order to obtain a spectrum that is in a good approximation proportional to the absorption index spectrum, the *absorbance* $A_{GI}(\omega)$ of a sample at wavenumber ω is defined as

$$A_{GI}(\omega) = log_{10}\frac{1}{R_{GI}(\omega)}, \tag{3.21}$$

analogously to eq. (3.19).

3.4.3 Attenuated total reflectance FTIR (ATR-FTIR) spectroscopy

As illustrated schematically in Fig. 3.10, in ATR-FTIR spectroscopy the infrared beam is directed into a crystal, which has a significantly higher refractive index than the sample to be measured [4]. The infrared beam reflects at the internal surface of the crystal several times until it exits the opposite side of the crystal and it is focused into the detector. The internal reflectance at the surface of the crystal creates an evanescent wave that extends only a few microns into the sample in contact with the crystal (see the zoomed in representation of a single reflection in Fig. 3.10). The penetration depth of the infrared beam into the sample is proportional to the wavelength and is technically defined as the distance required for the electric field amplitude of the evanescence wave to decay to e^{-1} of its value at the surface. Typically the penetration depth in ATR-FTIR spectroscopy ranges from 0.5 μm up to about 5 μm. Thus, the sample must be in intimate contact with the crystal. Part of the energy of this evanescent wave is absorbed by molecular vibrations excited in the sample, and therefore the infrared beam that reflects at the internal surface of the crystal gets attenuated and altered. At each of the multiple reflections at the internal surface of the crystal the infrared beam gets attenuated resulting in an increased overall attenuation.

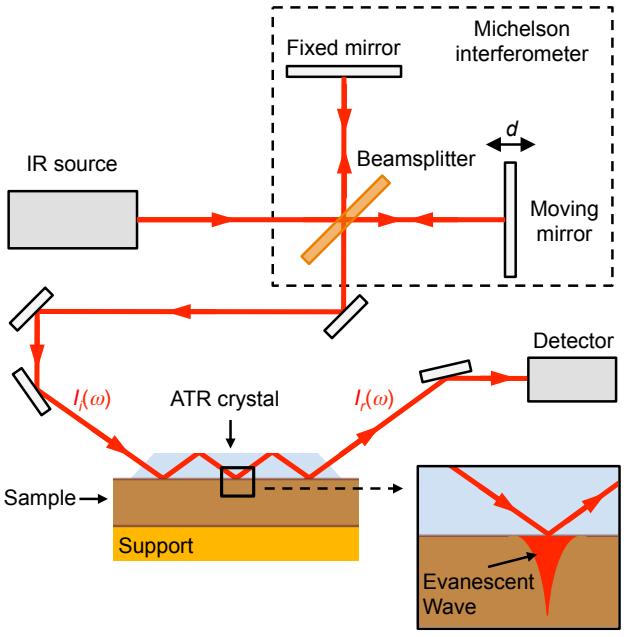

Fig. 3.10: **Setup of attenuated total reflectance FTIR (ATR-FTIR) spectroscopy**. Infrared radiation from a broadband infrared source is passed through a Michelson interferometer, comprising a beamsplitter (BS) and a fixed and a moving mirror. After the interferometer, the light is directed into a crystal. After reflecting several times at the internal surface of the crystal the light exits the opposite side of the crystal and is focused into the detector.

In ATR-FTIR spectroscopy, the ratio between the intensities of the incident and reflected beams is measured, which is called reflectance. It is defined as

$$R_{ATR}(\omega) = \frac{I_r(\omega)}{I_i(\omega)} \tag{3.22}$$

where $I_i(\omega)$ and $I_r(\omega)$ are the intensities at ω of the incident and reflected beams, respectively.

The sample spectrum is measured by bringing the sample into contact with the ATR crystal, while the reference spectrum is measured with a clean crystal (i.e. no sample in contact). The spectra are measured following the basic operation principle of FTIR spectroscopy. The division between the two spectra corrects for the instrumental characteristics and yields the reflectance of the sample.

One important experimental factor that affects the reflectance measured in ATR-FTIR spectroscopy is the ratio between the refractive indices of the ATR crystal and the sample [13]. The refractive index of the ATR crystal can be regarded as a constant, while the sample refractive index shows a dispersion-like spectral dependence near absorbing frequencies (see Fig. 3.7). It can be shown that consequently the peak position of the ATR reflectance spectra is shifted to lower frequencies (red-shifted) compared to that of transmittance spectra [13].

Analogue to GI-FTIR spectroscopy, in ATR-FTIR spectroscopy the absorbance spectrum $A_{ATR}(\omega)$ is typically used, which at wavenumber ω is defined as

$$A_{ATR}(\omega) = log_{10} \frac{1}{R_{ATR}(\omega)} \tag{3.23}$$

3.4.4 Micro-FTIR and micro-ATR-FTIR spectroscopy

In all three FTIR spectroscopy techniques introduced above, FTIR spectra of typically macroscopic samples are acquired as the spatial extension of the used thermal sources prevents diffraction limited focusing.

In order to perform spectroscopy of local material properties and gain access to spatial variations, in micro-FTIR spectroscopy the spatial resolution is increased by imaging the sample in transmission mode through small apertures [14], [15] (see schematic illustration in Fig. 3.11). Though the minimum size of the apertures is limited by the related intensity loss, state-of-the-art micro-spectrometers achieve a spatial resolution of about 10 μm [4].

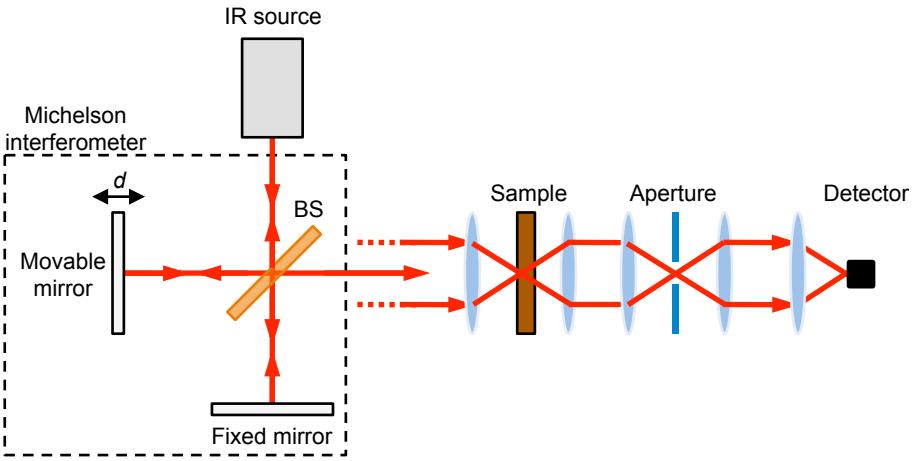

Fig. 3.11: **Setup of micro-FTIR spectroscopy**. After passing through the Michelson interferometer, the broadband infrared light is focused on the sample. With a small aperture the measured sample area can be spatially restricted to increase the spatial resolution.

Importantly, more recently micro-ATR-FTIR spectroscopy has been developed. Micro-ATR-FTIR spectroscopy uses a Cassegrain-style reflective objective and a high-refractive-index germanium ATR "crystal" of some hundreds of microns in diameter [16]. The crystal has a sharp tip on one side, which is in intimate contact with the sample. The infrared radiation undergoes total internal reflection at the tip surface, generating evanescence waves that interact with the sample. The reflected radiation is collected by the objective. With micro-ATR-FTIR spectroscopy higher spatial resolution than with aperture-based micro-FTIR spectroscopy can be achieved [17], [18].

3.4.5 Hyperspectral infrared imaging

A natural continuation of conventional FTIR spectroscopy is hyperspectral infrared imaging. In hyperspectral infrared imaging local spectra at each pixel of a two-dimensional image of a sample are recorded to yield a three-dimensional hyperspectral data cube with two spatial dimensions and one spectral dimension (the infrared frequency). Since the first report in 1995 [19], the technology has evolved dramatically, and now powerful hyperspectral infrared imaging spectrometers are commercially available. In the following we will briefly describe the current hyperspectral infrared imaging technology based on the description at [20].

Hyperspectral infrared imaging spectrometers typically use two-dimensional array detectors based on focal plane arrays (FPAs). The largest commercially available FPAs have 128 x 128 pixels, which allow for fast spectroscopic imaging with good SNR. Hybrid linear array detectors (i.e. 2x8 pixels) can also be used for the recording of hyperspectral infrared images. When using linear detectors, the sample is repeatedly moved in order to subsequently record spectral data from different adjacent regions.

Such process is repeated until the spectra of all the regions of the image are measured. Though they have been extensively used, linear array detectors are slower than two-dimensional array detectors and provide lower SNR and spatial resolution. Another option to record hyperspectral images is to measure sequentially the spectra of single points on the sample and perform a two-dimensional raster scan. But the acquisition time of the complete hyperspectral image is comparably higher than for linear and two-dimensional array detectors. Further, the SNR is typically lower, especially when measuring infrared spectra with high spectral resolution.

Hyperspectral infrared imaging can be accomplished by using the transmission, GI-FTIR or ATR-FTIR spectroscopy techniques described in this chapter, and by using any type of detector explained above. The key for any configuration (that is, FTIR spectroscopy technique and detector type) is that the sample position needs to be accurately controlled and manipulated. Though the first applications were based in micro-FTIR spectroscopy [19], in the recent years micro-ATR-FTIR spectroscopy has increasingly been used for hyperspectral infrared imaging [16], [18], [21]. Due to the comparably low penetration depth in ATR-FTIR spectroscopy, the spectral signals obtained for even strong bands can be relatively weak. However, micro-ATR-FTIR spectroscopy has several important advantages over micro-FTIR and GI-FTIR spectroscopy. It has no artifacts caused by Mie scattering, the sample preparation is easier and the spatial resolution of the hyperspectral images is higher [22].

Similar to other hyperspectral techniques (e.g. Raman microspectroscopy [23], [24] or electron energy loss spectroscopy (EELS) [25]), hyperspectral infrared images include a high quantity of information (i.e. thousands of infrared spectra). Thus, in order to extract interpretable knowledge, the appropriate data analysis procedures need to be selected and applied. In recent years, the interest on multivariate data analysis methods has increased and many powerful specific algorithms have been developed [26]–[29]. Multivariate analysis is a data analysis method that aims to explore the spectral and spatial information contained in the hyperspectral image in order to segment the image in groups of pixels with similar infrared spectra. Hyperspectral infrared imaging together with multivariate data analysis has proven to be a highly powerful technique, specially for the analysis of pharmaceutical products and for medical diagnosis [20].

4 Scattering-type Scanning Near-field Optical Microscopy (s-SNOM)

In this chapter the principle of scattering-type Scanning Near-field Optical Microscopy (s-SNOM) will be introduced, a technique that overcomes the diffraction limit in optical imaging by orders of magnitude. The s-SNOM setup and the theory of near-field interaction will be briefly described following the basic concepts from refs [3], [30]–[32] *and the description of ref* [33].

4.1 Introduction

The spatial resolution in classical optical microscopy is limited by diffraction because of the wave nature of light [34]. Due to this limitation, individual features cannot be resolved if they are closer than roughly half of the wavelength of the illuminating light. For infrared light the spatial resolution is limited to some micrometers (e.g. 3 μm for light of 1660 cm^{-1}), preventing infrared imaging on the nanometer scale or even single-molecule level.

Among others, one technique that circumvents the diffraction limit in classical optical microscopy is scanning probe microscopy (SPM) [35]. SPM techniques use a sharp probing tip to scan the surface of a sample. While scanning the surface, different properties of the sample (i.e. mechanical, electrical, magnetic or optical) can be observed by analyzing the local tip-sample interaction and two-dimensional images of the sample can be recorded. SPM techniques that record the optical properties of the sample are called scanning near-field optical microscopy (SNOM) techniques.

The first experimental approach to record the local optical information while scanning the surface was not implemented using a probing tip but instead an aperture probe was used [36]. Such a technique is referred as aperture SNOM and is based on a small aperture to overcome the diffraction limit. Typically a metal coated single-mode optical fiber is used as an aperture with a small opening at its end. However, the efficiency of such an aperture decreases when using small apertures and light of long wavelength. Thus, the resolution of aperture SNOM is not wavelength independent and is limited in practice to about $\lambda/10$ [14], [15], [37] at visible wavelength.

An alternative technique to aperture SNOM is scattering-type scanning near-field optical microscopy (s-SNOM). s-SNOM uses a probing tip and is the only imaging technique that provides completely wavelength-independent resolution (i.e. same resolution for visible[38], infrared[39] and THz light [40], [41]), which is on the order of 20nm [34], [42]. In this chapter the principle of s-SNOM will be introduced and the s-SNOM setup and the theory of near-field interaction will be briefly described.

4.2 Principle of s-SNOM

The basic principle of s-SNOM is illustrated in Fig. 4.1. A monochromatic laser beam is focused onto a metal-coated probing tip by a parabolic mirror (not shown in the figure). The metal-coated tip acts as an optical antenna that concentrates the electromagnetic field in the close proximity of its apex and backscatters radiation in all directions [43], [44]. The backscattered radiation is collected by the same parabolic mirror that is used to focus the laser beam onto the tip. The collected radiation is measured by interferometric detection, that is, both amplitude and phase are recorded. When the tip is brought into contact or very close to a sample, the strong optical near-field interaction between the tip and sample modifies the backscattered radiation, allowing for probing the dielectric properties of the sample. Importantly, the near-field interaction is localized to the scale of the tip radius, which is typically of about 20 nm. Thus, by measuring the backscattered radiation while scanning the sample surface, optical amplitude and phase images with nanoscale resolution can be obtained.

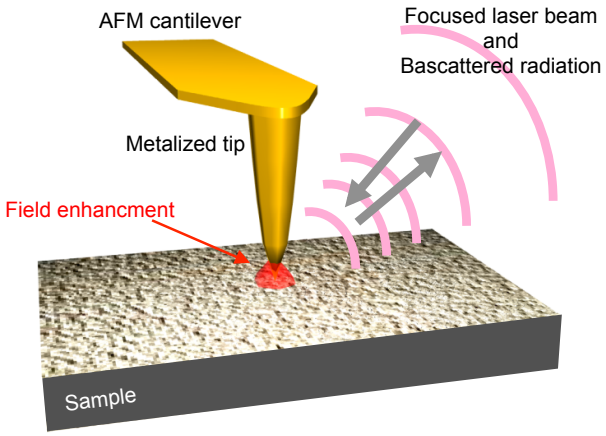

Fig. 4.1: **Principle of s-SNOM**. A sharp atomic force microscopy (AFM) tip is mounted on a cantilever and illuminated by a focused laser beam. The light backscattered by the tip is collected.

4.2.1 Atomic Force Microscopy (AFM)

s-SNOM is built upon an atomic force microscope (AFM) which represents the core of the s-SNOM setup. Therefore we will briefly describe how an AFM operates (adapted from ref. [31]).

AFM is a SPM technique that by scanning a probing tip over the sample surface allows for measuring its topography. The basic AFM setup is shown in Fig. 4.2. The AFM used in s-SNOM is operated in “tapping” mode. The probing tip is affixed to the bottom side of a cantilever, which is driven to oscillation in z-direction at its resonant frequency Ω,

with an amplitude of typically 20 to 50 nm. The cantilever vibration is monitored by reflecting a focused laser beam from the top side of the cantilever, and by measuring its deflection by a photodiode. The tip and the sample are maintained at such a distance that the tip touches slightly the sample at every oscillation. The oscillation amplitude of the cantilever is largely dependent on the tip-sample distance. Therefore, the measured oscillation amplitude is used to regulate the tip-sample distance by moving the sample up or down to keep the oscillation amplitude constant while scanning. Note that the sample is placed on a piezoelectric scanner capable of positioning the sample in all *x*- *y*- and *z*- directions. By recording the vertical position of the sample as a function of its lateral position, the topography of the sample is acquired.

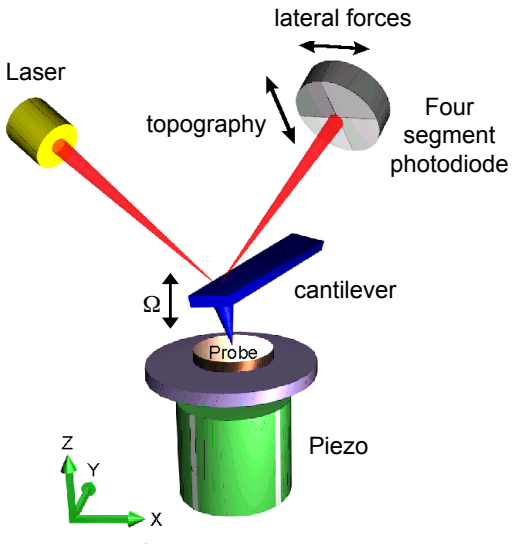

Fig. 4.2: **Schematic representation of a typical AFM setup**. A laser beam is reflected from the backside of the cantilever, onto a position-sensitive Photodiode. The sample is mounted on a piezo to precisely move the sample up and down. (Image taken from ref. [45]).

AFM operated in tapping mode is very well suited to implement the s-SNOM principle as the AFM tip is scanned over the surface of the sample and more interestingly, the tip is kept in contact (it gets into contact at every oscillation) with the sample allowing for the near-field interaction to occur. Furthermore the oscillation of the tip-sample distance introduces a modulation in the near-field interaction that facilitates its detection as will be described in more detail in chapters 4.2.3 and 4.2.4.

4.2.2 Tip illumination and nanofocusing

In s-SNOM a metal-coated AFM tip is used. In order to obtain near-field optical information together with the AFM topography image, a monochromatic laser is

focused onto the metal-coated AFM tip by a parabolic mirror (see Fig. 4.1). The laser excites charge oscillations in the metal [34], [46], [47], which cause a charge accumulation in the tip apex resulting in very high local fields [43], [44]. Fig. 4.3 shows the numerical simulation of the field distribution of a metal tip when it is illuminated with far-infrared light (λ=118 μm). The illumination considered in the simulation is a plane wave with linear polarization parallel to the tip axis (marked by yellow arrows). The color scale shows the ratio between the local and the incident electric fields, that is, the field enhancement. It can be shown [41] that the high electric field at the tip apex observed in Fig. 4.3 is an evanescent field that decays exponentially with distance on the scale of the tip radius. When the tip-sample distance is small enough (relative to the spatial decay of the electric field in the tip apex), the near-field interaction between the tip and the sample affects the radiation backscattered by the tip. The backscattered radiation mediated by the near-field interaction is referred as to *near-field scattering*. The near-field interaction can be described by the complex valued scattering coefficient $\sigma = se^{i\varphi}$ (with amplitude s and phase φ), which relates the scattered field E_s with the incident field E_i according to

$$E_s = \sigma E_i \tag{4.1}$$

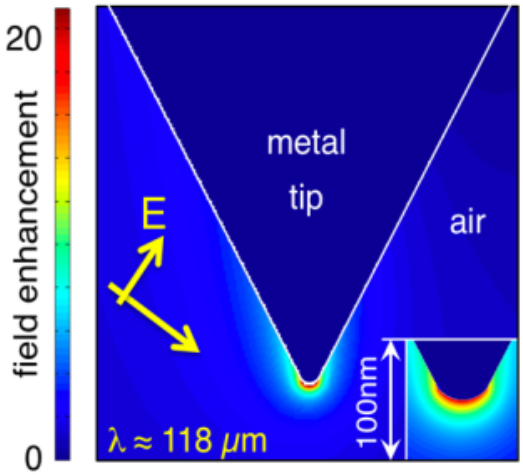

Fig. 4.3: **Simulation of field distribution of a metallic tip.** Numerical simulation of field distribution of a metal tip illuminated with far-infrared light with λ=118 μm. (Image taken from ref. [41]).

4.2.3 Detection of the scattered light

Information about the near-field interaction can be obtained by measuring the backscattered light. However, the near-field scattering introduced in chapter 4.2.2 is not the only contribution to the overall back-propagating light collected by the parabolic

mirror. There exists a second contribution that consists of reflections from other optical elements as well as the direct scattering of the tip. This second part does not contain any information about the near-field interaction and therefore it is called the *background signal* or *background scattering*.

In order to analyze the nature and interplay between the near-field scattering and background scattering, let us consider the simplest detection scheme in which the intensity of the light backscattered by the tip E_s is directly measured by a detector. The intensity measured at the detector I_{det} is given by

$$I_{det} = I_s \propto |E_s|^2 = \left|E_{nf} + E_{bg}\right|^2 = \left(E_{nf} + E_{bg}\right)\left(E_{nf} + E_{bg}\right)^* \quad \textbf{(4.2)}$$

where E_{nf}, and E_{bg} are the near-field scattering and background scattering fields, respectively.

Due to the tip oscillation, both contributions are modulated and thus E_s can be written as follows

$$E_s = E_{nf} + E_{\mathrm{bg}} = \sum_{n=0}^{\infty} E_{nf,n} \cos(n\Omega t) + \sum_{n=0}^{\infty} E_{bg,n} \cos(n\Omega t) \quad \textbf{(4.3)}$$

where $E_{nf,n}$ and $E_{bg,n}$ denote the n$^{\text{th}}$ order complex-valued Fourier coefficients of E_{nf} and E_{bg}, respectively [31].

The tip oscillation affects in a different way to the two contributions. Due to the rapid exponential decay of the evanescent waves (in the order of the tip diameter), the near-field scattering E_{nf} exhibits a fast nonlinear decrease as the distance increases (see chapter 4.3 for theoretical approximation). On the other hand, the background scattering E_{bg} only changes due to spatial variation of the incident electric field, which occurs in the length-scale of its wavelength. The tip oscillation amplitude is much smaller than the wavelength of the incident field. Therefore, the background scattering can in good approximation be considered to change linear with the tip position (i.e. weak high harmonic components), while the near-field scattering changes highly non-linear with the tip position (i.e. strong high harmonic components). As a consequence, for sufficiently high harmonics (in the infrared usually $n \geq 2$), the Fourier coefficients of the background scattering are negligible compared to the Fourier coefficients of the near-field scattering, $E_{bg,n} \ll E_{nf,n}$ [31].

If the electric field E_s were measured instead of the intensity, I_s, demodulation at a sufficiently high harmonic (i.e. integer multiple of the tip oscillation frequency Ω) would suppress the background contribution, yielding the pure near-field information. However, in practice the detector signal is proportional to the intensity I_s rather than to the electric field E_s. As the intensity is the square of the electric field, $I_{det} \propto I_s \propto |E_s|^2$,

the background and near-field terms are mixed (see eq. (4.2) and eq. (4.3)). Assuming that $E_{bg,n}$ is negligible for n ▷ 1, any harmonic component of the detected intensity is given by

$$I_{det,n} = E_{bg,0}E^*{}_{nf,n} + E_{nf,n}E^*{}_{bg,0} \tag{4.4}$$

As shown in Eq. (4.4), all harmonic components of the detected signal $I_{det,n}$ are affected by background $E_{bg,0}$. As a consequence, measurement of the intensity of the light backscattered by the tip and subsequent demodulation at high harmonics does not allow for obtaining completely background free near-field information [31].

In order to achieve a efficient background suppression and obtain the amplitude and phase information of the near-field scattering E_{nf}, a combination of pseudoheterodyne interferometric detection [48] and higher harmonic demodulation of the measured signals can be used. The pseudoheterodyne interferometric detection will be described in the following.

4.2.4 Pseudoheterodyne interferometric detection

The experimental setup of s-SNOM that allows for pseudoheteordyne interferometric detection is shown in Fig. 4.4.

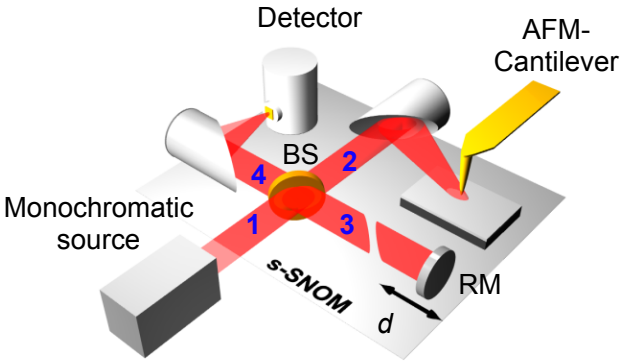

Fig. 4.4: **Schematic s-SNOM setup**. The metallic tip of the near-field microscope (s-SNOM) is illuminated with a monochromatic laser source. The backscattered light is analyzed with an asymmetric Michelson interferometer, comprising a beamsplitter (BS), reference mirror (RM) and a detector.

The s-SNOM setup is based on an asymmetric Michelson interferometer. The beam provided by the monochromatic laser (beam 1 in Fig. 4.4) is divided into two beams

(beam 2 and 3) by the beamsplitter (BS). The beam 3, referred as the *reference* beam, is reflected at the reference mirror (RM), while the beam 2 is focused onto the AFM tip by a parabolic mirror, which also collects back the backscattered light [49], [50]. The two back-propagating beams are combined at the beamsplitter and their interference is measured at the detector. The detector signal now is given by

$$I_{det} \propto \left|E_s + E_{ref}\right|^2 = \left(E_{nf} + E_{bg} + E_{ref}\right)\left(E_{nf} + E_{bg} + E_{ref}\right)^* \quad \textbf{(4.5)}$$

where E_{ref} is the electric field of the reference beam.

In pseudoheterodyne detection there are two modulation mechanisms. On one hand, due to the tip oscillation the light backscattered from the tip ($\mathrm{E_{nf}} + \mathrm{E_{bg}}$) is modulated at a frequency Ω (typically around $\Omega \sim 140\mathrm{KHz}$) and its higher harmonics nΩ (with n being an integer >1). On the other hand, the reference beam is phase modulated due to oscillation of the RM at a frequency M (typically at few hundreds of Hz). Due to the interference of the backscattered light (containing both E_{nf} and E_{bg}) with the phase modulated reference beam (E_{ref}), the detector signal has a frequency spectrum as illustrated in Fig. 4.5.

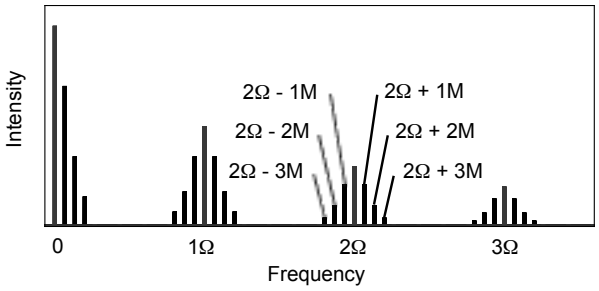

Fig. 4.5: **Signal splitting in pseudoheterodyne detection in s-SNOM**. The metallic AFM-tip is oscillating with a frequency Ω, and the reference mirror with a frequency M (M≪Ω), causing the interferometric signal to split up in sidebands nΩ±mM. Adapted from ref. [31].

The modulation at a lower frequency M introduced by the reference mirror vibration generates new spectral components at frequencies $f_{\mathrm{sb}} = n\Omega + mM$, $n, m \neq 0$, which are called *sideband* frequencies. It has been shown [31] that the background contribution at sufficiently high harmonic sidebands is negligible. Therefore, by measuring the magnitude of the Fourier coefficients at $n\Omega + 1M$ and $n\Omega + 2M$ of the detector signal, the amplitude $Abs\left[E_{nf,n}\right]$ and phase $Arg\left[E_{nf,n}\right]$ of the n$^{\mathrm{th}}$ harmonic near-field scattering can be obtained [31], [51]. Therefore, pseudoheterodyne

interferometric detection allows for obtaining background-free near-field information [52], [53].

4.3 Theory of s-SNOM

It was described in chapter 4.2 that the tip-sample interaction (referred as near-field interaction) yields a near-field scattering that contains information about the local optical properties of the sample. In order to understand the signal measured in s-SNOM and get useful information about the sample, a theoretical model of the near-field interaction is required. A simple model that allows for understanding the near-field interaction and provides a qualitative explanation of almost all phenomena experimentally observed in s-SNOM is the *point dipole model* (PDM), which will be described in the following (adapted from [3]). The PDM is illustrated in Fig. 4.6.

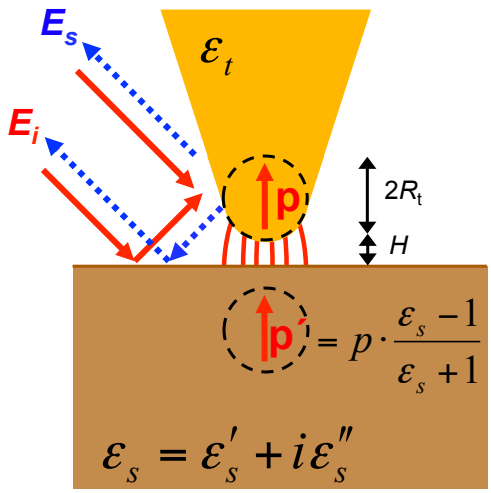

Fig. 4.6: **Illustration of the PDM model for s-SNOM**. The incident electric field E_i creates a dipole p in the metallic AFM-tip, which is described by a sphere. The near-field interaction with the sample is described with a mirror dipole p' at the sample.

Let the incident field focused onto the tip be E_i, and the scattered field be E_s. The ratio between E_i and E_s is called the *scattering coefficient,* $\sigma = E_s/E_i$ [44]. For simplicity, let us consider that the near-field scattering is the only contribution to the total scattered field, $E_s = E_{nf}$. The field at the tip location can be written as $(1 + r_s)E_i$, where r_s is the reflection coefficient that accounts for the reflection of the field at the sample surface. This field polarizes the tip yielding an effective dipole moment $P = \alpha_{\text{eff}}(1 + r_s)E_i$, where α_{eff} is the effective polarizability of the tip. The effective polarizability α_{eff} is a key parameter as it accounts for the near-field interaction between the tip and the sample, and therefore introduces the optical properties of the sample into the model. By reciprocity, the radiation back-scattered by this effective dipole into the far field is given

by $E_s = (1 + r_s)P$, because again the dipole back-scatters directly and via reflection at the sample surface [44], [54], [55]. The complex-valued scattering coefficient thus is given by

$$se^{i\varphi} = \sigma = \frac{E_s}{E_i} \propto \alpha_{\text{eff}}(1 + r_s)^2 \tag{4.6}$$

where s and φ are the amplitude and phase of the scattering coefficient. Note, that the scattering coefficient is complex-valued, as the tip-sample interaction produces a phase difference between E_s and E_i when the imaginary part of the sample permittivity is not equal to zero.

The PDM regards the tip as a point dipole p with a polarizability corresponding to that of a small sphere of radius R_t and polarizability α_t, which is given by

$$\alpha_t = 4\pi {R_t}^3 \frac{\varepsilon_t - 1}{\varepsilon_t + 2} \tag{4.7}$$

with ε_t being the permittivity of the tip material. The point dipole of the tip generates a mirror dipole $p' = p(\varepsilon_s - 1)/(\varepsilon_s + 1)$ in the sample, which interacts with the tip dipole p. Quasi-static solution of the scattering problem yields the effective polarizability of the tip dipole

$$\alpha_{\text{eff}} = \frac{\alpha_t}{1 - \frac{\alpha_t \beta}{16\pi(H + R_t)^3}} \tag{4.8}$$

where H is the tip height above the sample surface. β is the *quasi-static reflection coefficient* that depends only on the sample permittivity ε_s and writes:

$$\beta = \frac{(\varepsilon_s - 1)}{(\varepsilon_s + 1)} \tag{4.9}$$

Eq. (4.6), (4.8) and (4.9) show how the scattered field E_s is related to the sample permittivity, ε_s, assuming that $E_s = E_{nf}$. However, in practice the scattered field E_s also contains a strong background contribution E_{bg} and thus, $E_s \neq E_{nf}$. However pseudoheterodyne interferometric detection (see chapter 4.2.4) allows for removing the background contribution by measuring the n$^{\text{th}}$ harmonic near-field signal E_n (note that $E_n \approx E_{nf,n}$), which following eq. (4.6) is given by

$$E_n = \sigma_n E_i \propto \alpha_{\text{eff},n}(1 + r_s)^2 E_i \quad \textbf{(4.10)}$$

where σ_n and $\alpha_{\text{eff,n}}$ are the n$^{\text{th}}$ order Fourier coefficients of σ and α_{eff}, respectively.

While recording an s-SNOM image, the incident field E_i is constant and therefore $E_n \propto \sigma_n$. Consequently, the measured n$^{\text{th}}$ order amplitude and phase are usually referred as to s_n and φ_n, respectively.

Furthermore, while scanning over different materials on a sample, all parameters that affect the near-field scattering, except the sample permittivity, are ideally constant (i.e. the incident field, reflection coefficient at the sample, tip permittivity, tip height modulation, etc.). Therefore, the permittivity of the sample is in good approximation the only parameter responsible for contrast mechanism in s-SNOM imaging. Comparison of E_n at different materials within an s–SNOM image yields useful information about their relative permittivity, ε_s.

More advanced theoretical models than the PDM have been developed, which provide predictions that compare better with experimental data, especially for samples exhibiting strong resonances (i.e. phonons or plasmon polaritons). Different models are discussed in detail in ref. [31].

4.4 Experimental setup

In this thesis, a commercial s-SNOM (NeaSNOM, neaspec.com) was used to perform both s-SNOM and nano-FTIR measurements. The nano-FTIR technique will be introduced in chapter 5. The scheme of the microscope setup is illustrated in Fig. 4.7.

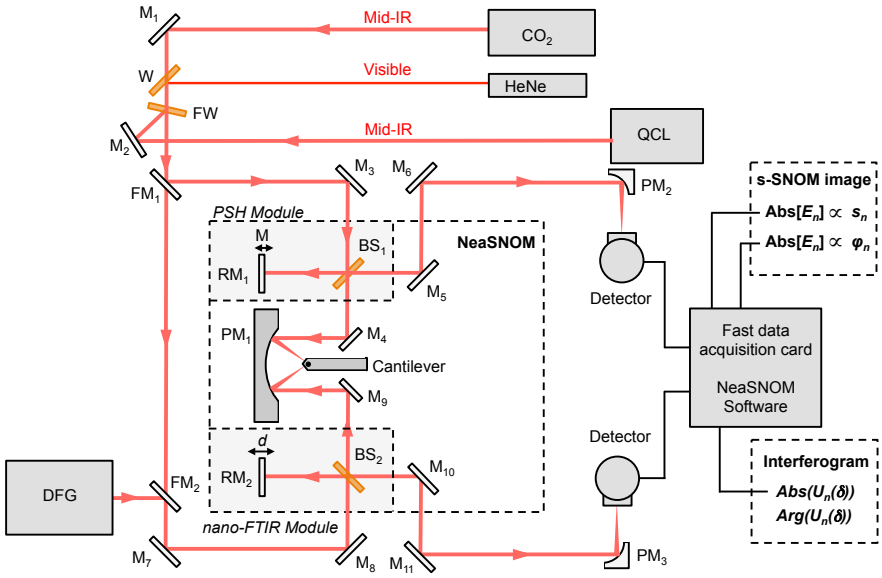

Fig. 4.7: **Microscope setup used in this thesis**. It comprises a NeaSNOM microscope, two beamsplitters, two moving reference mirrors and two detectors (one at each side of the microscope), a DFG based broadband laser (used for nano-FTIR), one CO_2 laser and one QCL laser (used for s-SNOM), one HeNe laser (used for alignment purposes), one computer (with the NeaSNOM software and the data acquisition card) and several optical components (e.g. mirrors and windows) that allow for selecting and directing the different lasers.

The sample is placed below a conventional (commercially available) cantilevered AFM tip (marked with a black dot in Fig. 4.7). The microscope has two modules, that is, the pseudoheterodyne (PSH) module and the nano-FTIR module. Each module is located at one side of the microscope and comprises an independent asymmetric Michelson interferometer. For s-SNOM imaging, the monochromatic infrared radiation from a laser is coupled into the PSH module, while for nano-FTIR the broadband infrared radiation from the DFG is coupled into the nano-FTIR module. The radiation coming from any of the two modules is focused onto the AFM tip using a parabolic mirror (PM_1).

The reference mirror (RM_1) of the PSH module is mounted on a piezo actuator, which is driven at 450 Hz with an amplitude of a few micrometers to perform pseudoheterodyne interferometric detection. In the nano-FTIR module, the reference mirror (RM_2) is mounted on a piezo-driven linear stage, which can be moved linearly at constant velocity for 1600 micrometers to perform FTIR spectroscopy. The beamsplitter BS_1 is made of ZnSe and has an antireflection coating at 10.2 µm wavelength, while the beamsplitter BS_2 was an uncoated ZnSe beamsplitter. For all measurements presented in this thesis, commercial cantilevered Au-coated cantilevered tips (PPP-NCSTAu, Nanosensors) with mechanical resonance frequencies around $\Omega \sim 135$kHz were used.

The reason why we use different detection modules depending on the operation mode (i.e. s-SNOM or nano-FTIR) is merely technical and relies on the fact that the

requirements for the reference mirror movement are completely different for each operation mode. A single piezo actuator cannot vibrate at a high frequency of some hundreds of Hertz (required for pseudoheterodyne interferometric detection) and at the same time move slowly over hundreds of micrometers (required for nano-FTIR). Therefore, two different piezo actuators are used in each module.

To measure the intensity of the output beams coming from the PSH and nano-FTIR modules, independent liquid nitrogen cooled HgCdTe detectors were used (see Fig. 4.7). For the PSH module the detector "KMPV8-0.5-J1" (Kolmar technologies) was used, while for the nano-FTIR module the detector "FTIR-16-0.10" (Infrared Associates, Inc.) was used. The signal provided by the detectors is measured by a fast data acquisition card and processed by the NeaSNOM software. When using the PSH module, the software delivers the amplitude and phase of the nth order demodulated signal, E_n, which is proportional to the amplitude s_n and phase φ_n of the nth order scattering coefficient σ_n, respectively (see chapter 4.2.4). The recording of both signals (while the tip is scanned over the sample surface) yields optical amplitude and phase images. When using the nano-FTIR module, the software delivers the amplitude and phase of the nth order demodulated detector signal, respectively. This signal is recorded for a fixed tip position while the reference mirror position d moves linearly, yielding the interferogram $U_n(\delta)$, where $\delta = 2\Delta d$. For the analysis and processing of the recorded interferograms, the software *Wolfram Mathematica 8* was used in chapter 6, and the software *MATLAB R2014a* in chapters 7 and 8. Note that all s-SNOM and nano-FTIR data shown in this thesis were obtained by signal demodulation at order $n = 3$, except for the nano-FTIR absorption spectrum shown in Fig. 6.4 where it was $n = 2$.

In order to perform s-SNOM measurements with infrared radiation at different frequencies, a CO_2 laser and a quantum cascade laser (QCL) were installed. Furthermore, a visible red beam generated by a HeNe laser was also installed, which was used for alignment purposes. The three lasers were overlapped and by flipping specific mirrors and windows the desired laser could be selected and coupled into the PSH module. In this thesis, we exclusively used the QCL laser (QCL, Daylight Solutions, USA), which is tunable between 1560 cm^{-1} and 1750 cm^{-1} in steps of 0.01 cm^{-1}.

For nano-FTIR, a broadband laser based on a difference frequency generator (DFG, Lasnix, Germany) was installed. The DFG laser generates a broadband coherent mid-infrared laser beam by synchronously superimposing two pulsed near-infrared beams in a GaSe crystal [56]–[58]. The broadband mid-infrared laser beam was guided and coupled into the nano-FTIR module of the NeaSNOM microscope. We note that for alignment purposes the CO_2, HeNe and QCL lasers can also be coupled into the nano-FTIR module by flipping FM_1 and FM_2 mirrors.

The setup of the DFG laser is shown in Fig. 4.8. The two near-infrared, 100-fs pulse trains were generated by a fiber-laser system (FemtoFiber pro infrared (FFPro-IR) and FFPro-SCIR, Toptica Germany). The FFPro-IR delivers a collimated free-beam with about 350 mW at 1560 nm fundamental wavelength. The FFPro-SCIR uses a portion of

the laser generated by FFPro-IR and provides a supercontinuum generation by using a highly nonlinear fiber that generates a widened spectrum from 980 to 2200 nm. The two near–infrared beams are synchronized by a delay stage and combined by a window (W) and finally focused into a GaSe crystal. In the crystal a broadband coherent mid-infrared beam is obtained. After the GaSe crystal, the beam is collimated by a parabolic mirror (PM).

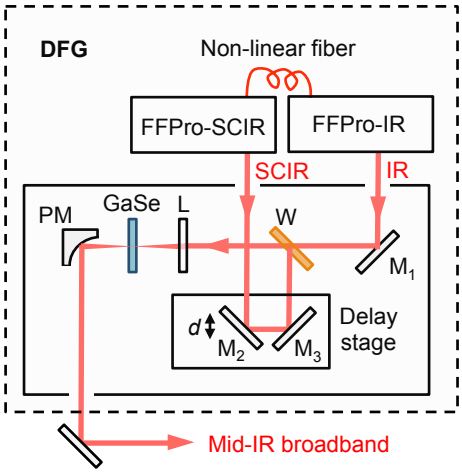

Fig. 4.8: **Setup of the laser based on a difference frequency generator (DFG)**. It comprises a fiber-laser system with two lasers, FFPro-IR and FFPro-SCIR, which emit two near–infrared beams that are synchronized by a delay stage, combined by a window (W) and focused into a GaSe crystal. In the crystal a broadband coherent mid-infrared laser beam is obtained.

In this thesis, two different DFG laser prototypes were used. In chapter 6, a preliminary prototype was used, which provided an infrared laser beam with average output power of about 100-250 μW and a usable width of about 600 cm^{-1}. In chapters 7 and 8, an optimized DFG prototype was used, with an average output power of about 600 μW and a usable spectral bandwidth of about 400 cm^{-1}. The centre frequency of both lasers could be tuned roughly between 1000 and 1700 cm^{-1}, by mainly altering the SCIR output, which can be readily done by adjusting the motorized prism compressor inside the FFPro-SCIR.

5 Fourier transform infrared nanospectroscopy (nano-FTIR)

In this chapter, Fourier transform infrared nanospectroscopy (nano-FTIR) will be introduced. Nano-FTIR combines FTIR spectroscopy (chapter 3) and s-SNOM microscopy (chapter 4), and allows for performing FTIR spectroscopy with nanoscale spatial resolution. The experimental implementation based on an asymmetric Fourier transform spectrometer will be described, as well as the processing of the recorded near-field interferograms that yield the nanoscale infrared spectra.

5.1 Principle of nano-FTIR

Nano-FTIR merges s-SNOM microscopy (see chapter 4) and FTIR spectroscopy (see chapter 3), and allows for performing FTIR spectroscopy with nanoscale resolution. To obtain broadband spectral information, the tip is illuminated by broadband infrared radiation, and FTIR spectroscopy of the backscattered light is performed. To this end, a n^{th} order near-field interferogram, $U_n(\omega)$, is measured by recording the demodulated detector signal (see chapter 5.2) while linearly moving the reference mirror. Because tip and sample are located in one arm of the interferometer (asymmetric Michelson interferometer, see chapter 4.2.4), Fourier transformation of the near-field interferogram $U_n(\omega)$, yields n^{th} order amplitude and phase spectra [57]. Analogue to the pseudoheterodyne detection, demodulation of the detector signal allows for suppressing the background contribution and thus at a sufficiently high harmonic yields $E_n(\omega) \approx E_{nf,n}(\omega)$. However, the spectrum recorded in a nano-FTIR experiment is affected by instrumental characteristics and is given by $E_n(\omega) = \sigma_n(\omega)F(\omega)E_i(\omega)$, where $F(\omega)$ is the response function of the setup, $E_i(\omega)$ is the incident field and $\sigma_n(\omega)$ is the near-field scattering coefficient. Thus, pure information about the near-field scattering coefficient $\sigma_n(\omega)$ is not directly obtained. Still, for simplicity, in this thesis $E_n(\omega)$ is referred as to the *near-field spectrum*.

In order to remove the influence of instrumental characteristics (i.e. $F(\omega)$) the near-field spectra measured on the sample $E_{n,sam}(\omega)$ are normalized by near-field spectra measured on a known substrate. Typically the known substrate is silicon, which is spectrally flat ($\sigma_{n,Si}(\omega) = \text{const}$), yielding $E_{n,Si}(\omega) = const\, F(\omega)E_i(\omega)$. Thus, the near-field contrast of a sample area relative to a reference area is given by

$$\eta_n(\omega) = \frac{E_{n,sam}(\omega)}{E_{n,Si}(\omega)} = \frac{\sigma_{n,sam}(\omega)F(\omega)E_i(\omega)}{const\, F(\omega)E_i(\omega)} \propto \sigma_{n,sam}(\omega) \qquad \textbf{(5.1)}$$

In this thesis, the spectra of the near-field contrast, $\eta_n(\omega)$, that is, normalized *near-field spectra*, will be called *nano-FTIR spectra*. The nano-FTIR amplitude spectrum is thus

given by $s_n = s_{n,sam}/s_{n,Si}$ while the nano-FTIR phase spectrum is given by $\varphi_n = \varphi_{n,sam} - \varphi_{n,Si}$.

In chapter 5.8 it will be shown that the imaginary part of the nano-FTIR spectra, $\mathrm{Im}[\eta_n(\omega)]$, reveals the local infrared absorption of the sample material, and therefore the *nano-FTIR absorption* has been defined as $a_n(\omega) = \mathrm{Im}[\eta_n(\omega)] = s_{n,sam}/s_{Si,n} \sin(\varphi_{n,sam} - \varphi_{Si,n})$ [57], [59].

In the following, the experimental implementation and data processing of nano-FTIR will be described, following the description of chapter 2.3 of ref. [33] and chapter 5 of ref. [3].

5.2 Experimental setup

The nano-FTIR setup (see illustration in Fig. 5.1) is essentially the same as the s-SNOM setup described in chapter 4.2.4. However, for nano-FTIR a broadband laser is used to illuminate the tip. In this thesis, a broadband infrared laser based on a difference frequency generator was used (DFG , Lasnix, Germany, see chapter 4.4 for details).

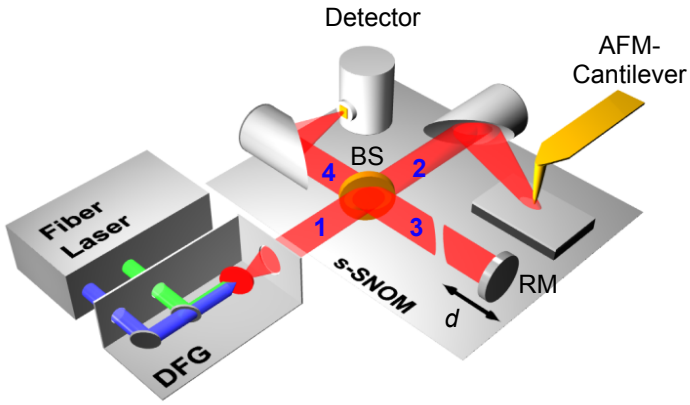

Fig. 5.1: **Schematic nano-FTIR setup**. The metallic tip of a near-field microscope (s-SNOM) is illuminated with a broadband source generated by a laser based on a difference frequency generator (DFG). The backscattered light is analyzed with an asymmetric Michelson interferometer, comprising a beamsplitter (BS), reference mirror (RM) and a detector.

At a fixed position of the tip relative to the sample, the detector signal is recorded while moving the reference mirror at a constant velocity. Due to the tip oscillation, the scattered field and consequently the detector signal are modulated. In order to remove the background contribution, the detector signal is demodulated online with a (software-based) lock-in amplifier, which yields a complex valued output (that is, amplitude and

phase of the modulation).The real part of the demodulated complex-valued lock-in signal yields the interferogram. As an example, in Fig. 5.2 we show the interferogram recorded on a tobacco mosaic virus (TMV, see chapter 6.2 for details), $U_{3,\mathrm{TMV}}(\delta)$. To this end, the tip was positioned on top of the TMV at the position marked by a black dot in the topography image shown in inset of Fig. 5.2. Note that the demodulation order was $n = 3$.

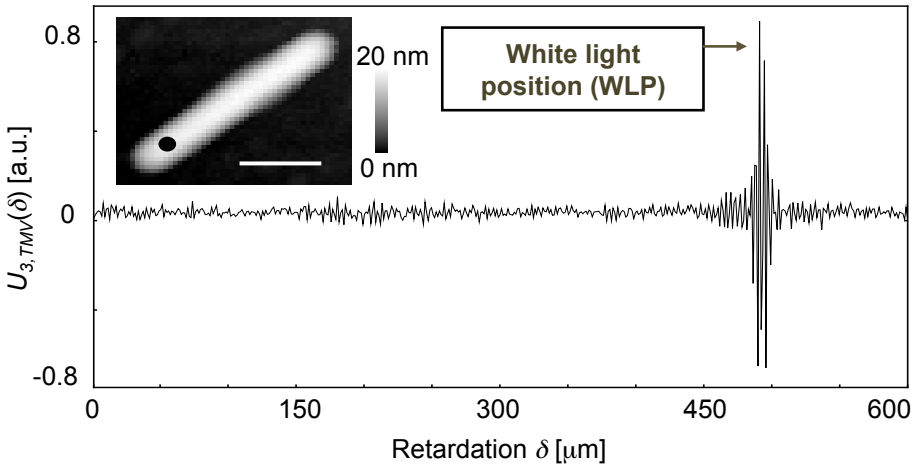

Fig. 5.2: **Near-field interferogram $U_{3,\mathrm{TMV}}(\delta)$ recorded at TMV**. The tip was positioned on top of the TMV at the position marked by a black dot in the topography image shown in the inset (scale bar, 100 nm), while the demodulated interferogram was recorded. Total retardation was $\delta = 1200\mu\mathrm{m}$ and number of data points was $N = 512$. The tapping amplitude was 50 nm and the acquisition time of each data point was 65 ms, the acquisition time of a complete near-field interferogram was 33 s.

Note that contrary to conventional FTIR spectroscopy , the near-field interferogram shown in Fig. 5.2 was recorded with the WLP not centered. This is because of the asymmetric spectrometer design, and will be describe in chapter 7.3.

Fourier transformation of the interferogram $U_3(\delta)$ yields the complex-valued near-field spectrum $E_3(\omega)$. The amplitude and phase of the near-field spectrum of TMV are shown in Fig. 5.3.

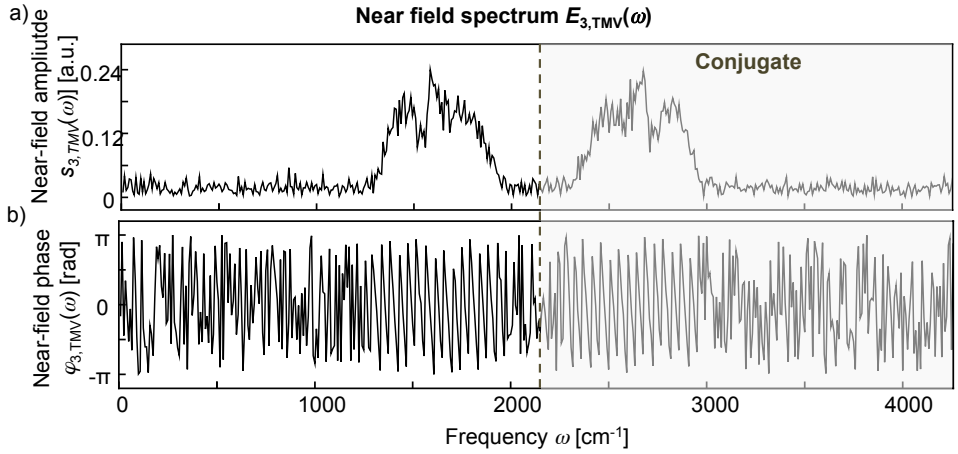

Fig. 5.3: **Near-field spectrum of TMV**. **(a)** Near-field amplitude spectrum $s_{3,TMV}$ and **(b)** near-field phase spectrum $\varphi_{3,TMV}$ of TMV obtained by FT of the near-field interferogram shown in Fig. 5.2.

5.3 Normalization

The near-field spectrum recorded at the sample needs to be normalized in order to remove the influence of instrumental characteristics. Similar to GI-FTIR spectroscopy (see chapter 3.4.2), a reference near-field spectrum is recorded on a known substrate, which is spectrally flat (i.e. has no spectral absorption peaks). For the mid-IR spectral region, silicon or gold are suitable substrates. Importantly, the reference near-field spectrum needs to be recorded with the same settings as the sample near-field spectrum (e.g. same tip, same tapping amplitude, same illumination, same alignment, same processing of the interferogram, etc.)

The near-field spectra measured on TMV and silicon, $E_{3,TMV}(\omega)$ and $E_{3,Si}(\omega)$, respectively, are shown in Fig. 5.4a (black and red graphs, respectively). They were recorded at the points marked by black and red dots, respectively, in inset of Fig. 5.4a. By normalization, the nano-FTIR amplitude spectrum $s_3 = s_{3,TMV}/s_{3,Si}$ and the nano-FTIR phase spectrum $\varphi_3 = \varphi_{3,TMV} - \varphi_{3,Si}$ of TMV were obtained (Fig. 5.4b). Note that due to the low SNR, no clear spectral features are observed in the obtained normalized spectra. Analogue to conventional FTIR spectroscopy averaging over several interferograms needs to be done in order to improve the SNR. The averaging procedure will be described in the following.

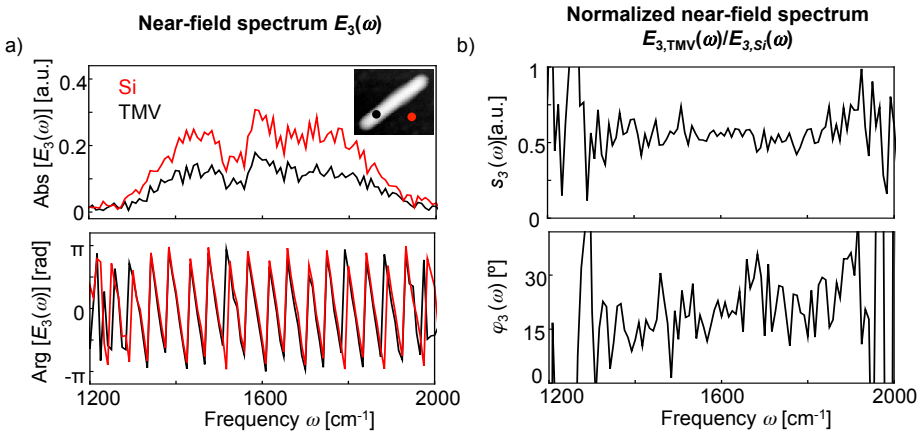

Fig. 5.4: **Normalization of the near-field spectrum of TMV**. **(a)** Near-field amplitude and phase spectra of TMV (black) and Silicon (red), which were recorded on black and red dots, respectively, marked in the topography image shown in inset of Fig. 5.4a. Scale bar, 100 nm. **(b)** Normalized near-field amplitude and phase spectra (i.e. nano-FTIR amplitude and phase spectra) of TMV. The near-field spectra recorded at silicon were used as reference spectra for normalization.

5.4 Averaging

To improve the SNR of nano-FTIR spectra, several interferograms are typically measured both at the sample and at the reference. The relative position of the tip and the sample is subject to unavoidable drift in the range of several nanometers per minute (see chapter 7.4 for more details). On the other hand, the recording of several interferograms may take several minutes. Thus, in order to record several interferograms in one and the same location, the sample drift needs to be corrected by sample re-positioning. The procedure for sample re-positioning will be explained in detail in chapter 7.4. Note that re-positioning is usually not needed at the reference because large areas of silicon are usually available. For TMV, 60 interferograms were measured both on TMV and on silicon. All 60 interferograms were averaged, yielding one interferogram for each location. Fourier transformation and normalization was applied as described in chapters 5.2 and 5.3, respectively. In order to see how the averaging improves the SNR, the nano-FTIR amplitude s_3 and phase φ_3 spectra of TMV obtained by averaging over different amount of interferograms are shown in Fig. 5.5. The SNR of both nano-FTIR amplitude and phase spectra improves with averaging, and the expected amide I and amide II absorption bands (marked in Fig. 5.5c) are clearly resolved. See chapter 6.4.1 for discussion of the Amide bands.

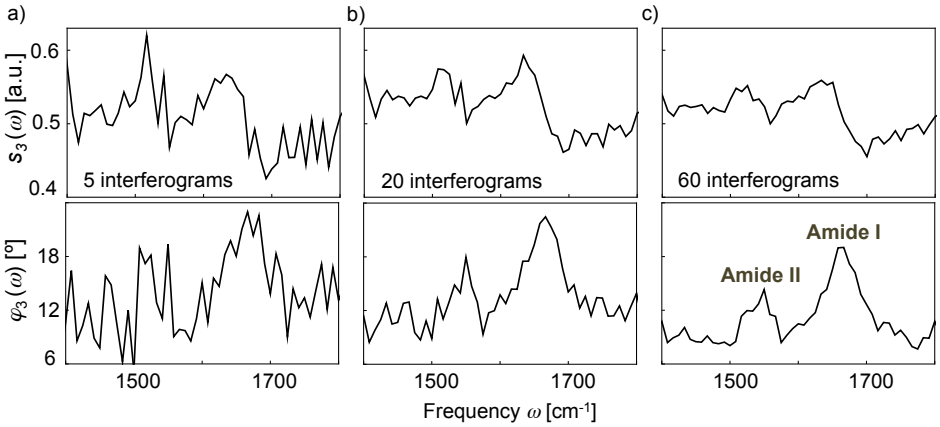

Fig. 5.5: **Averaging of nano-FTIR spectra**. Nano-FTIR amplitude $s_3 = s_{3,TMV}/s_{3,Si}$ and phase $\varphi_3 = \varphi_{3,TMV} - \varphi_{3,Si}$ spectra at TMV averaged over 5 **(a)**, 20 **(b)** and 60 **(c)** interferograms. The total acquisition time was 6.3, 25.3 and 76 minutes, respectively.

5.5 Zero filling

Analogue to conventional FTIR spectroscopy, zero filling (see chapter 3.3) can be applied to extend near-field interferograms recorded in nano-FTIR. As an example, in Fig. 5.6a the three times extended near-field interferogram of TMV is shown. In Fig. 5.6b, Fig. 5.6c and Fig. 5.6c the nano-FTIR amplitude and phase spectra obtained with no extension (red squares), three times extension (green circles) and fifteen times extension (black line), respectively, are shown. It can be seen that different extensions result in nano-FTIR spectra with different amount of data points.

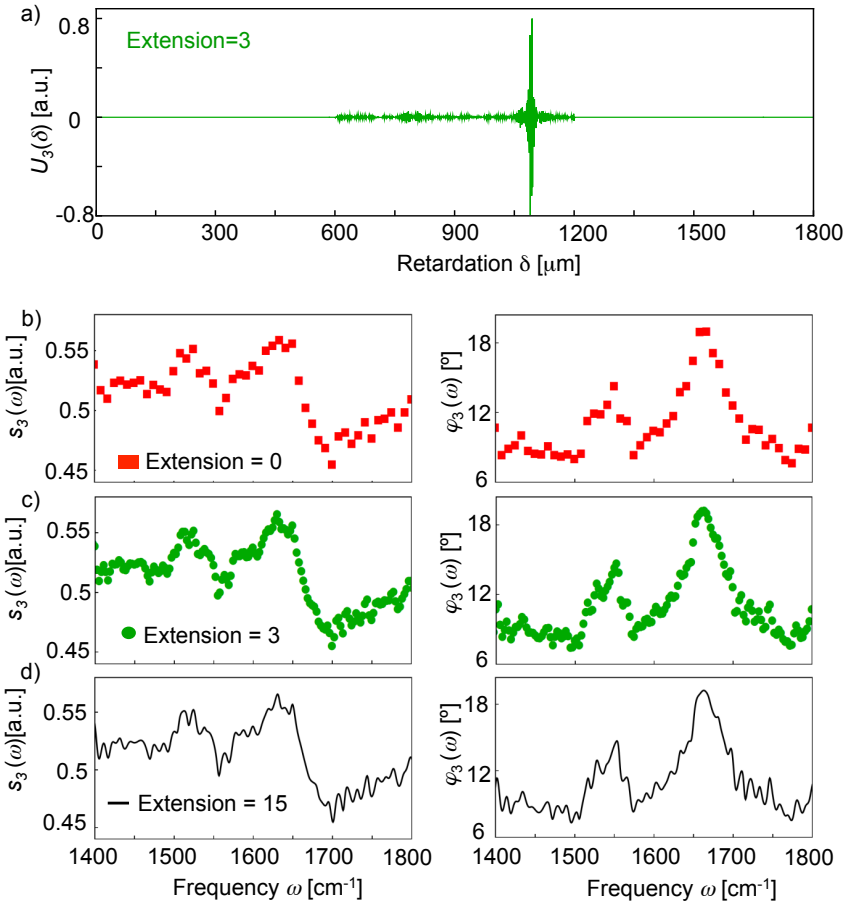

Fig. 5.6: **Zero filling in nano-FTIR**. **(a)** 3 times extended interferogram. **(b)** Nano-FTIR amplitude (left) and phase (right) spectra obtained by no extension (red squares), **(b)** 3 times extended (green circles) and **(c)** 15 times extended (black line) interferograms.

5.6 Apodization

Apodization (see details in chapter 3.3) is also applied to the near-field interferogram. In all apodization functions applied in this thesis, a "*Blackman-harris 3 term*" function was used, which is given by

$$\mathrm{D}(\delta) = 0.42 - 0.5\cos\left(\frac{2\pi\delta}{\delta_t}\right) - 0.08\cos\left(\frac{2\pi\delta}{\delta_t}\right) \qquad \textbf{(5.1)}$$

In order to take advantage of the high SNR of the interferogram near the WLP, an asymmetric apodization function was applied, which has a value of 1 at the WLP and decreases down to a value of zero at maximum and minimum retardation (i.e. edges of the interferogram). The used asymmetric "*Blackman-harris 3 term*" function is shown in Fig. 5.7a (red) together with the raw recorded interferogram (gray) and the apodized

interferogram (black). Note that for better visibility the raw recorded interferogram (gray) is vertically offset. Fig. 5.7b and Fig. 5.7c show the nano-FTIR amplitude and phase spectra (black), respectively, obtained from the apodized interferogram. For comparison the nano-FTIR spectra obtained from the raw interferogram are also shown (gray, already shown in Fig. 5.6d). Note that apart from the apodization, 15 times zero-filling was applied to the interferograms before Fourier transformation and normalization.

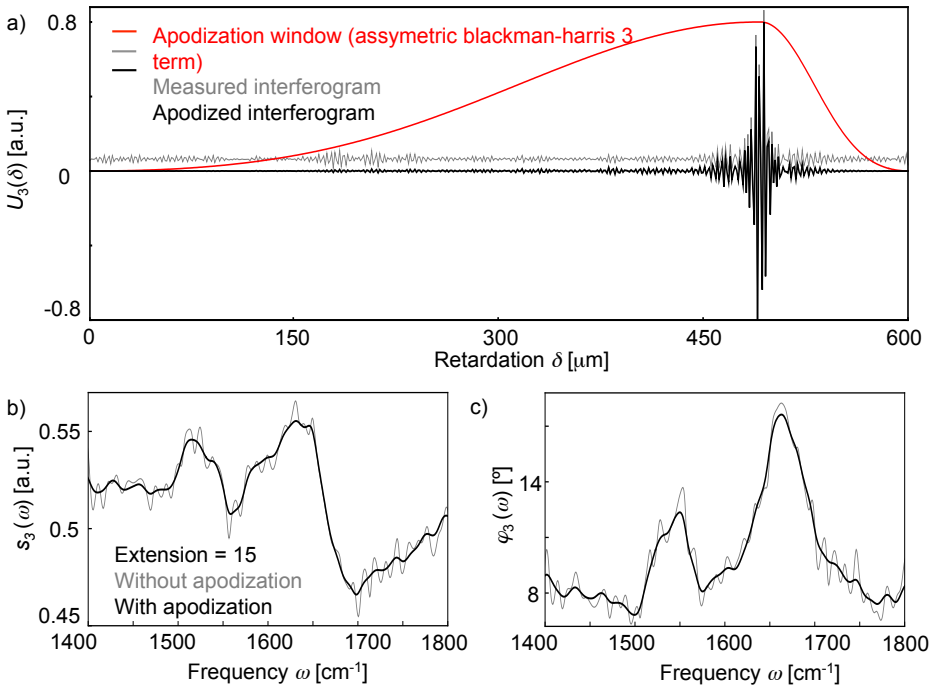

Fig. 5.7: **Apodization in nano-FTIR**. **(a)** Apodization function (red) and the raw (gray) and apodized (black) interferograms. **(b)** Nano-FTIR amplitude and **(c)** phase spectra obtained with and without apodization (black and gray, respectively).

5.7 Baseline Correction

The baseline of nano-FTIR phase spectra can be tilted around $\omega = 0$ cm^{-1}. The origin of this tilting is discussed in detail in chapter 7.6. Throughout this thesis, we correct the phase spectra by defining two frequencies at which it is known that the sample is not absorbing. For the nano-FTIR phase spectrum of TMV, the frequencies 1500 cm^{-1} and 1775 cm^{-1} were selected and the linear baseline correction was applied so that the nano-FTIR phase at these frequencies is zero. The baseline-corrected nano-FTIR phase spectra of TMV is shown in Fig. 5.8.

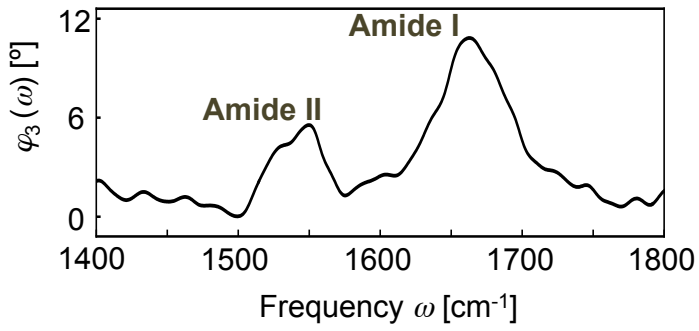

Fig. 5.8: **Nano-FTIR phase spectra of TMV obtained after baseline correction**.

5.8 Theory of nano-FTIR

It was shown in eq. (5.1), that the nano-FTIR spectrum is proportional to the spectrum of the near-field scattering coefficient $\eta_n(\omega) \propto \sigma_n(\omega)$. Further, according to the point dipole model (PDM) described in chapter 4.3, the scattering coefficient has the following structure:

$$\sigma(\omega, H) \propto \alpha_{\text{eff}}(f \cdot \beta)(1 + r_s)^2 \tag{5.2}$$

where α_{eff} is the effective polarizability of the tip and r_s is the far-field reflection coefficient of the sample surface (see eq. (4.6)). $\beta = \beta(\omega) = (\varepsilon_s - 1)/(\varepsilon_s + 1)$ is the quasi static reflection coefficient that depends only on the sample permittivity ε_s and $f = f(H)$ is a frequency–independent function of the tip-sample distance H.

It can be shown [59] that for a thin organic film with weak molecular vibrational resonances (i.e. TMV) $\sigma(\omega, H)$ can be expanded into a Taylor series, which to the first order in $(f \cdot \beta)$ yields:

$$\sigma(\omega, H) \approx [\alpha_0 + \alpha_1 \cdot f(H) \cdot \beta(\omega)](1 + r_s)^2 \tag{5.3}$$

where α_0 and α_1 are frequency- and height-independent constants. Due to the demodulation of the detector signal all height-dependent terms vanish, while due to the normalization to a spectrum of Si, the influence of r_s also vanishes, yielding

$$\sigma_n(\omega) \propto \beta(\omega) \tag{5.4}$$

Thus, the recorded nano-FTIR spectrum is determined exclusively by the local dielectric function of the sample $\varepsilon_s(\omega)$, which in principle allows for the derivation of the

imaginary part of the complex-valued refractive index (i.e. the absorption index). For weak molecular vibrations, we can write in good first approximation [59] that

$$\kappa(\omega) = \mathrm{Im}[\varepsilon(\omega)^{\frac{1}{2}}] \sim \mathrm{Im}[\beta(\omega)] \propto \mathrm{Im}[\sigma_n(\omega)] \propto \mathrm{Im}[\eta_n(\omega)]. \quad \textbf{(5.5)}$$

Thus, the *nano-FTIR absorption* has been defined as $a_n(\omega) = \mathrm{Im}[\eta_n(\omega)] = s_{sam,n}/s_{Si,n} \sin(\varphi_{sam,n} - \varphi_{Si,n})$.

6 Structural analysis and mapping of individual protein complexes by infrared nanospectroscopy

In this chapter we introduce mapping of protein structure with 30nm lateral resolution and sensitivity to individual protein complexes by nano-FTIR. We present local broadband spectra of one virus, ferritin complexes, purple membranes and insulin aggregates, which can be interpreted in terms of their α-helical and/or β-sheet structure. Applying nano-FTIR for studying insulin fibrils—a model system widely used in neurodegenerative disease research—we find clear evidence that 3-nm-thin amyloid-like fibrils contain a large amount of a-helical structure. This reveals the surprisingly high level of protein organization in the fibril's periphery, which might explain why fibrils associate.

6.1 Introduction

Fourier transform infrared (FTIR) spectroscopy allows for the analysis of chemical bonds, protein morphology or secondary structure [60]–[63]. Applications include the tracing of protein modifications that may originate from interactions with other biomaterials (e.g. cellular receptors, enzymatic cofactor) [64] or inorganic matter (e.g. heavy metal ions, nanoparticles) [65]. Such interactions are of high relevance in various physiological cellular processes (e.g. cellular attachment, genomic regulation), pathological processes of a large variety of diseases (e.g. viral infection, neurodegenerative diseases) [66], [67], as well as in biomedical diagnostics and equipment (e.g. support for human cell culture) [68]. The analysis of amide vibrations provides valuable insights into the secondary structures of proteins, revealing information regarding conformation and folding [62], [69]–[71]. In particular, the peak position of the Amide I absorption band, provides information about the secondary structure of proteins. However, due to the diffraction-limited resolution of FTIR spectroscopy, infrared spectroscopy applications on the nanometer scale or even single molecule level have so far proved elusive.

The diffraction- limited resolution of FTIR spectroscopy is circumvented by Fourier transform infrared nanospectroscopy (nano-FTIR) [43], [56], [57], [59], [72], [73] as described in chapter 5. However, broadband nano-FTIR spectra of protein complexes have neither been observed so far, nor shown to be suitable for the analysis of their structure. Biological objects including protein fibrils and membranes have been studied only by s-SNOM imaging at selected wavelengths [74]–[78] and it has not been demonstrated that the most important secondary structures - α-helical and β-sheet structures - can be identified on the level of individual protein complexes.

In this chapter we demonstrate that nano-FTIR can probe protein secondary structure on the nanometer scale and with sensitivity to individual protein complexes. To this end, we have chosen to study the amide bands of individual tobacco mosaic viruses (TMVs) and ferritin complexes [79] for their well-defined, robust and dominantly α-helical

protein structure [80], insulin aggregates for exhibiting β-sheet structure [81] and purple membranes (PMs) because of the well-defined orientation of the transmembrane α-helices [82]. Broadband infrared spectra of a ferritin complex indicate that nano-FTIR is sensitive to about 4,000 amino acids, corresponding to about 5,000 C=O and N-H bonds, respectively. Most importantly, by comparing nano-FTIR spectra to standard far-field FTIR spectra, we find that the amide I band in the nano-FTIR spectra can be analysed and interpreted in the framework of standard infrared spectroscopy. Our studies establish a solid foundation for infrared nanobiospectroscopy, which is a prerequisite for nano-FTIR applications in biochemical and biomedical research. We demonstrate the potential for real-life applications of nano-FTIR in these fields by exploring the still not fully clarified protein conformation in individual insulin fibrils.

6.2 Sample preparation

In the following we introduce the biological objects studied in this chapter, and how sample preparation was performed. All samples were prepared using DI ultrapure (18 MΩcm) water. Substrate surfaces were used as provided by the supplier, but in some cases they were additionally cleaned by ultrasonication in acetone, isopropanol, and water (each for 10 min), and blow-dried with nitrogen. For all s-SNOM and nano-FTIR measurements, all samples were prepared on silicon wafers. For GI-FTIR spectroscopy measurements, the samples were prepared on gold substrates (150 nm of thermally evaporated gold deposited on a silicon wafer), while for transmission-FTIR -and ATR-FTIR spectroscopy measurements the samples were prepared on CaF2 and silicon substrates, respectively.

TMV samples

The TMV is a well-defined protein complex of 18 nm diameter and about 300 nm length and it consist of 2140 identical proteins assembled helically around an RNA strand [80]. The capside proteins are composed of five α-helixes and four short β-sheets resulting in dominantly α-helix content. A suspension of TMV (strain *vulgare*), purified from systemically infected tobacco plants (*Nicotiana tabacum cv Samsun nn*) was kindly provided by Prof. C. Wege (University of Stuttgart, Germany). TMV was dialyzed against water in a 10kDa Slide-A-Lyzer dialysis unit (Thermo Fisher Scientific), and diluted with water (DI ultrapure,18 MΩcm).

TMV sample for transmission-FTIR spectroscopy: 10 μl of 1 μg/ml suspension were deposited on a CaF2 wafer, and dried in air by Simon Poly from the Nanobiomechanics group at CIC nanoGUNE.

TMV sample for GI-FTIR spectroscopy: 10 μl of 1 μg/ml suspension were spin-coated (spin coater SCI-20, Schaefer Technologie) on a gold wafer (40 nm of thermally evaporated gold deposited on a silicon wafer), and dried in air by Wiwat Nuansing from the Self-Assembly group at CIC nanoGUNE.

TMV sample for s-SNOM: 10 μl of 1 μg/ml suspension were spin-coated on a cleaned undoped silicon wafer and dried in air by Simon Poly from the Nanobiomechanics group at CIC nanoGUNE.

Ferritin samples

Ferritin is a globular protein complex of 12 nm in diameter and comprises 24 subunits that form a cage around a ferrihydrite nanoparticle. Each ferritin subunit is composed of six α-helixes and one β-sheet [79]. Horse spleen ferritin solution (44 mg ml^{-1}, Sigma-Aldrich) was diluted 500-fold with water.

Ferritin sample for s-SNOM: A droplet of Ferritin solution was deposited on a silicon wafer and incubated for 2 min. Excess of solution was removed with filter paper (Sigma) and the sample was dried in air.

Ferritin sample for GI-FTIR spectroscopy: Ferritin solution was first purified with a spin desalting column (7K MWCO, Thermo Scientific) and followed with the procedure as above, but on a gold substrate.

Purple membrane samples

Purple membrane (PM) of *Halobacterium salinarum* is composed of a double layer of polar and neutral lipids, and the integral membrane protein bacteriorhodopsin. The secondary structure of bacteriorhodopsin comprises seven transmembrane α-helices and an extracellular β-sheet [82].

Halobacteria (H. salinarum strain S9) were cultivated in high salt pepton medium (10 g L^{-1} pepton, 4.3 M NaCl, 80 mM MgSO4, 27 mM KCl, 10 mM sodium citrate, pH 6.5) for 6 days. The collected cells were lysed by osmotic shock with distilled water. Purple membrane fragments were purified by fractionated centrifugation [83].

Purple membrane for s-SNOM: A 30 μl droplet of an imaging buffer pH7.8, containing 150 mM of KCl and 20 mM of TRIS, was deposited on a silicon substrate, and 0.2 μl of purified purple membrane (6 mg ml^{-1}) was added into the droplet. 15 μl of imaging buffer were subsequently added into the droplet to ensure maximum dispersion of previously added purple membranes. The resulting droplet was incubated on the silicon substrate for 25 minutes and then rinsed several times with water and dried in air.

Purple membrane for GI-FTIR spectroscopy: Same sample preparation procedure as for s-SNOM, but a gold substrate was used and the purple membrane was incubated for 40 minutes.

Insulin aggregate samples

Insulin aggregates are composed of essentially two β-sheets [81]. Insulin dispersions were prepared solubilizing 20 mg dehydrated human insulin (Sigma-Aldrich) in 1 ml 1

mM HCl solution. The solution was then re-diluted in 10 mM HCl/KCl at 2 mg/ml, and incubated at 60°C for 24 hours in a thermomixer (Eppendorf), followed by 2 years storage at 4°C.

Insulin aggregates (+ TMV) for s-SNOM: 10 μl of insulin aggregate solution were spin-coated (as for TMV) on a silicon substrate, and rinsed with water. 10 μl of 1 μg ml^{-1} TMV suspension were then spin-coated on the dried insulin aggregates.

Insulin aggregates for ATR-FTIR spectroscopy: 20 μl of insulin aggregate solution were deposited on a silicon wafer, dried, and rinsed with water.

Insulin fibril samples

Insulin fibrils are amyloid-like fibrils composed of filament-shaped protein aggregates [70], [81], [84]. Insulin dispersions were prepared as above, but incubated at 60°C for 30 hours.

Insulin fibrils for s-SNOM: 10 μl of insulin fibril solution were spin-coated on a silicon wafer, and rinsed with water.

Insulin monomer samples

Insulin monomers are composed of predominantly α-helical structure. Insulin dispersions were prepared as above, but without any incubation.

Insulin monomer for GI-FTIR spectroscopy: 20 μl of insulin monomer solution were spin-coated on a gold substrate, and rinsed with water.

6.3 Far-field characterization

FTIR spectroscopy

For the far-field FTIR spectroscopy measurements we used a Bruker Hyperion 2000 microscope coupled to a Vertex 70 transmission mode FTIR spectrometer equipped with grazing incidence (GI) and attenuated total reflectance (ATR) modules and a liquid-nitrogen cooled mid-band MCT detector. All FTIR spectra shown in this thesis show the absorbance and were measured with a spectral resolution of 4 cm^{-1} and present an average over 1000 scans with a total acquisition time of 860 s.

Transmission-FTIR spectroscopy. Sample and reference spectra were recorded on calcium floride (CaF_2) with and without the sample, respectively.

GI-FTIR spectroscopy. The GI module (15x GIR objective, Bruker) comprises a plane mirror that reflects the beam onto the sample surface at grazing angle incidence. The reflected beam is backreflected and refocused onto the same sample area and then collected and detected. Sample and reference spectra were recorded on a 150 nm thick gold film on silicon, with and without the sample, respectively.

ATR-FTIR spectroscopy. The ATR module (20x ATR objective, Bruker, single internal reflection) comprises a germanium crystal with a diameter of about 100 μm at the point of contact with the sample. Sample and reference spectra were recorded on a 150 nm thick gold film on silicon wafer, with and without the sample, respectively.

Circular dichroism (CD)

For the recording of CD spectra we used a Jasco J-815 CD spectrometer and a cell with a 1 mm optical pathlength. From CD spectra of the sample solutions we subtracted the solvent CD spectrum. The spectra are the result of averaging 36 scans, recorded at room temperature.

6.4 Setting the foundations for protein analysis with nano-FTIR

6.4.1 Nanoscale broadband infrared spectra of the amide I and II bands

We first verify the ability of nano-FTIR to measure nanoscale broadband infrared spectra of the amide I and II bands over the range from 1400 to 1800 cm^{-1}. To that end, we studied tobacco mosaic viruses (Fig. 6.1a), which have a dominantly α-helical structure (see chapter 6.2 for detailed description). Fig. 6.1c shows near-field infrared phase φ images taken at 1660 cm^{-1} and 1720 cm^{-1}, that is, on and off resonance with the amide I vibration. At 1660 cm^{-1} the phase image exhibits strong contrast owing to the amide I absorption [74]. As expected, the phase contrast vanishes when the illumination is tuned to 1720 cm^{-1}, where the protein does not absorb. By recording nano-FTIR amplitude $s(\omega)$ and phase $\varphi(\omega)$ spectra on top of the virus (position marked by the red dot in the topography image) and normalizing them to those taken on a clean silicon area, we obtained the local infrared absorption spectrum a of TMV (red spectrum in Fig. 6.1d). The local absorption spectrum of TMV reveals the amide I and amide II bands. The Amide I band is associated with combinations of C=O stretching with C-N-H bending vibrations, while the Amide II band is associated with combinations of C-N stretching with C-N-H bending vibrations.

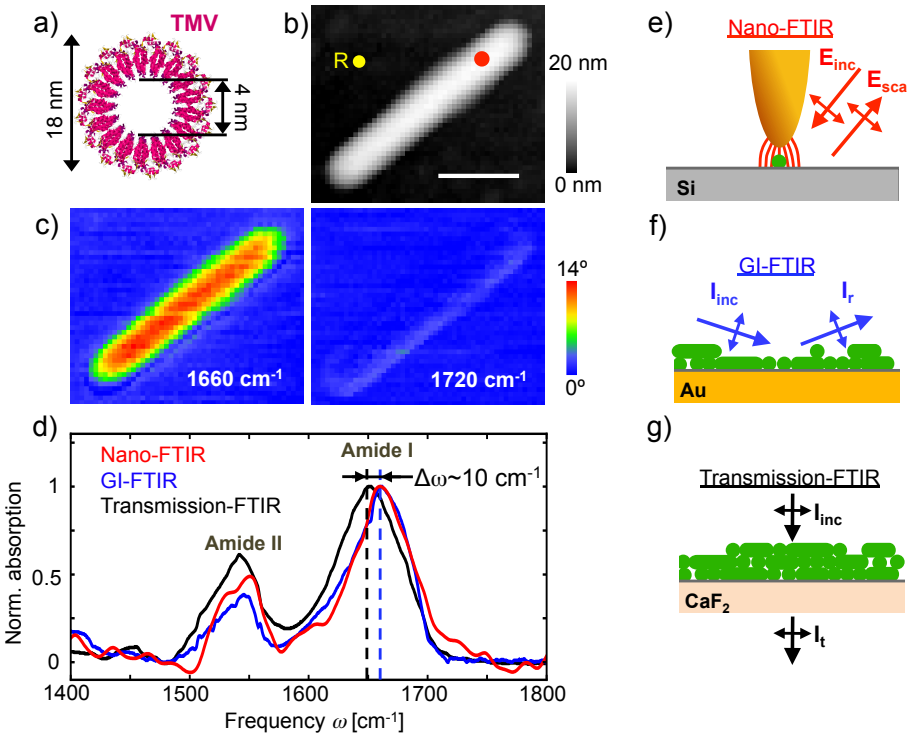

Fig. 6.1: **Infrared nanospectroscopy of tobacco mosaic virus (TMV)**. **(a)** Illustration of the protein structure of TMV. **(b)** Topography of TMV on a silicon substrate. Scale bar is 100 nm. **(c)** Infrared near-field phase images φ at two different frequencies, 1660 cm^{-1} (left) and 1720 cm^{-1} (right) (2.5 min total image acquisition time). **(d)** nano-FTIR absorption spectrum of TMV taken at the position marked by the red dot in the topography image (red, average of 40 interferograms; 22 min total acquisition time; 8 cm^{-1} resolution; x4 zero filling) and GI-FTIR spectrum (blue) and transmission-FTIR spectrum (black) of TMV. The position marked by the yellow dot and R in Fig. 6.1b indicates where the reference spectrum was recorded. **(e)** Schematics of s-SNOM and nano-FTIR. **(f)** Schematics of GI-FTIR spectroscopy. **(g)** Schematics of transmission-FTIR spectroscopy.

In far-field FTIR spectroscopy the exact peak position of the Amide I band is extensively used to learn about the secondary structure of proteins. Therefore, in order to extract nanoscale information about secondary structure of proteins we analyzed how the amide I peak position of the nano-FTIR absorption spectrum compares to that of far-field FTIR spectra. To this end, we recorded far-field FTIR spectra of TMV, by employing p-polarized GI-FTIR and transmission-FTIR spectroscopy (blue and black spectra in Fig. 6.1d, respectively, see chapter 6.2 for details). Schematics of nano-FTIR, GI-FTIR and transmission-FTIR spectroscopy are shown in Fig. 6.1e, f and g, respectively. Fig. 6.1d clearly shows that the peak positions vary significantly depending on the FTIR spectroscopy technique (see also Fig. 6.9). For transmission-FTIR spectroscopy the Amide I peak position is at 1650 cm^{-1}, while for GI-FTIR spectroscopy it is at 1660 cm^{-1} (marked with dashed black and blue lines, respectively,

in Fig. 6.1d). Most importantly, the Amide I peak position of the nano-FTIR absorption spectrum fits to that of GI-FTIR spectroscopy. Thus, our results suggest that in order to extract reliable information (i.e. secondary structure of proteins) nano-FTIR absorption spectra should be compared to GI-FTIR spectra. It is important to note that nano-FTIR phase spectra may be blue-shifted with respect to the nano-FTIR absorption spectra (i.e. imaginary part). Importantly, the spectral shift between nano-FTIR phase and nano-FTIR absorption spectra depends on the size and geometry of the measured nanostructure [85]. Thus, for comparison between near-field (either phase or absorption) and far-field spectra the size and geometry of the measured nanostructure needs to be taken into account, as well as the specific FTIR spectroscopy technique.

6.4.2 Sensitivity of nano-FTIR to a single ferritin complex

In order to show the high sensitivity of the nano-FTIR technique, we studied single ferritin particles, which are globular protein complexes comprising only about 4,000 amino acids (see chapter 6.2 for sample description). The topography image in Fig. 6.2c shows two particles of about 10 nm and 8 nm, and one of about 6 nm height, which appear much broader due to convolution with tip apex that has a radius of about 35 nm (see Fig. 6.2b and Fig. 6.3). The infrared phase image φ at 1660 cm^{-1} reveals a strong absorption for the 10 nm and 8 nm particles, indicating that these are ferritin complexes. No infrared contrast is seen for the 6 nm particle which we interpret as ferrihydrite core that does not absorb at 1660 cm^{-1}. Fig. 6.2d shows the nano-FTIR absorption spectrum (red curve) of the ferritin marked by the red dot in Fig. 6.2c, in comparison with a GI-FTIR spectrum of a large ferritin ensemble (blue curve). As demonstrated with the TMV (*vide supra*), the nano-FTIR absorption spectrum reveals the amide I and II bands in excellent agreement with the GI-FTIR spectrum. Thus, we conclude that nano-FTIR allows for measuring infrared spectra of individual protein complexes, which can be interpreted by comparison with standard GI-FTIR absorbance spectra.

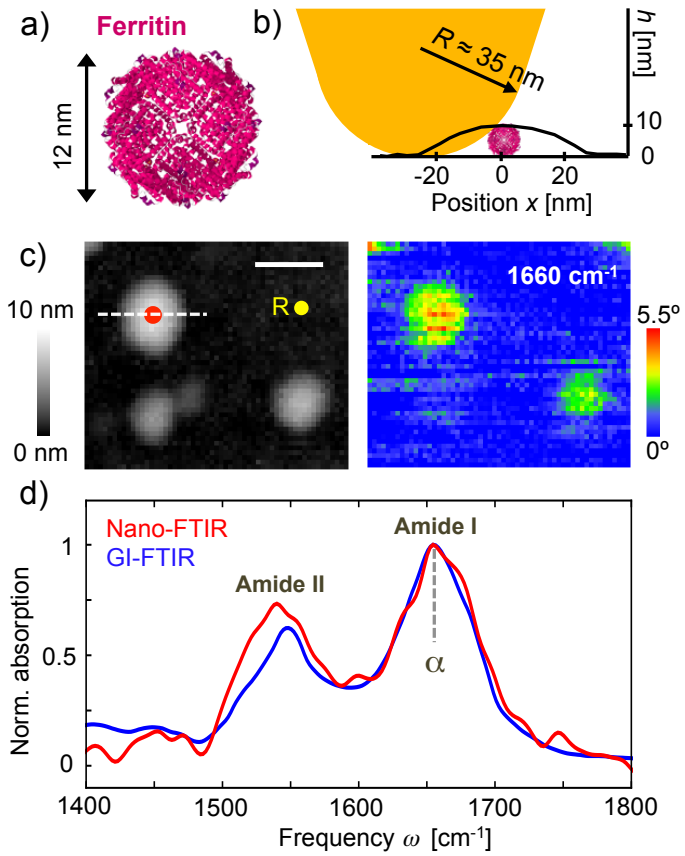

Fig. 6.2: **Infrared nanospectroscopy of individual ferritin protein complexes**. **(a)** Illustration of the protein structure of ferritin. **(b)** Illustration of the tip probing a ferritin particle. The graph shows the measured height profile h when the tip is scanned along the dashed line in Fig. 6.2c. **(c)** Topography and infrared near-field phase image φ of two ferritin molecules and a ferrihydrite core on a silicon substrate. Scale bar is 50 nm (1.5 min total image acquisition time). **(d)** nano-FTIR (red) and GI-FTIR absorption spectra of a large ferritin ensemble on a gold substrate (blue). The red dot in the topography image marks the position where the nano-FTIR absorption spectrum (average of 60 interferograms; 23 min total acquisition time; 8 cm^{-1} resolution; x4 zero filling) was recorded. The position marked by the yellow dot and R in Fig. 6.2c indicates where the reference spectrum was recorded.

In order to show that the marked object (red dot in Fig. 6.2c) is one ferritin complex, we compare in Fig. 6.3 the measured topography profiles with simulated topography profiles. The topography in Fig. 6.3a shows 3 features that could correspond to one, two or more individual ferritin complexes or ferritin cores. Since the spectral signature of ferritin (resulting from the ferritin shell) is only present in features A and B (see right panel in Fig. 6.2c), they can be identified as ferritin complexes, while the feature C could be a ferri-hydrite core. Such assignment is supported by the height of the features. Indeed, the measured height of feature C is within the normal spread for the ferri-hydrite core, which have diameters varying from 5 to 8 nm. In the dry environment, the protein shell might shrink to the core surface. With a protein shell thickness of about 2nm, the resulting variation of the diameter of the ferritin complex might vary from 9 to

12 nm. Allowing for a deformation of the shell due to mechanical interaction with the AFM tip, the measured heights of the features A and B match well the expected diameter of ferritin complexes in dry environment. Since the heights of the topographical features are too low to allow for several ferritin complexes or cores being stuck vertically upon each other, they can only correspond to a lateral arrangement of multiple particles. To elucidate whether each topographical feature corresponds to one or more individual particles, we model the topography profiles for one and two particles and compare them to those taken along the horizontal lines in Fig. 6.3a. In the model, the tip and the particles are represented as hard spheres and the topography is found by searching for the minimum tip height, which produces zero convolution. The particle diameters for the modeling are available from the measured heights of the corresponding topographical features. The tip radius R has to be determined self-consistently as the one producing the best match for the experimental topography profile for all features (thick grey curves in Fig. 6.3b-g). We first calculated the convolution of a tip of radius R with single particles of a diameter corresponding to the feature heights. We found that for a tip radius R=35 nm the calculated height profiles (red curves in Fig. 6.3b-d) nearly perfectly match the measured height profiles (grey curves). The calculated convolution with more than one particle yields pronouncedly flatter height profile with small dips. Both consequences do not match the measured height profiles. For an example, see the simulated height profiles obtained for two particles adjacent to each other as would be measured with a tip radius of R=35 nm (blue lines, panels b-d) and R=25 nm (green lines, panels e-g). This analysis indicates that each of the features A and B represents one ferritin complex, and feature C one core.

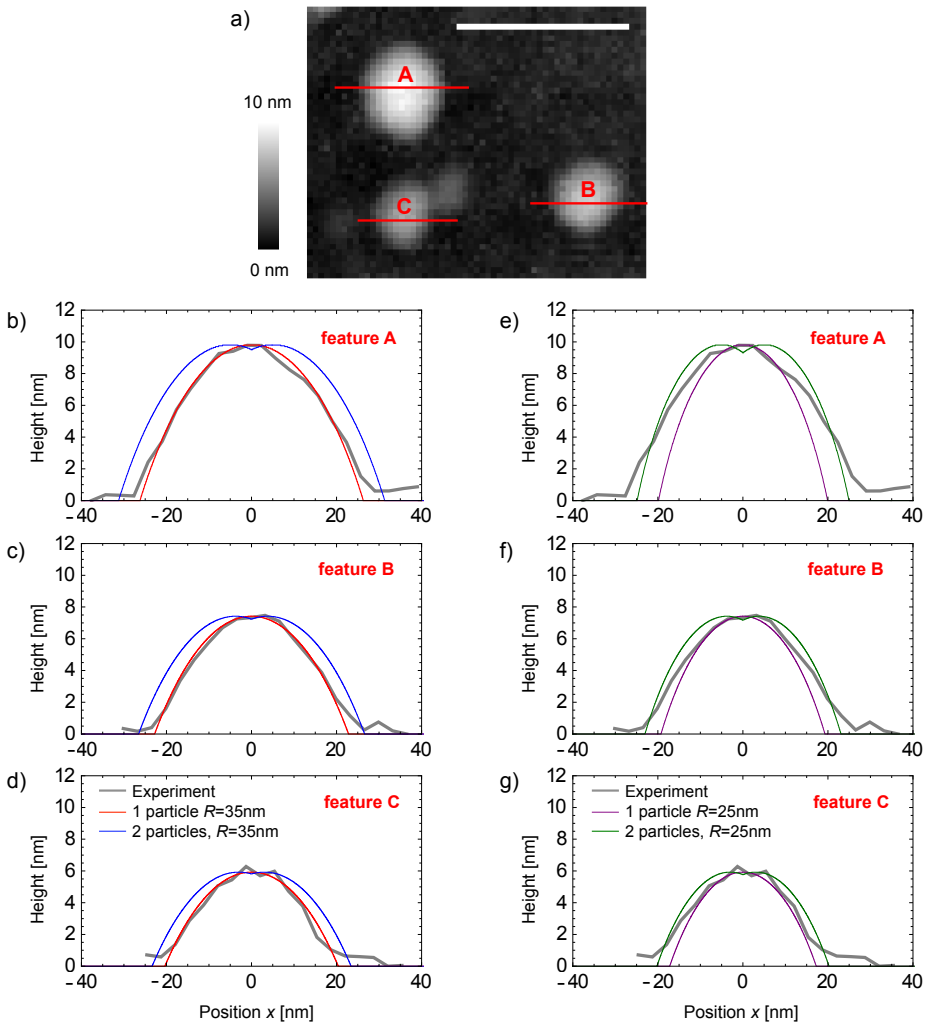

Fig. 6.3: **Measured and simulated topography profiles of particles shown in Fig. 6.2c**. **(a)** The topography as shown in Fig. 6.2c. The scale bar is 100 nm. **(b)** Measured (thick grey) topography profiles for feature A taken along the red line marked in panel (a) and the corresponding simulation (thin red and blue) with tip radius R = 35 nm. Thin red line represents a simulation with one particle. The thin blue line represents a simulation with two particles. **(c)** Same as in panel (b) but for feature B. **(d)** Same as in panel (b) but for feature C. **(e)** Measured (thick grey) topography profiles for feature A taken along the red line marked in panel (a) and the corresponding simulation (thin purple and green) with tip radius R = 25 nm. Thin purple line represents a simulation with one particle. The thin green line represents a simulation with two particles. **(f)** Same as in panel (e) but for feature B. (g) Same as in panel (e) but for feature C.

6.4.3 Influence of protein orientation studied with purple membranes (PMs)

In order to explore whether and how nano-FTIR absorption spectra depend on the protein orientation, we studied the purple membrane (PMs) of *Halobacterium salinarum* (Fig. 6.4), which is composed mainly of transmembrane α-helices. As the helices are predominantly oriented perpendicular to the membrane plane, the infrared amide I vibration (C=O) is normal to the membrane surface, whereas the amide II vibration (N-H) is parallel to the membrane surface [86] (see illustration in Fig. 6.4b). The well-

defined directions of the amide vibrations render PM an excellent protein structure for studying the sensitivity of nano-FTIR to protein orientation. In the topography image (Fig. 6.4a) the membranes appear as 6 nm high flat layers. As before with the TMV, the infrared phase contrast (Fig. 6.4c) at 1660 cm^{-1} exhibits the typical amide I absorption, which vanishes at 1720 cm^{-1} because the archaeobacterial purple membrane is devoid of any ester lipids that usually give rise to carbonyl stretching vibrations in lipid membranes of eubacteria and eukarya. A nano-FTIR absorption spectrum a (Fig. 6.4d, red curve) is obtained by placing the tip atop the PM (marked by red dot in Fig. 6.4a). The GI-FTIR spectrum (p-polarized incident field) of horizontally adsorbed PMs was recorded for comparison (Fig. 6.4d, blue curve). Interestingly, the amide II band does not appear in both spectra. In the GI-FTIR spectroscopy experiment, the electric field is perpendicular to the PM surface and thus perpendicular to the direction of the amide II vibrations. For that reason, amide II vibrations are not excited [86]. The absence of the amide II band in the nano-FTIR absorption spectrum is explained by the field distribution at the tip apex, which essentially is that of a vertically oriented point dipole located in the tip apex (Fig. 6.4b) [44]. The strongest field, located directly below the tip apex, is vertically oriented, and efficiently couples the protein vibrations normal to the PM surface (amide I) but not the protein vibrations parallel to the PM surface (amide II). This orientation-dependent effect is well-known from surface-enhanced infrared absorption spectroscopy [87]. Thus, we conclude that nano-FTIR primarily probes molecular vibrations that oscillate perpendicular to the sample surface.

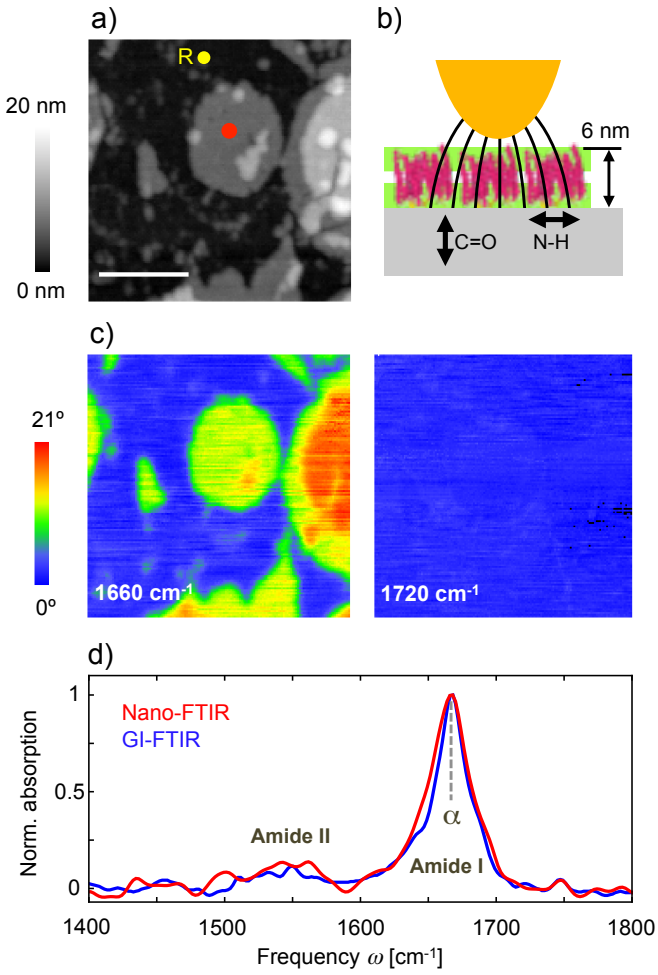

Fig. 6.4: **Nano-FTIR sensitivity to protein orientation demonstrated with purple membrane (PM).** **(a)** Topography of PMs on a silicon substrate. Scale bar is 400 nm. **(b)** Illustration of near-field probing of PM. **(c)** Infrared near field phase images φ at two different frequencies, 1660 cm^{-1} (left) and 1720 cm^{-1} (right) (19 min total image acquisition time). **(d)** nano-FTIR (red) and GI-FTIR absorption spectra of an ensemble of horizontally absorbed PMs on a gold substrate (blue). The red dot in the topography image marks the position where the nano-FTIR absorption spectrum (average of 60 interferograms; 23 min total acquisition time; 8 cm^{-1} resolution; x4 zero filling) was recorded. The position marked by the yellow dot and R indicates where the reference spectrum was recorded. Contrary to all the rest nano-FTIR data shown in this thesis where the demodulation order is three, in the nano-FTIR absorption spectrum shown in (d) the demodulation order is two.

6.4.4 Spatial resolution of nano-FTIR.

In Fig. 6.5 we evaluate the spatial resolution and reproducibility of nano-FTIR protein spectroscopy, by recording 20 spectra while the tip is scanning in steps of 10 nm across the PM. The spectral line scan (Fig. 6.5b) along the line of red dots in the topography image (Fig. 6.5a) reveals the amide I peak on top of the membrane until the edge is reached (at position x~80 nm). Plotting the nano-FTIR absorption a at 1660 cm^{-1} as a function of the position x (Fig. 6.5c), shows that absorption vanishes within three scan

steps. This demonstrates a spatial resolution of about 30 nm, which is an improvement by more than 100 compared to micro-FTIR mapping [88]. We further note that the 8 local infrared spectra on the PM (P1-P8, between $x = 0$ and 80 nm) exhibit a stable peak position and peak height, which illustrates the high reproducibility of nano-FTIR (Fig. 6.5d). On the other hand, this results shows that the infrared absorption of PM does not exhibit significant spatial variations, confirming the homogeneity of the protein structure within the purple membrane.

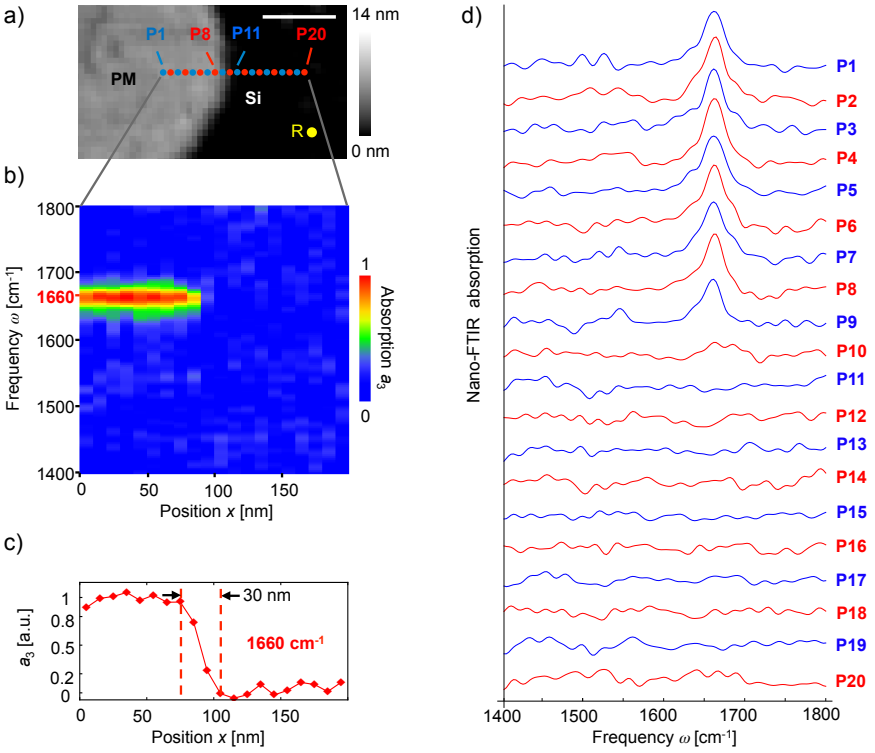

Fig. 6.5: **Spatial resolution and reproducibility of nano-FTIR protein spectroscopy demonstrated with purple membrane (PM).** **(a)** Topography image of PM on a silicon substrate. Scale bar is 100 nm. **(b)** Infrared-spectroscopic line scan recorded while the tip was scanned in 10 nm steps along the line of red and blue dots in Fig. 6.5a. At the position of each dot a spectrum was taken (each spectrum is an average of 17 interferograms; 2.3 min acquisition time; 16 cm^{-1} resolution; x6 zero filling). **(c)** Absorption signal a at 1660 cm^{1} as a function of position x. **(d)** 20 nano-FTIR absorption spectra recorded at the positions P1 to P20 marked by red and blue dots in Fig. 6.5a. The spectra are the same as those presented in Fig. 6.5b. For better visibility each spectrum is vertically offset. All spectra have been normalized to the reference spectrum recorded at the position marked by the yellow dot and R in Fig. 6.5a.

6.5 Nanoscale mapping of structural protein heterogeneity

To establish nanoscale identification of α-helical and β-sheet structure in proteins, and to demonstrate heterogeneity in a sample at the nanometer scale that is only resolvable

by nano-FTIR, we studied insulin aggregates deliberately contaminated with a low amount of TMV (Fig. 6.7). While α-helices dominate in TMV, the insulin aggregates are composed of essentially two β-sheets [81]. The TMV can be thus considered a diluted α-helical structure within a β–sheet sample.

For sample preparation we used a 2 year old insulin solution (see chapter 6.2). Such a solution yields insulin aggregates rather than well-defined fibrils. For such a sample we expect that the orientation of the infrared-active β-sheet dipole of the amide I band is random, thus yielding a signal in nano-FTIR. Note that only vertically oriented dipoles yield a signal in nano-FTIR as shown in chapter 6.4.3. Furthermore, insulin aggregates contain more β-sheet structure than insulin fibrils as can be observed in the CD spectra of different insulin solutions shown in Fig. 6.6. The CD spectrum of the insulin aggregates displays essentially characteristic β-sheet features, while the CD spectrum of the insulin fibrils displays characteristic β-sheet features with slight α-helical features.

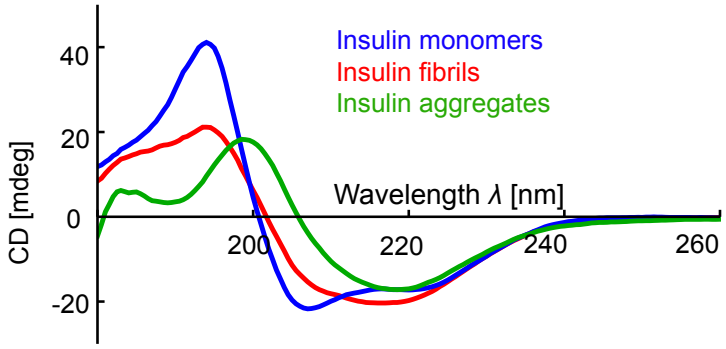

Fig. 6.6: **CD spectrometry analysis of different insulin solutions**. CD spectra of insulin aggregates (green), insulin fibrils (red) and insulin monomers (blue). All CD spectra were recorded with a Jasco J-815 CD spectrometer and a cell with a 1 mm optical pathlength. From each insulin CD spectrum we subtracted the solvent CD spectrum. Each spectrum is the result of averaging 36 scans, recorded at room temperature.

In Fig. 6.7a we show ATR-FTIR spectra of pure insulin aggregates (black curve) and of the insulin/TMV mixture (blue curve). The ATR-FTIR spectrum of the insulin/TMV mixture closely matches to the ATR-FTIR spectrum of pure insulin and does not reveal the presence of TMV. The topographical image (Fig. 6.7b) of the mixture shows rod-like structures and aggregates of up to 32 nm in height. Still, TMV and insulin cannot be clearly discriminated. Fig. 6.7c shows the near-field infrared phase images at 1634 cm^{-1} and 1660 cm^{-1}, corresponding to the center frequencies of the amide I band for β-sheet and α-helical structure, respectively [70]. In both infrared images all structures show a distinct absorption contrast. As expected, the phase contrast to the substrate (i.e. absorption) increases with particle height (i.e. volume). Comparing the two infrared images, we find a significant increase of the phase contrast from 1634 cm^{-1} to 1660 cm^{-1} for the smooth rod in the lower left corner of the image while for all other structures the

phase contrast did not change with respect to the substrate. From this observation we conclude that α-helices form this rod-like structure, which is thus most likely a TMV. For identification of the secondary structure, we recorded nano-FTIR absorption spectra (Fig. 6.7d) on the smooth rod at the position marked by the red dot in the topography image (red spectrum), and on the aggregate marked by the green dot (green spectrum). The red spectrum exhibits the absorption maximum at 1660 cm^{-1}, which corresponds to the amide I resonance frequency of α-helices. Furthermore, the shape fits well to thei nfrared spectrum of TMV (Fig. 6.1d). These results lead us to identify this rod-like structure as a TMV particle. In contrast, the green spectrum significantly differs from the red, exhibiting two peaks at 1660 cm^{-1} and 1634 cm^{-1}, which are attributed to the presence of α-helices and β-sheets, respectively. Thus, we can identify this particle as an insulin aggregate, as its nano-FTIR absorption spectrum agrees with the ATR-FTIR spectrum of the pure insulin sample (Fig. 6.7a, black curve). Note that we compare the nano-FTIR absorption spectrum with an ATR-FTIR spectrum, rather than with GI-FTIR spectrum, as the infrared signal was too weak to obtain a GI-FTIR spectrum. Because ATR-FTIR spectra are typically red-shifted relative to GI-FTIR spectra [4] (see Fig. 6.9), the ATR-FTIR spectrum is slightly red-shifted compared to the nano-FTIR absorption spectrum.

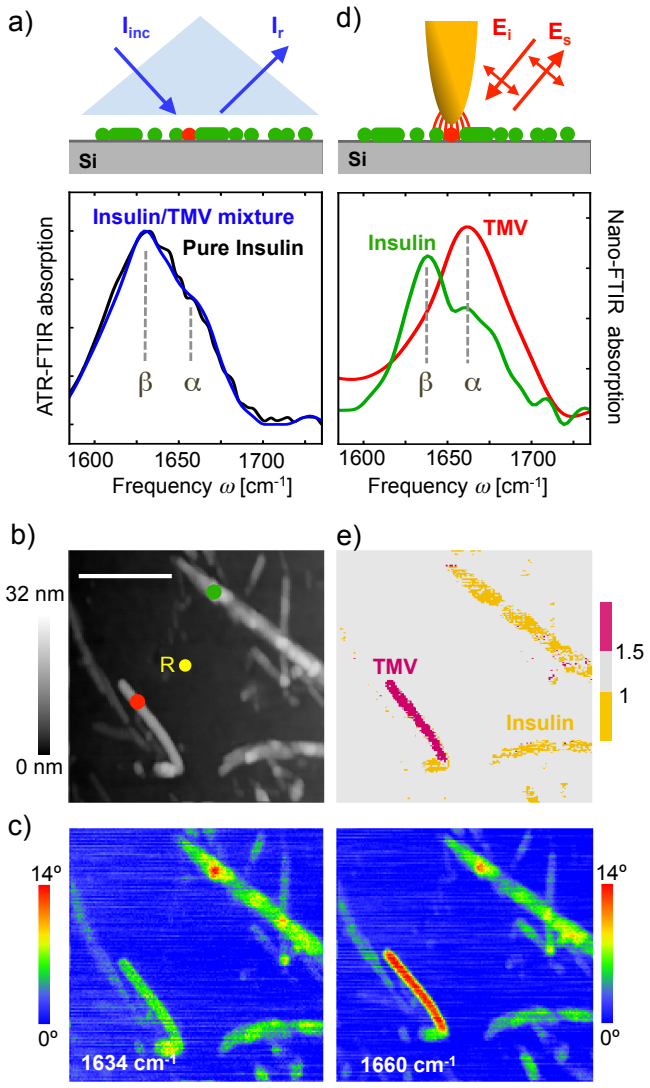

Fig. 6.7: **Nanoscale mapping of α-helical and β-sheet secondary structure**. **(a)** ATR-FTIR spectrum of a pure insulin aggregate sample (black) and a mixture of insulin aggregates and TMV (blue) on a silicon support. **(b)** Topography of a mixture of TMV and insulin aggregates on silicon. Scale bar is 500 nm. **(c)** Infrared near-field images of φ at two different frequencies, 1634 cm^{-1} (left) and 1660 cm^{-1} (right) (19 min total image acquisition time). **(d)** nano-FTIR absorption spectra of TMV (red, average of 70 interferograms; 19 min total acquisition time; 16 cm^{-1} resolution; x4 zero filling) and insulin aggregate (green, average of 40 interferograms; 22 min total acquisition time; 8 cm^{-1} resolution, x4 zero filling). Red and green dots in the topography image mark the positions where the nano-FTIR absorption spectra were taken. The position marked by the yellow dot and R indicates where the reference spectrum was recorded. **(e)** Map of TMV (purple) and insulin (yellow) aggregates.

To visualize the nanoscale distribution of TMV and insulin aggregates, i.e. the nanoscale structural heterogeneity of the sample, we calculated the ratio between the infrared phase images at 1660 cm^{-1} and 1634 cm^{-1}. From the spectra displayed in Fig. 6.7d we know that the absorption of TMV is stronger at 1660 cm^{-1} than at 1634 cm^{-1}. For insulin the absorption is stronger at 1634 cm^{-1}. Every image pixel where we obtain a

ratio that is significantly larger than 1 thus reveals TMV, while every image pixel where we obtain a ratio that is smaller than 1 reveals insulin. Fig. 6.7e shows a map where pixel with ratio larger than 1.5 are depicted in purple, and pixel with ratio smaller than 1 in yellow. The map clearly reveals the TMV (purple) and shows that all other protein structures (yellow) have a strong signal at 1634 cm^{-1}, which can be attributed to the presence of β-sheets. This allows us to identify them as insulin aggregates.

6.6 Nano-FTIR studies of individual insulin fibrils

Having demonstrated the capability of mapping secondary structure on the nanometer scale, nano-FTIR is well prepared for applications in biochemical and biomedical research. We explore - as a first application example - the protein conformation in individual insulin fibrils (Fig. 6.8). Insulin can form amyloid-like fibrils and fibers composed of filament-shaped protein aggregates [70], [81], [84], which renders it an excellent and widely used model system for neurodegenerative disease research (i.e. Alzheimer, Parkinson). Studies [81], [89] show that the filaments have a core composed of β-sheets (Fig. 6.8a). It is assumed that this core is surrounded by randomly oriented secondary structures, including α-helices, β-turns and unordered structures [70]. However, the exact structure of the shell is still an open question of high biological relevance [84]. Recent studies by tip-enhanced Raman spectroscopy (TERS) indicate the presence of α-helices/unordered structures at the surface of the fibrils [90], [91]. In the following we apply nano-FTIR and s-SNOM to study the protein conformation in insulin fibrils.

In contrast to insulin aggregates shown in chapter 6.5, insulin fibrils were grown by incubating insulin protein at 60°C in a pH 2 buffer for 30 hours (see more details in chapter 6.2), thus representing a biologically relevant model system. In Fig. 6.8b the topography of a sample area is shown where we found type I (3 nm high, consisting of two protofilaments, marked I) and thicker insulin fibrils (with increasing thickness the number of protofilaments increases) with heights ranging from 5 to 10 nm [70], [92], [93]. In the nano-FTIR absorption spectrum of a 9 nm thick fibril (Fig. 6.8c, red curve, taken at the position marked by the red dot in the topographical image) we find the strongest peak at 1669 cm^{-1}. By comparison with a GI-FTIR spectrum of monomeric insulin (predominantly α-helical structure, blue dashed curve) we can assign this peak to the presence of α-helical structure. The peak at 1638 cm^{-1} is assigned to β-sheets. However, it is relatively weak compared to the nano-FTIR absorption spectrum of the insulin aggregates (Fig. 6.7d). We explain this observation by the well-aligned β-sheet structure forming the core of the fibrils seen in Fig. 6.8a, where the dipole orientation of the amide I band is mostly parallel to the filament axes (i.e. to the substrate surface) [94], [95]. As seen before in chapter 6.4.3 with purple membrane, protein vibrations parallel to the substrate couple only weakly to the near field at the tip apex and thus are suppressed in the nano-FTIR absorption spectra.

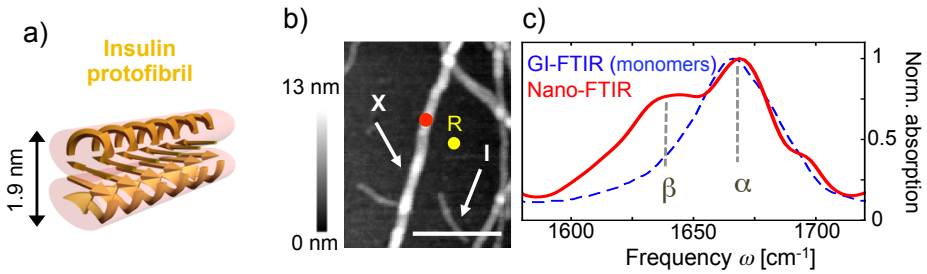

Fig. 6.8: **Nano-FTIR of individual insulin fibrils**. **(a)** Illustration of the structure of an amyloid-like insulin protofibril (a type I fibril consists of two protofibrils). **(b)** Topography of insulin fibrils on a silicon substrate. Scale bar, 300 nm. The arrows indicate a type I fibril (I) and a 9 nm thick fibril composed of several protofilaments (X), respectively. **(c)** nano-FTIR absorption spectrum of a 9 nm thick insulin fibril (red, average of 154 interferograms; 8 cm^{-1} resolution; x4 zero filling) recorded at the position marked by the red dot in Fig. 6.8b. The position marked by the yellow dot and R indicates where the reference spectrum was recorded. The dashed blue line shows for comparison a GI-FTIR spectrum of insulin monomers on a gold substrate.

Amide I peak position of α-helical secondary structure

The Amide I peak frequency of 1666 cm^{-1} recorded by GI-FTIR spectroscopy for the α-helical insulin momomers (see red graph in Fig. 6.8c) seems to be unusual high. However, it can be readily explained by the FTIR experimental modality. It is well known that GI-FTIR spectra can be significantly blue shifted compared to standard transmission-FTIR spectra [4] (see Fig. 6.1). We demonstrate this phenomenon in Fig. 6.9, where we compare FTIR spectra of the insulin monomer sample obtained by different standard techniques (see chapter 6.3). The peak in the transmission-FTIR spectrum occurs at the much lower frequency 1656 cm^{-1}, which matches literature data (ranging from 1654 to 1658 cm^{-1} [96]–[98])

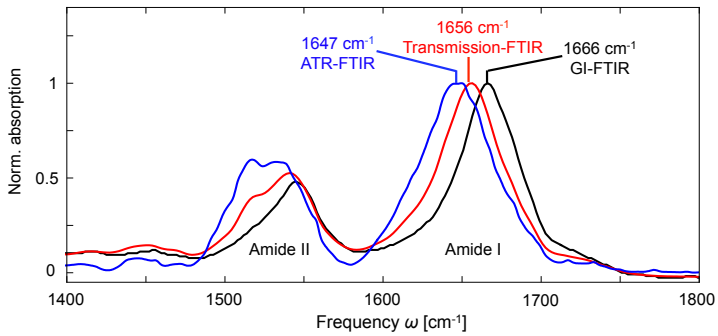

Fig. 6.9: **Comparison of standard far-field FTIR spectra of insulin monomers**. Attenuated total reflectance FTIR (ATR-FTIR) spectrum (blue), standard transmission-FTIR spectrum (red), and p-polarized grazing incidence FTIR (GI-FTIR) spectrum (black).

Standard band decomposition

To obtain more details about the secondary structure of the fibrils and to show that standard FITR analysis tools can be used to analyze nano-FTIR absorption spectra, we performed standard band decomposition of the nano-FTIR absorption spectrum of the 9 nm thick insulin fibrils shown in Fig. 6.8c. The band decomposition was performed with the OPUS software package (version 4.2) supplied by Bruker. As a starting point for the curve fitting procedure, five individual absorption bands were proposed at 1638, 1655, 1667, 1685 and 1705 cm^{-1}, defining parallel β-sheets, unordered, α-helices, β–turn and antiparallel β-sheet structures, respectively. The curve fitting was successfully performed based on the damped least-squares optimization algorithm developed by Levenberg–Marquardt and assuming Gaussian band envelopes. The obtained residual RMS error was 0.0048.

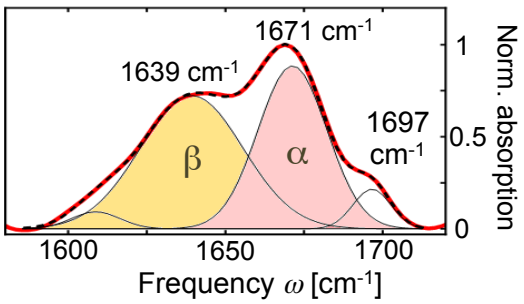

Fig. 6.10: **Band decomposition of nano-FTIR absorption spectra**. Band decomposition of the nano-FTIR absorption spectrum (red curve) based on five absorption bands (thin black curves). The dashed black curve shows the resulting fit.

Comparing the decomposed nano-FTIR absorption spectrum of the insulin fibrils with a GI-FTIR spectrum of insulin monomers (peak maximum at 1666 cm^{-1}), we can assign the peak at 1671 cm^{-1} to α-helical structure. The insulin monomers are dominantly α-helical structure, as we confirmed by CD measurements shown in Fig. 6.6. The frequency difference between 1666 and 1671 cm^{-1} might be caused by the structural change from monomer to fibril structure, or due to the different sample support, which in nano-FTIR is silicon and in GI-FTIR spectroscopy is gold. The band decomposition also revealed another major band at 1639 cm^{-1} confirming that β-sheet structures also contribute predominantly. The band at 1697 cm^{-1} could be caused by β-turns or even antiparallel β-sheet structure and the weak band at 1609 cm^{-1} might indicate side chains. Most importantly, no band is observed in between the β- and α-peaks, where typically unordered structure is located [69]. Thus, we conclude that disordered structures are almost absent in the fibrils. Note that the dipole of the amide I band is isotropically oriented in disordered structures and thus orientation cannot be the cause for this observation.

6.6.1 s-SNOM based spectroscopic analysis of type I insulin fibrils

To explore the presence of α-helices in type I insulin fibrils (which are only 3 nm thick), we performed infrared s-SNOM imaging at different frequencies provided by our QCL. For nano-FTIR of such thin fibrils the broadband laser source does not yet provide enough infrared power. Fig. 6.11a shows infrared near-field phase images at four different wavelengths, exhibiting clear contrast for both the type I and the 9 nm thick fibrils. From altogether 12 images we extracted local infrared spectra at the positions marked by the red, green and blue symbols in Fig. 6.11a. The spectra are plotted in Fig. 6.11b using the corresponding symbols. For both the 9 nm thick fibril (red and green symbols) and type I (blue symbols) fibril we find the same spectral signature as observed in the nano-FTIR absorption spectrum (thick red curve in Fig. 6.11b).

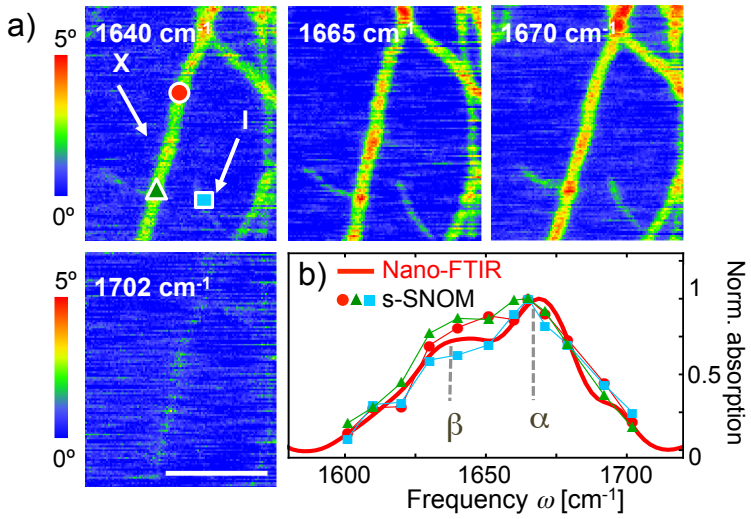

Fig. 6.11: **Nanoimaging based spectroscopic analysis of type I insulin fibrils**. **(a)** s-SNOM phase images of the fibrils shown in Fig. 6.8b. Scale bar is 300 nm. **(b)** Local infrared absorption spectra (symbols) depicting the normalized imaginary part of the near-field signal at the positions marked in Fig. 6.11a. The data points were extracted from twelve near-field amplitude and phase images and were normalized to the imaginary part of the near-field signal on the silicon substrate. Four of the phase images are shown in Fig. 6.11a. For comparison the nano-FTIR absorption spectrum of Fig. 6.8c is depicted by the red thick curve. All spectra are normalized to their maximum value.

The spectrum acquired at the position marked by the blue symbol in Fig. 6.11a thus provides experimental evidence that α-helices are also present in type I fibrils. The current resolution of about 30 nm does not allow for concluding whether the α-helices are inside the core or forming a shell. Assuming that the core is formed of purely β-sheets (according to current models [89]), our findings suggest that the shell is highly

structured (mainly α-helical structure) and not randomly organized. The presence of α-helices in the shell could explain the tendency of fibrils to associate.

6.7 Conclusions.

Nano-FTIR enables reliable probing and mapping of protein secondary structure with nanoscale resolution, and close to single protein sensitivity. Our results indicate that infrared spectra of one ferritin complex can be obtained, which demonstrates extraordinary sensitivity of nano-FTIR to ultra-small amounts of material, in case of one ferritin complex $0.8\ 10^{-18}$ g (about 1 atto-gram) of protein, respectively 5000 C=O bonds. By further sharpening the tips and optimizing their antenna performance [99], we envision single protein spectroscopy in the future, paving the way to a new era in infrared bio-spectroscopy. Most importantly, we find that the amide I band in the nano-FTIR spectra can be analyzed and interpreted in the framework of standard infrared spectroscopy. We foresee manifold applications, such as studies of conformational changes in amyloid structures on the molecular level, the mapping of nanoscale protein modifications in biomedical tissue or the label-free mapping of membrane proteins. In order to operate under physiological conditions, for example to study the membrane of living cells, s-SNOM and nano-FTIR have to operate in liquids. Indeed, scanning near-field optical microscopy in liquids and under physiological conditions has been already demonstrated [100], [101]. In order to perform nano-FTIR, the water could be exchanged by D_2O, which is typically done in conventional FTIR spectroscopy in order to eliminate infrared absorption by H_2O in the region of the amide I band [96].

7 Hyperspectral infrared nanoimaging based on nano-FTIR using a laser continuum

In this chapter we introduce hyperspectral infrared nanoimaging, that is, the recording of a two-dimensional array of nano-FTIR spectra, using a tunable bandwidth-limited laser continuum. We describe the key technical innovations that for the first time have allowed for hyperspectral infrared nanoimaging based on nano-FTIR; increase of data acquisition speed, sample drift correction or stitching of bandwidth-limited nano-FTIR spectra. We show that using a tunable DFG laser continuum with an effective spectral bandwidth of about 400 cm^{-1}, hyperspectral data cubes of about 5000 nano-FTIR spectra covering 1000 to 1900 cm^{-1} could be recorded in less than 8 hours.

7.1 Introduction

In chapter 6 we demonstrated that nanoscale imaging (s-SNOM; images at fixed wavelength) and nanoscale spectroscopy (nano-FTIR; spectra at individual points) is possible. However, to get further insights into the structure of a sample, spectroscopic information at each pixel of an image is desirable. Spatially-resolved spectroscopic information can be obtained by sequential s-SNOM imaging of one and the same sample area at different infrared frequencies using a tunable monochromatic laser. From the stack of images, an infrared spectrum can be constructed at each pixel [74], [102]–[107]. Typically, tunable monochromatic CO_2 or cw-quantum cascade lasers (QCLs) are used as infrared source. As they can be tuned only over a relatively small spectral width of about 200 cm^{-1}, several lasers are required to cover the whole mid-infrared spectral range. On the other hand, frequencies below 900 cm^{-1} are barely reached with table-top cw-lasers. Further, due to the nonlinear and typically uncontrolled drift between sample scanner and tip, as well as the tip wear due to the numerously repeated sample scanning, the construction of accurate local broadband infrared spectra is challenging.

Spectroscopic infrared nanoimaging, in principle, can be also achieved by recording a nano-FTIR spectrum at each pixel of a 2D image. Advantages would include the availability of continuous broadband radiation also below 900 cm^{-1} (provided by thermal sources [43], [108], synchrotrons [109]–[111] and infrared laser continua [57], [58], [112]–[115]), and that repetitive scanning and related problems (tip wear) could be avoided. However, the low spectral irradiance of many broadband infrared sources is strongly challenging nano-FTIR based hyperspectral infrared nanoimaging, that is, the recording of a large two-dimensional array of nano-FTIR spectra. For example, synchrotrons provide ultra-broadband infrared radiation with a spectral irradiance of about 0.2 $W/cm^2/cm^{-1}$ [109] at mid-infrared frequencies, which is several orders of magnitude weaker than that of mid-IR QCLs used for s-SNOM imaging. The reported time for recording nano-FTIR spectra of materials with a strong infrared response (for example phonons in SiO_2) amounts to about one minute [109], which is significantly increased for weakly absorbing organic substances. The recoding of a hyperspectral

image of about 100x100 = 10000 pixel would require many tens of hours, thus challenging the mechanical and optical stability of nano-FTIR setups. Alternatively to synchrotrons, mid-infrared laser continua based on difference frequency generation (DFG) can be applied for nano-FTIR [57], [58], [112]–[115]. These table top lasers provide tunable infrared radiation of several 100 cm^{-1} bandwidth and a spectral irradiance that can be much higher compared to synchrotrons. However, hyperspectral infrared nanoimaging with such lasers has not been achieved yet. Reasons include the non-negligible sample drift during spectra acquisition, as well as the still relatively small spectral bandwidth that requires the combining of multiple bandwidth-limited nano-FTIR spectra at each pixel.

In this chapter we introduce hyperspectral infrared nanoimaging by nano-FTIR with a tunable laser continuum, and describe the key implementations of the technique. It is based on recording and stitching together multiple bandwidth-limited nano-FTIR spectra at each pixel of a two-dimensional sample area, which is enabled by sample drift correction during spectra acquisition. Specifically, we use a tunable DFG laser continuum (about 400 cm^{-1} effective bandwidth) to record nanoscale-resolved hyperspectral infrared images comprising about 5000 nano-FTIR spectra that cover a spectral range from 1000 to 1900 cm^{-1}.

7.2 Hyperspectral infrared nanoimaging setup

We developed hyperspectral infrared nanoimaging (Fig. 7.1) using the commercial nano-FTIR setup (Neaspec GmbH) described in chapter 5.2. The tip was illuminated with a DFG mid-infrared laser continuum of about 400 cm^{-1} spectral bandwidth, which centre frequency is tunable between 1000 and 1700 cm^{-1} (see Fig. 7.1a).

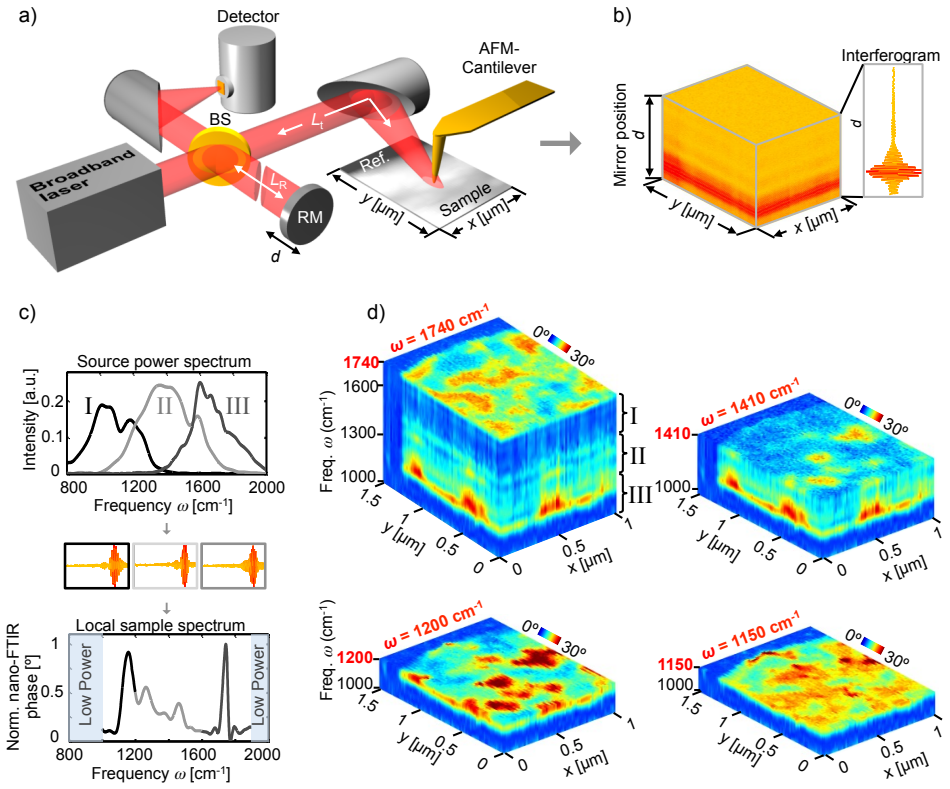

Fig. 7.1: **Hyperspectral infrared nanoimaging**. **(a)** Set-up employing a mid-infrared laser continuum source for tip illumination. The tip scans the sample surface while at each pixel the light backscattered from the tip is analyzed with a Michelson interferometer that is operated as a Fourier transform spectrometer. The setup comprises a beam splitter (BS, uncoated ZnSe), a reference mirror (RM) and a detector. **(b)** Two dimensional array of interferograms. **(c)** Top: Output spectra of the source. Middle: Interferograms recorded for each output spectrum. Bottom: Broadband nano-FTIR phase spectrum composed by three nano-FTIR phase spectra obtained by FT of the corresponding interferograms and normalization to a reference spectrum. **(d)** Hyperspectral infrared data cubes of spectral resolution of 35 cm^{-1}, cut at different frequencies ω. They show the phase of the tip-scattered light as a function of position (x,y) and frequency ω.

For hyperspectral nanoimaging we record interferograms at each pixel (x, y) of a 2D area of the sample surface (Fig. 7.1b). Subsequent Fourier transform and normalization to reference spectra yields a 2D array of nano-FTIR spectra with a spectral bandwidth determined by the output spectrum of the DFG laser source, that is, a hyperspectral data cube $A(x, y, \omega)$ where x and y represent two spatial dimensions and ω the frequency (spectral dimension). For chapters 7 and 8, we recorded and studied nano-FTIR phase spectra $\varphi(\omega)$, as they are related to the sample's infrared absorption [59], [85] (see chapter 5.8), the later being typically analyzed when infrared spectroscopy of organic materials is performed. To increase the spectral bandwidth, we record data cubes $A^k = \varphi^k(x, y, \omega)$ at three different DFG output spectra (indicated by the index k = I,II,III and shown in the upper panel of Fig. 7.1c) and stitch together at each pixel the corresponding normalized nano-FTIR phase spectra (Fig. 7.1c, lower panel). As a

result, a hyperspectral data cube A is obtained. In Fig. 7.1d we show the hyperspectral infrared data cube of a three-component polymer blend on a silicon substrate, which is based on a fluorine copolymer (referred as to FP), an acrylic copolymer (AC), and a polystyrene latex (PS) (see chapter 8.2.1 for details about the sample). Cutting the cube at different infrared frequencies ω yields monochromatic infrared images with a spatial resolution of about 30 nm. They clearly reveal a rich variety of spectrally and spatially varying features, indicating that neither individual point spectra nor individual monochromatic images provide the full information content contained in the hyperspectral data of this sample. We note that for the processing of the hyperspectral data shown in this thesis, the software *MATLAB R2014a* was used. In the following we describe the key implementations of our technique

7.3 Increase of nano-FTIR data acquisition speed

Increase of nano-FTIR data acquisition speed was accomplished through improvement of the SNR of the individual nano-FTIR spectra. To that end, the output power of our mid-IR supercontiuum (described in chapter 4.4 and used in chapter 6) was optimized, yielding about 0.6 mW stable mid-IR radiation over a spectral bandwidth of about 400 cm^{-1}. Moreover, for increasing both the nanofocus intensity and the light collection efficiency, we implemented an off-axis parabolic mirror with increased numerical aperture (NA = 0.4).

Further we optimized the settings for the recording of interferograms in our specific setup. In far-field FTIR spectroscopy a symmetric Michelson interferometer is used, which yields interferograms that are symmetric in respect to the white light position (WLP, corresponding to the position of the reference mirror at which the optical path lengths of both interferometer arms are equal). In contrast, nano-FTIR uses an asymmetric Michelson interferometer, where the sample (together with the tip) is located in one of the interferometer arms. For causality reasons, the interferograms obtained from the sample are asymmetric [116], [117] and only one half of the interferogram contains information about the sample (see demonstration below in Fig. 7.2). Thus, for hyperspectral imaging only the left side of the interferogram was recorded (see middle panel of Fig. 7.1b), and an asymmetric apodization function was applied.

With our improved laser source we succeeded to obtain about 400 cm^{-1} broad nano-FTIR spectra of organic materials in 1.66 seconds, which is more than one order of magnitude faster than what has been previously achieved with DFG and synchrotron radiation [57], [109], [112].

Asymmetric near-field interferogram analysis

In Fig. 7.2 we demonstrate that when a near-field interferogram is recorded in an absorbing sample only one half of the interferogram contains information about the

sample. To this end, we recorded interferograms of a thin Poly(methyl methacrylate) (PMMA) film on silicon (red line in Fig. 7.2a) and of the clean silicon substrate next to it (black line in Fig. 7.2a). The experiment is sketched in Fig. 7.2c. We observe that both interferograms show strong signal oscillations even far away from the WLP. They can be explained by the spectrally sharp mid-infrared absorption of vapor water. Due to the presence of the water vapor in both interferometer arms, the signal oscillations are symmetric to the WLP. Further, they are the same for both the PMMA and the reference sample. Both findings confirm that they do not contain specific information about the PMMA sample. On the other hand, on the left side of the WLP we observe significant differences (marked by orange circle in Fig. 7.2a) between the PMMA and the reference (Si) interferogram. They are caused by the free-induction decay (FID) of the molecular vibrations in the PMMA sample [116].

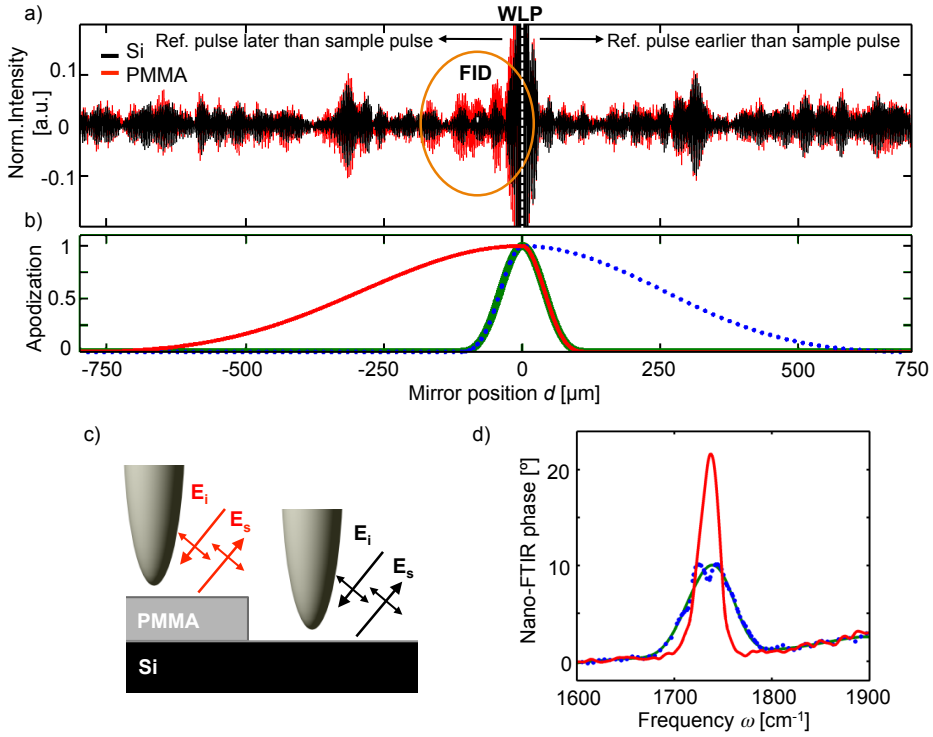

Fig. 7.2: **Asymmetric interferogram analysis**. **(a)** Interferograms of a Poly(methyl methacrylate) (PMMA) film and silicon substrate normalized to the interferogram values at the white light position (WLP). **(b)** Different apodization functions yielding the nano-FTIR phase spectra shown in (d). **(c)** Sketch of the experiment yielding the interferograms shown in (a). **(d)** Nano-FTIR phase spectra obtained from interferograms shown in (a) by using the apodization functions shown in (b).

By FT of the two interferograms shown in Fig. 7.2a, and subsequent normalization of the PMMA spectrum to the Si spectrum, we obtain the nano-FTIR absorption spectra of PMMA. In order to analyze the information encoded at the two sides of the WLP, we applied different asymmetric apodization windows ("*blackman harris 3 term*"[118])

prior to FT, which are shown in Fig. 7.2b (solid red and dotted blue curves). For comparison, we also applied a narrow symmetric apodization window (green solid curve in Fig. 7.2b). The obtained nano-FTIR phase spectra are shown in Fig. 7.2d

The green nano-FTIR phase spectrum clearly reveals the absorption peak of the C=O vibration at 1740 cm^{-1} [57]. The peak is rather broad due to the low spectral resolution owing to the narrow apodization window. The same spectrum (solid red curve in Fig. 7.2d) is obtained when the width of the apodization function is increased on the right side of the WLP (blue dotted graph in Fig. 7.2b). In other words, the spectral resolution is not improved, which can be explained by the absence of a FID at the right side of the interferogram of PMMA. However, increasing the width of the apodization function on the left side of the WLP (red function in Fig. 7.2b) yields an improved spectral resolution, as can be seen by narrowing of the absorption peak in the red spectrum compared to the blue dotted spectrum (Fig. 7.2d). The increasing spectral resolution also comes along with an increase of the height of the red peak compared to the green peak, which is an intrinsic feature of Fourier transform spectroscopy [4].

Our analysis clearly shows that recording of the right part of the interferogram (typically done in standard FTIR spectroscopy) does not provide any spectral information and thus can be skipped in nano-FTIR. We also point out that the spectral resolution of the nano-FTIR spectra is determined by the length of the interferogram on the left side of the WLP, i.e. the side of the interferogram that contains the FID.

7.4 Sample drift correction

Depending on the number of individual spectra, the acquisition of a data cube A^k may still take several minutes to few hours. To avoid artifacts due to sample drift, we adapted concepts known from other imaging techniques (e.g. electron energy loss spectroscopy mapping or AFM [119]). In the nano-FTIR setup used in this thesis the AFM tip is fixed (it only oscillates vertically), while the sample is scanned. To this end, the sample is placed on a linearized scanner with 100 by 100 μm lateral scan range and capacitive position sensors. The methodology for the sample drift correction is described in the following.

First, a topography image of the area of interest is taken (see Fig. 7.3a) and the centre of the hyperspectral image to be recorded is defined and marked as $\overrightarrow{C_0} = (0,0)$ in the scanner software. Further, with the help of the mechanical phase image (see Fig. 7.3b) a small topographical feature (about 40 nm in lateral diameter and 10 nm in height) inside the area of interest is selected as a reference point, R. A small topography image of 150 by 150 nm is recorded in about 5 seconds (see Fig. 7.3c) and the position of the selected reference point in the coordinate system of the scanner is measured, $\overrightarrow{R_0}$. Then, the first *n* spectroscopic line scans of the data cube are recorded. After a time of about 4-5 minutes we interrupt the data acquisition and record again the small topography image and the position of the reference point is measured, $\overrightarrow{R_1}$. The difference between the old and new position of the reference point yields the sample drift that occurred during the line

scans, $\overrightarrow{D_1} = \overrightarrow{R_1} - \overrightarrow{R_0}$. Accordingly, we update in the scanner software the centre coordinates of the image, $\overrightarrow{C_1} = \overrightarrow{C_0} + \overrightarrow{D_1}$, and continue with the data cube acquisition. This procedure is repeated until the whole data cube is recorded; at the n-th repetition we measure the sample drift, $\overrightarrow{D_n} = \overrightarrow{R_n} - \overrightarrow{R_{n-1}}$, and update the centre coordinates to $\overrightarrow{C_n} = \overrightarrow{C_{n-1}} + \overrightarrow{D_n}$.

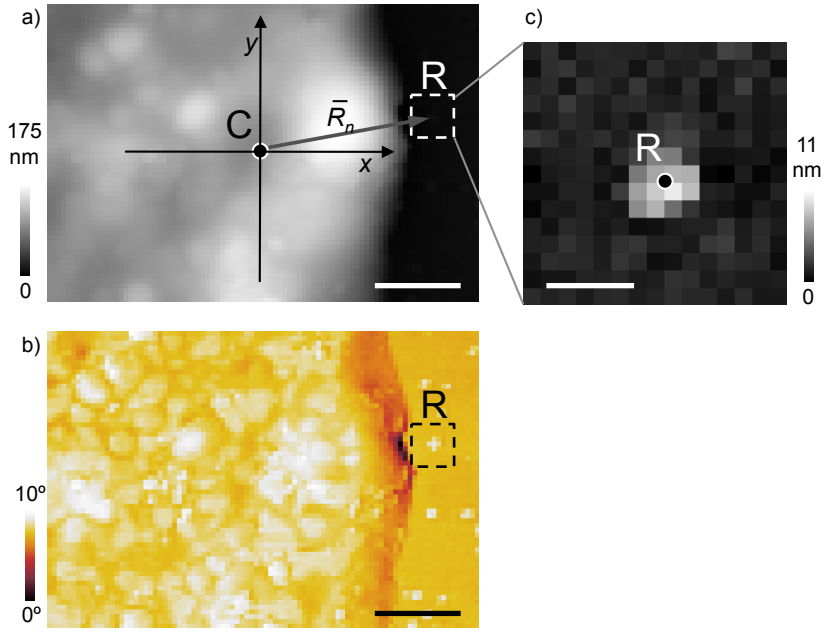

Fig. 7.3: **Sample drift correction**. **(a)** Topography image and **(b)** mechanical AFM phase image of the area of interest in the polymer blend sample shown in Fig. 7.1. Scale bars, 300 nm. **(c)** Zoom in image of the reference point. Scale bar, 50 nm.

The new position of the sample can be set by the scanner software in discreet steps of 10 nm, that is, with an error of about 5 nm. The repeatability of the physical positioning is of about 2 nm, which is determined by the capacitive sensor of the commercial linearized scanner. Thus the maximum error of the re-positioning is of about 7 nm. In all recorded data cubes, the average sample drift $\overrightarrow{D_{AVG}}$ was less than 27 nm per 4 minutes, which is smaller than the spatial resolution of about 30 nm [57], [112]. For that reason, our method allows for the recording of nearly drift-free data cubes. Among others, this achievement is essential for reliable spectral stitching of different data cubes of one and the same area.

For the polymer sample shown in Fig. 7.1d and Fig. 7.3, the repositioning procedure was performed every 2 lines (i.e. every 4-5 minutes), that is, 30 times during the recording of the complete data cube of 82x62 spectra. The recording of the small topography image plus the calculation and repositioning to the updated centre coordinates took about 20 seconds, which yields an accumulated time of about 10

minutes. Thus, the recording of one bandwidth-limited data cube A^k took (5084 x 1.66 s) / 3600 + 10min/60 = 2.5 h and the recording of the hyperspectral data cube A (i.e. three bandwidth-limited data cubes) shown in Fig. 7.1d required about 7.5 hours.

7.5 Normalization of nano-FTIR spectra

For accurate and reliable normalization of the nano-FTIR spectra, the reference spectra need to be recorded under the same experimental conditions. Due to slight spectral fluctuations of the laser continuum and drift of the interferometer arms (see chapter 7.6), however, the conditions may vary between sample and reference measurements. For that reason, we regularly acquire interferograms of a reference area while recording the data cube. This can be achieved, for example, by recording the data cube such that each line contains a clean reference area (e.g. silicon, marked Ref. in Fig. 7.1 where the line scans are parallel to the y-axis). The near-field spectra, of each line are then normalized to the reference spectrum included in this line in order to obtain nano-FTIR spectra.

However, depending on the sample the data cube may not contain any reference spectra due to the lack of an appropriate reference surface. This was the case in the hair cross-section that will be shown in chapter 8.3. For that reason, a small piece (about 2 mm in diameter) of a clean silicon wafer was placed about 300 µm next to the hair cross-section in order to record reference spectra. As described in chapter 7.4 we performed sample drift correction every 4 lines with the help of a reference feature R on the hair sample. After 20 lines, yielding the partial data cube $\varphi_{sam}^{k,1}(x,y,\omega)$, we stopped the data acquisition at the sample position (x_1,y_1) relative to R, in order to record a reference spectrum (note that the recording of 20 lines (40 pixels/line) required a time of about 22 minutes, in which the DFG laser output spectrum did not exhibit noticeable fluctuations). To that end, we moved the center of the silicon surface below the tip (about 10 seconds) and recorded an about 200 x 200 nm size topography image, in order to assure that the surface was clean (about 20 seconds). Subsequently, we recorded the reference near-field phase spectrum $\varphi_{\mathrm{Si}}^{k,1}(\omega)$ (average over several individual reference spectra with a total acquisition time of 30 seconds). We then moved the sample position (x_1,y_1) below the tip, which took about 3 minutes. To that end, we first moved the hair cross-section roughly below the tip by using the optical image of sample and cantilever, which was obtained with the optical microscope that is integrated in the NeaSNOM. By recording a topography image of the hair sample, we identified the reference feature R, which allows for moving the sample position (x_1,y_1) exactly below the tip. We then continued the data cube acquisition for another 20 lines, followed by an interruption for recording the next reference near-field spectrum, yielding $\varphi_{sam}^{k,2}(x,y,\omega)$ and $\varphi_{\mathrm{Si}}^{k,2}(\omega)$, respectively. This procedure was repeated 5 times until the complete data cube was recorded. In order to obtain nano-FTIR phase spectra, the near-field spectra of each partial data cube were normalized to the corresponding reference near-field spectrum according to $\varphi^{k,j}(x,y,\omega) = \varphi_{sam}^{k,j}(x,y,\omega) - \varphi_{\mathrm{Si}}^{k,j}(\omega)$. The recording of each reference spectrum, including the related sample repositioning, process took about 4 minutes,

which resulted in an accumulated extra time of about 20 minutes for the whole data cube.

7.6 Stitching of bandwidth-limited nano-FTIR spectra.

To combine the individual bandwidth-limited data cubes A^k , we need to combine at each position (*x*,*y*) the individual nano-FTIR phase spectra $\varphi^k(x, y, \omega)$ obtained with the different DFG settings. A key for achieving this task is the sample drift correction during the recording of each bandwidth-limited data cube. As outlined in chapter 7.4, the sample drift correction ensures that the position uncertainty is less than the spatial resolution, thus ensuring that spectra of the same position (*x*,*y*) are combined.

The remaining challenges and solutions for combining the individual spectra are shown in Fig. 7.4. We recorded sample-drift-corrected data cubes of the same sample area using the three different laser outputs shown in Fig. 7.4b (numerated k = I, II, III). In Fig. 7.4a (bottom) we show the bandwidth-limited nano-FTIR phase spectra $\varphi^k(x, y, \omega)$ of six subsequent pixels on the polymer blend sample. For better comparison, and to demonstrate the reproducibility of the individual spectra, the upper panel of Fig. 7.4a displays all spectra plotted on top of each other. Within the overlapping spectral regions (marked by grey areas) we clearly observe the same spectral features in the adjacent bandwidth-limited nano-FTIR phase spectra. However, the spectra can be significantly offset against each other by up to 12 degrees, although all spectra are normalized to a reference spectrum (see chapter 7.6). In the following we will first describe the procedure we applied to correct for the fluctuations of the offset $\Delta\varphi$ between the phase spectra of adjacent data cubes, and then we will discuss the origin of such fluctuation.

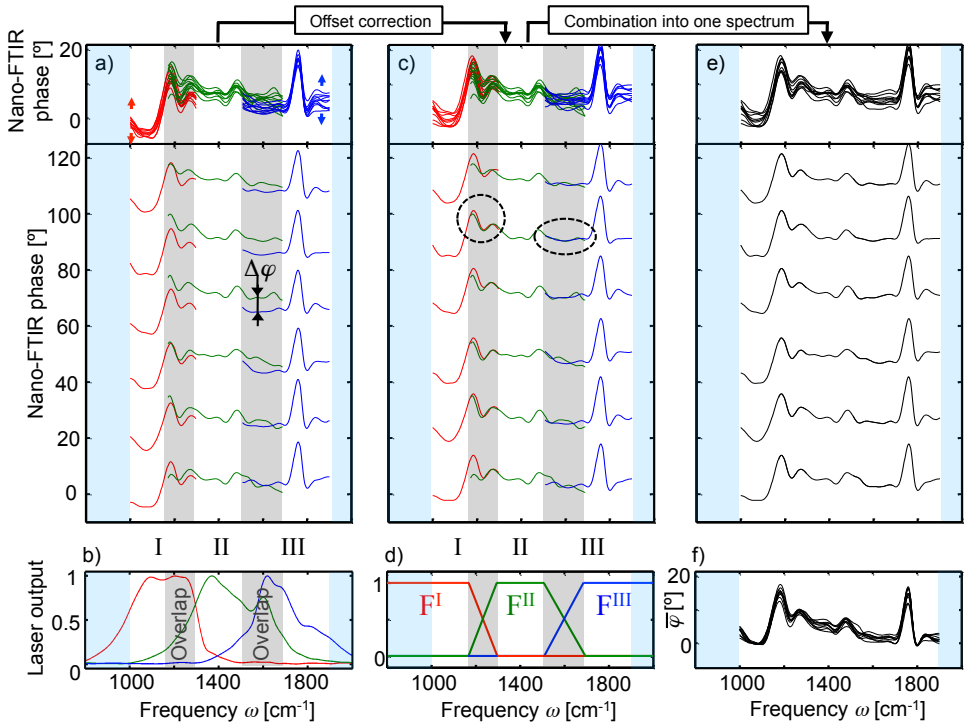

Fig. 7.4: **Stitching of bandwidth-limited nano-FTIR spectra**. **(a)** Bandwidth-limited nano-FTIR phase spectra from six subsequent pixels of the hyperspectral data cube shown in Fig. 7.1. **(b)** Laser output spectra. **(c)** Spectra of (a) after offset correction. **(d)** Functions F^{I}, F^{II} and F^{III}. **(e)** Broadband nano-FTIR spectra after stitching. **(f)** Broadband nano-FTIR spectra after stitching and baseline correction. The top panels of Fig. 7.4a,c,e show all nano-FTIR spectra plotted on top of each other, while the bottom panels show the same spectra plotted for each pixel separately.

Procedure for phase offset correction

In order to correct the phase offset, we shift at each pixel (x,y) the phase spectra $\bar{\varphi}^{I}(\omega)$ and $\bar{\varphi}^{III}(\omega)$ by the constant phase values $c^{\mathrm{I}} = \overline{\varphi^{I}(\omega)} - \overline{\varphi^{II}(\omega)}$ and $c^{\mathrm{III}} = \overline{\varphi^{III}(\omega)} - \overline{\varphi^{II}(\omega)}$ (the average values are evaluated in the corresponding spectral overlap regions marked grey in Fig. 7.4), in order to match $\overline{\varphi^{II}(\omega)}$. The offset-corrected phase spectra are shown in Fig. 7.4c. We find that the spectral features (marked by dashed black circles) in the overlapping regions are now well matched for all pixels, thus verifying the validity and reliability of our rather simple offset-correction procedure.

Finally, we combine the three offset-corrected spectra at each pixel to obtain a single broadband nano-FTIR phase spectrum. To achieve a smooth transition between the spectral ranges, we multiply the phase spectra $\varphi^{k}(\omega)$ by the functions $F^{k}(\omega)$ shown by the red, green and blue graphs in Fig. 7.4d. Subsequently, the spectra are summed up. The final broadband nano-FTIR phase spectra are shown in Fig. 7.4e. Altogether, this methodology enables an automatized combination of bandwidth-limited data cubes to one hyperspectral data cube.

Origin of phase offset fluctuations

We plot in Fig. 7.5b the offset $\Delta\varphi$ between the phase spectra φ^{II} and φ^{III} comprising the hyperspectral data cube of Fig. 7.1d as a function of spatial position (x,y), yielding a phase offset map $\Delta\varphi(x,y)$. For interpreting the data, note that the individual phase spectra of each horizontal line were normalized to the averaged reference spectrum of the same line, which was obtained on the silicon area (black area on the left side of the topography image shown in Fig. 7.5a). For each line, we observe that $\Delta\varphi$ slightly fluctuates around 0 degree on the silicon area, which can be attributed to fluctuations of the effective interferometer path length caused by air turbulences or convection. For increasing distance from the silicon area, we find that $\Delta\varphi$ in numerous lines tends to either increase or decrease (as can be seen more clearly for the two line profiles shown in Fig. 7.5c). This observation lets us assume that $\Delta\varphi$ originates from a drift of the WLP caused by a relative drift of the interferometer path lengths.

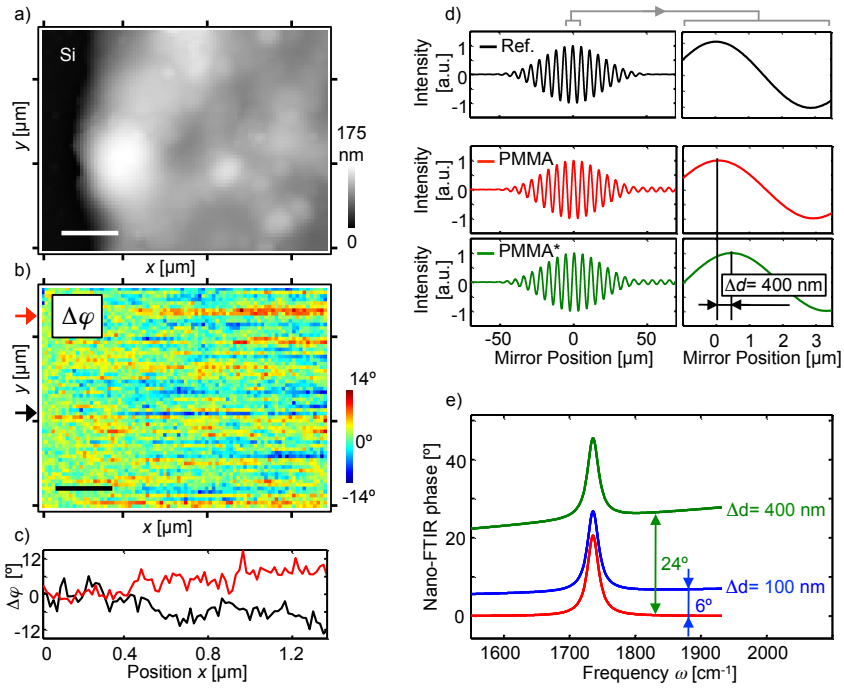

Fig. 7.5: **Origin of offset fluctuations of phase spectra**. **(a)** Topography of the sample area where the hyperspectral data cube was recorded. Scale bar, 300 nm. **(b)** 82 x 62 pixel map showing the offset $\Delta\varphi(x,y)$ between the nano-FTIR phase spectra $\varphi^{II}(x,y)$ and $\varphi^{III}(x,y)$. Scale bar, 300 nm. **(c)** Phase offset $\Delta\varphi$ along the lines marked by the red and black arrows in Fig. 7.5b. **(d)** Simulated interferograms for a silicon reference sample (black) and PMMA sample (red, green). The green interferogram is identical to the red interferogram, but shifted by 400 nm in order to mimic a shift of the WLP, i.e. a drift of the interferometer path length against each other. Right: Zoom into the interferogram around the WLP. **(e)** Calculated phase spectra of PMMA (red and green) normalized to a reference spectrum. Sample and reference spectra were correspondingly obtained by Fourier transform of the interferograms shown in Fig. 7.5d. The blue spectrum was obtained by Fourier transform of an interferogram that was shifted by 100 nm compared to the reference interferogram and subsequent normalization.

To elucidate how the drift of the WLP shifts the offset of the normalized phase spectrum, we calculated theoretical reference and PMMA interferograms (black and red curves in Fig. 7.5d). The reference interferogram was calculated by Fourier transformation of a bandwidth-limited virtual laser output spectrum. The PMMA interferogram was calculated by Fourier transformation of a complex-valued infrared spectrum of a Lorentz oscillator at 1730 cm^{-1} (being a proxy for the C=O stretching) illuminated by the virtual laser output spectrum. To mimic a shift of the WLP, i.e. a drift of the interferometer path length against each other, we shift the sample interferogram by 400 nm to the right, yielding the green interferogram in d. Fourier transform of the shifted (green) interferogram and normalization to the Fourier transform of the reference (black) interferogram of Fig. 7.5d yields a phase spectrum (green curve in Fig. 7.5e), which baseline is tilted around $\omega = 0$ cm^{-1} leading to a phase offset $\Delta\varphi$ of about 24 degrees at around 1730 cm^{-1} compared to the original phase spectrum (red curve in Fig. 7.5e). We also show in Fig. 7.5e a phase spectrum (blue) obtained by Fourier transform of an interferogram that was shifted by 100 nm compared to the reference interferogram (black curve in Fig. 7.5d). The smaller interferometer shift results in a smaller phase offset $\Delta\varphi$ of about 6 degree, while the tilting of the baseline is barely recognized. The calculations of Fig. 7.5d,e support our explanation that the offset of normalized phase spectra is caused by an interferometer drift between the recording of the reference and sample spectra. A WLP drift as small as 100 nm yields a phase offset of about 6 degrees, which is in the range of the experimentally observed phase offsets (Fig. 7.5b). Taking into account that the time between reference and sample measurement in one line of Fig. 7.5b can take up to 136 s (one line consists of 82 pixel, while one spectrum requires 1.66 s), the WLP was drifting by about 50 nm per minute. Such drift is relatively small and unavoidable, considering that the interferometer was not stabilized and exposed to the lab environment without any enclosure. A drift of 50 nm relative to an interferometer path length of about 6 cm corresponds to a relative drift of about 10^{-6}. Importantly, according to our calculations, for small phase offsets similar to the ones observed in our experiments (i.e. about 6 degrees) the tilting of the baseline is barely noticeable.

7.7 Baseline correction

Baseline correction is a basic correction method in far-field FTIR spectroscopy, where different algorithms are used (i.e. linear, polyline, etc.) to define the baseline to be corrected [4], [120], [121]. In nano-FTIR a linear baseline correction is applied manually to the recorded phase spectrum (see chapter 5.7). Here we apply an automatic linear baseline correction to correct each individual broadband phase spectrum. The advantage of baseline correction is demonstrated in Fig. 7.6, where we compare phase images and phase spectra (extracted from hyperspectral data cube of Fig. 7.1d) before and after baseline correction.

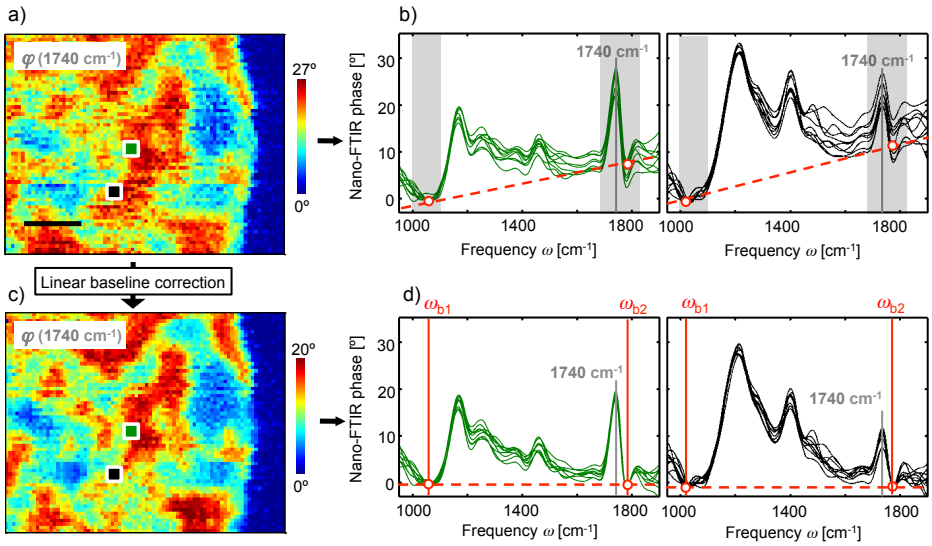

Fig. 7.6: **Baseline correction**. **(a)** Phase image at 1740 cm^{-1} extracted from the hyperspectral data cube shown in Fig. 7.1 prior to linear baseline correction. Scale bar, 300 nm. **(b)** Nine phase spectra (3x3 pixels) extracted from regions marked by squares in Fig. 7.6a. The spectra of the left diagram (green) were taken on a AC-rich region (marked by green symbol in (a)). The spectra in the right diagram (black) were taken on a FP-rich region (marked by black symbol in (a)). **(c,d)** Same data as in (a) and (b), respectively, but extracted from the hyperspectral data cube after linear baseline correction. The grey areas in (b) show the spectral regions at which the frequencies with minimum phase value where selected. Red dashed lines show the baseline of one of the nano-FTIR phase spectra.

The baseline correction is done as follows. Based on far-field FTIR spectra of the sample components (see Fig. 7.7), two spectral regions are first selected (marked as grey areas in Fig. 7.6b) at which all the components have at least one non-absorbing (or negligibly absorbing) frequency. Having selected the two spectral regions, at each pixel of the hyperspectral data cube, the frequencies are determined where the phase (corresponding to absorption) in the two selected spectral regions assumes its minimum value ω_{b1} and ω_{b2}. An example of this procedure is illustrated in Fig. 7.6b, where the two frequencies used for baseline correction are marked by red open circles. Note that the evaluated spectral regions are the same for all pixels, while the selected frequencies may be different. The line determined by the phase values $\Delta\varphi(\omega_{b1})$ and $\Delta\varphi(\omega_{b2})$ is defined as the baseline (marked as dashed red line in Fig. 7.6b) and is subtracted from the phase spectrum (illustrated in Fig. 7.6d). The baseline correction is performed individually for all phase spectra of the hyperspectral data cube. It allows for reliable and automatic baseline correction of the individual spectra, provided that all spectra have at least one non-absorbing frequency in the selected spectral ranges. Fig. 7.6d clearly shows that the linear baseline correction does not alter the spectral features of individual spectra. However, most importantly, it reduces fluctuations between neighboring spectra (compare Fig. 7.6b and Fig. 7.6d), and hence significantly improves the SNR of the images extracted from the hyperspectral data cube (compare Fig. 7.6a and Fig. 7.6c).

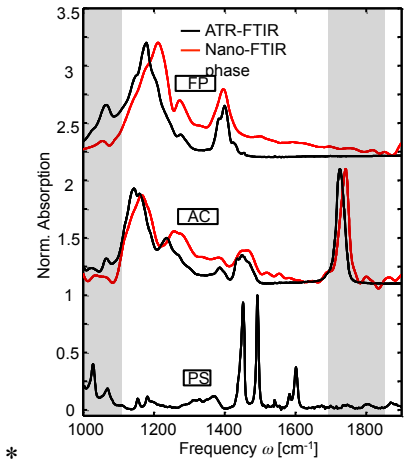

Fig. 7.7: **Comparison of nano-FTIR and ATR-FTIR spectra of polymers**. Nano-FTIR (red, 16 cm^{-1} spectral resolution) and ATR-FTIR (black, 4 cm^{-1} spectral resolution) spectra of FP, AC and PS. For better visibility, we show the spectra with different offsets. For ATR-FTIR spectroscopy measurements we used the Frontier FT-IR/FIR spectrometer (Perkin Elmer) equipped with a universal ATR module (1 reflection with diamond/ZnSe top plates).

7.8 Conclusions

In summary, we introduced techniques and methods for recording nanoscale-resolved hyperspectral infrared images obtained with a tunable bandwidth-limited mid-infrared laser continuum. It relies on recording multiple bandwidth-limited data cubes of one and the same sample area, and stitching them together to one hyperspectral data cube. Key for the reliable and accurate stitching of the data cubes have been the implementation of methods for (i) regular sample drift correction during data acquisition, (ii) regular recording of reference spectra during data acquisition, (iii) correcting spectral offsets caused by unavoidable interferometer drift and (iv) baseline correction of the broadband nano-FTIR phase spectra analogous to far-field hyperspectral infrared imaging. Using a tunable DFG laser continuum with an effective spectral bandwidth of about 400 cm^{-1}, hyperspectral data cubes of about 5000 nano-FTIR spectra covering 1000 to 1900 cm^{-1} could be recorded in less than 8 hours.

By improving the power and spectral bandwidth of emerging infrared laser sources (a recent work demonstrates a 100 cm^{-1} broad laser continuum of about 100 mW that is tunable between 500 cm^{-1} and 3000 cm^{-1} [122]) and taking advantage of advanced spectral noise reduction strategies (i.e. principal component analysis based noise reduction), we envision high-quality, hyperspectral infrared nanoimaging with few wavenumber spectral resolution on a time scale of one hour.

8 Demonstration of chemical mapping by hyperspectral infrared nanoimaging

Having developed the hyperspectral infrared nanoimaging technique (described in chapter 7), in this chapter we demonstrate its application potential with a polymer blend and a human hair cross-section. We demonstrate that in combination with multivariate data analysis, hyperspectral infrared nanoimaging provides nanoscale-resolved chemical and compositional maps, yielding valuable insights into the spatial distribution of polymers. More important, it enables the identification and spatial mapping of nanoscale-size areas where chemical interactions between polymers occur. Furthermore, our studies of a hair cross-section demonstrate the capacity of hyperspectral infrared nanoimaging to identify and chemically analyze melanin molecules within their granula, without requiring deleterious extraction or tagging processes.

8.1 Introduction

The hyperspectral infrared nanoimaging technique described in chapter 7 allows for the recording of hyperspectral data cubes of thousands of nano-FTIR spectra covering the spectral range from 1000 to 1900 cm^{-1}. Generaly, hyperspectral data cubes contain a huge amount of spatially resolved chemical and structural information that can yield relevant insights about the studied samples. However, the analysis and interpretation of hyperspectral data cubes and subsequent extraction of relevant application-related information is rather challenging. Thus, complex multivariate data analysis algorithms have been developed in order to analyze hyperspectral data cubes recorded by different far-field techniques such as infrared [16], [19], [21] and Raman [23], [24] spectroscopy or EELS [25]. A hyperspectral image can be segmented based on a unsupervised hierarchical cluster analysis [66], [123], revealing the spatial distribution of areas with the same, or similar, spectroscopic information. Another, less-standard approach, is to create "distance maps" (i.e. similarity maps) using reference spectra, which allows for mapping the relative content of target components. In distance maps, a high color intensity denotes a low inter-spectral distance (or high similarity) between the actual point spectrum and a given reference spectrum. By superpositioning several distance maps obtained with different reference spectra, composite maps can be constructed (i.e. maps of the relative content of several components). In combination with multivariate data analysis, hyperspectral infrared nanoimaging could have a wide application potential for valuable chemical materials characterization in various fields ranging from materials sciences to biomedicine.

In the following, we demonstrate that valuable multivariate analysis of hyperspectral infrared nanoimages can be performed using a standard software package. In particular, we used the CytoSpec software package (CytoSpec, Berlin/Germany), which is a specialized software package for vibrational hyperspectral imaging.

In chapter 8.2 we apply CytoSpec to analyze hyperspectral data of a polymer blend relevant for coating applications, which is based on a fluorine copolymer (referred as to FP), an acrylic copolymer (AC), and a polystyrene latex (PS) (for details and fabrication see chapter 8.2.1). Polymer blends are used in a wide variety of applications (ranging from consumer electronics to aerospace) because they often exhibit properties that are superior to any one of the component polymers alone. However, the manifestation of such superior properties depends strongly upon the nanoscale distribution of the individual components (i.e. miscibility) [124], [125]. Therefore, nanoscale characterization tools are needed for the development of high performance polymer blends, as well as for quality control purposes [126]. Characterization of polymer blends (i.e. morphology, chemical composition and/or polymer interactions) currently requires the combination of different complex techniques [127] (i.e. AFM, staining-based TEM, optical microscopy techniques), which only partially provide nanoscale or chemical information. In the following we show that in combination with multivariate data analysis, hyperspectral infrared nanoimaging can meet the strong demand for highly-sensitive nanoscale chemical mapping of the spatial distribution and local chemical interaction of the polymer components.

In chapter 8.3 we apply hyperspectral infrared nanoimaging, together with CytoSpec, to perform the first *in-situ* infrared-vibrational chemical analysis of native melanin in human hair medulla. Melanin is a polymer pigment, present in the human hair and skin, and responsible for tissue coloring and UV photoprotection [128]. Due to its photo absorbing properties, melanin has attracted large attention from cosmetic and solar energy industries [129], [130]. Unfortunately, it has revealed impossible to analyze human melanin without extracting it from hair or tissue, which comes along with potential damage and modification [131], [132].

8.2 Chemical mapping of a three-component polymer blend.

Fig. 8.1a shows the topography image of the about 170 nm thick spin-coated polymer blend on silicon. The hyperspectral infrared data cube recorded on this sample area was already shown in Fig. 7.1d. The good reproducibility of the individual spectra (see Fig. 8.1b showing four sets of neighboring point spectra at the sample positions A to D marked in Fig. 8.1a,d) allow for valuable multivariate analysis based on established procedures known from far-field infrared spectroscopy.

8.2.1 Sample preparation

Three water-based polymer dispersions made by emulsion polymerization were employed for the preparation. Table 1 summarizes their main characteristics.

	Composition (% weight)	Particle diameter dp (nm)
PVDF/HFP	95/5	129
MMA/BA/AA	49.5/49.5/1	144
PS/AA	99/1	109

Table 1: **Main characteristics of the three water-based polymer dispersions employed to prepare the polymer blend**.

Three-component polymer blend for hyperspectral infrared nanoimaging: The three polymer dispersions listed in table 1 were separately diluted at 0.2% solids content and mixed into a single dispersion by stirring. Then, the mixture was casted onto a silicon wafer through spin coating. Finally, the silicon wafers were dried in an oven overnight at 120ºC. Proportions were chosen in order to obtain a blend for coating applications. The final dispersion contained 40% of a polyvinyledene fluoride (PVDF) and hexafluoropropylene (HFP) copolymer; 40% of an acrylic copolymer made of methyl methacrylate (MMA), butyl acrylate (BA) and acrylic acid (AA); and 20% of a high glass transition temperature (Tg) latex based on polystyrene to improve mechanical properties without the need of any film forming aids [133].

Polymer reference samples for nano-FTIR: The three polymer dispersions listed in table 1 were separately diluted at 0.2% solids content. Each one was individually casted onto a silicon wafer through spin coating. Finally, the silicon wafers were dried in an oven overnight at 120ºC.

Polymer reference samples for ATR-FTIR spectroscopy: The three polymer dispersions listed in table 1 were diluted at 1% and casted onto separate glass substrates and dried overnight at 120 ºC. The obtained polymer layers were several μm thick.

8.2.2 Inter-spectral distance mapping using nano-FTIR reference spectra

We applied inter-spectral distance mapping, where we calculate for each pixel spectrum $S(x,y)$ the multivariate spectral Euclidean distance $D(x,y)$ between the point spectrum and a reference spectrum. The distance values are converted into color scales and plotted as specifically colored pixels at the positions (x,y). In the resulting distance maps, high color intensity denotes a small distance (high similarity) with the reference spectrum (and vice versa). With nano-FTIR phase spectra obtained from reference samples made of pure AC and FP components (black spectra in Fig. 8.1b, see chapter 8.2.1 for sample preparation details), we obtained the distance (similarity) maps for the AC (red) and FP (blue) components shown in Fig. 8.1c. Superposition of these two

maps yields a compositional map (Fig. 8.1d), which highlights areas with the highest relative content of each polymer.

We observe homogenous but distinct red and blue areas for the two different references, indicating that the AC and FP components are not fully mixed but rather separated. On the red areas, representative spectra (B) match well with the AC reference (black reference spectrum in Fig. 8.1b), indicating the presence of pure AC (illustrated by situation B in Fig. 8.1g). Within the blue areas, interestingly, representative spectra (D in Fig. 8.1b) show FP peaks at low frequencies ($\omega < 1500$ cm^{-1}) but also the C=O peak of AC at 1740 cm^{-1}. It can be shown (see chapter 8.2.4) that the spectra at position D are a linear superposition of the pure FP and AC spectra, which lets us conclude that both FP and AC are present within the volume probed by the near field below the tip apex (represented in Fig. 8.1g by the reddish elliptical area below the tip apex). We conclude that FP forms cluster-like nanostructures, while AC is spread all over the sample surface. For that reason, the near field below the tip apex probes both the FP cluster and AC layer below the FP cluster (illustrated by situation D in Fig. 8.1g). We explain this finding by the differences in viscosity, molecular weight and/or chain stiffness. On the other hand, the clearly visible spatial dispersion of AC and FP - avoiding the formation of percolation networks – indicates that AC and FP are miscible even at the nanoscale. Note that any improvement of film formation or film homogenization by mixing or optimizing drying conditions was beyond the scope of this study.

In Fig. 8.1d we also observe black areas on the polymer blend, indicating that the similarity of the local spectra (A in Fig. 8.1b) is low compared to the FP and AC reference spectra. We explain these areas by the dominating presence of PS (illustrated by situation A in Fig. 8.1g). Note that we did not perform distance mapping with PS references, as the peaks in nano-FTIR phase spectra of pure PS reference sample are comparably weak. It seems that the oscillator strength of the PS bonds is much weaker than in other polymers, and thus is not detected with the current nano-FTIR setup.

Interestingly, Fig. 8.1d reveals purple areas (marked C in Fig. 8.1g), which indicate local spectral differences compared to both the AC (red) and FP (blue) regions. Indeed, representative spectra (marked C in Fig. 8.1b) of the purple areas cannot be reproduced by a linear superposition of AC and FP reference spectra (see chapter 8.2.4). Compared to the red AC spectrum (B), the C=O peak at 1740 cm^{-1} is reduced, indicating that the amount of AC in the probing volume of the tip is reduced. On the other hand, the peak at 1155 cm^{-1} is significantly increased. We attribute this finding to the presence of FP and its chemical interaction with AC. Note that chemical interactions are known to cause peak shifts [107] and increase of peak heights [134]. Specifically, we assume a spectral shift of the CF_2 stretching vibration of FP from 1195 cm^{-1} towards lower frequencies, most likely due to the formation of hydrogen bonding between the C-F bonds of FP and the acrylic polymer chains [135], [136]. Further, the C-O stretching of the ester bond of AC at 1155 cm^{-1} may be enhanced due to the chemical interaction. The concerted action of both effects could thus explain the enhanced peak at 1155 cm^{-1} that

is found in the purple regions, which consequently indicate the areas where the AC and FP components are well mixed.

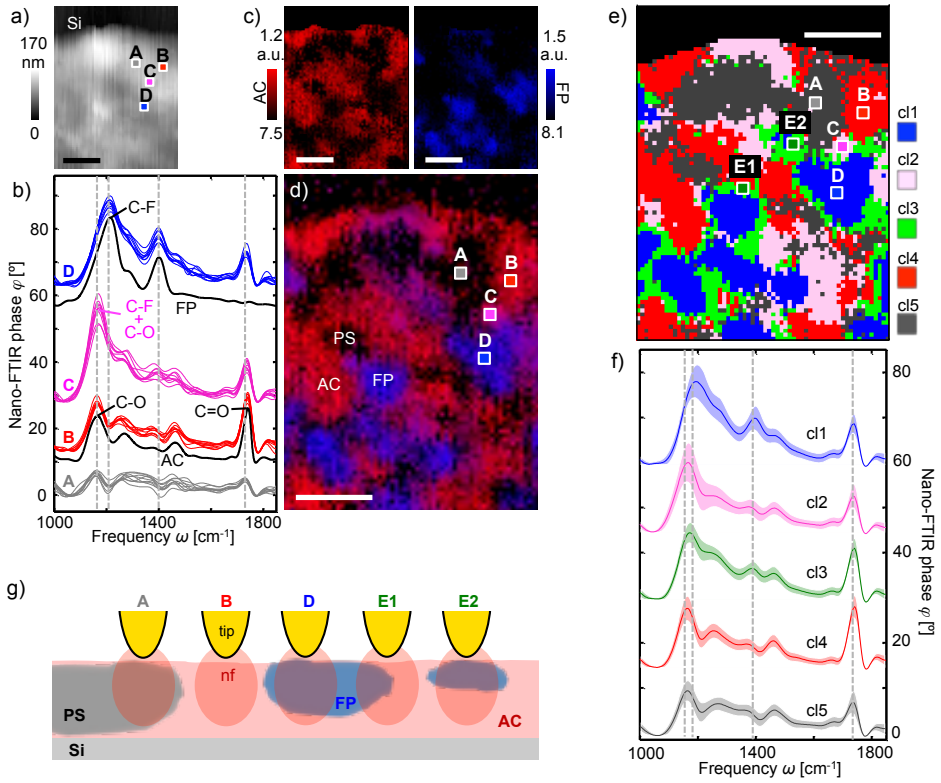

Fig. 8.1: **Chemical nanomapping of polymers**. **(a)** Sample topography. **(b)** Black curves show nano-FTIR phase spectra of FP and AC reference samples (44 min total acquisition time; 35 cm^{-1} resolution). Colored curves show the nine nano-FTIR phase spectra in the areas marked A, B, C and D in Fig. 8.1a and d, extracted from the data cube shown in Fig. 7.1d. All spectra are vertically offset. **(c)** Spatial maps of AC and FP obtained by inter-spectral distance mapping. **(d)** Compositional map, obtained by superposition of the maps of Fig. 8.1c. **(e)** Cluster map obtained by multivariate data analysis (HCA algorithm). **(f)** Average nano-FTIR phase spectra and standard deviation of clusters cl_i (colored thin and thick lines, respectively). **(g)** Schematics of near-field probing at positions A-E2 marked in Fig. 8.1d and e. All scale bars are 400 nm.

8.2.3 Unsupervised cluster analysis

Next we demonstrate that valuable multivariate data analysis can be also performed without any reference spectra. To this end, we apply unsupervised hierarchical cluster analysis [137], where D-values were used as inter-spectral distance measures and Ward's method was employed as the clustering method. The hyperspectral data of Fig. 7.1d was segmented into 5 distinct clusters (denoted as cl1 to cl5, see Fig. 8.1e). We justify the choice of at least four clusters by our findings from inter-spectral distance mapping (Fig. 8.1d). On the other hand, segmentation into more than five clusters resulted essentially in further segmentation of the noisy dark PS-rich (dark) areas. In the future, a more detailed analysis could be applied to determine the optimal number of clusters [138], which, however, would go beyond the scope of this work. The cluster

segmentation map is shown in Fig. 8.1e, and the cluster spectra (colored) in Fig. 8.1f. The spectra and areas of clusters cl1, cl2, cl4 and cl5 agree well with Fig. 8.1b and Fig. 8.1d, respectively, corroborating the robustness and reliability of the data and the strategy of data analysis. Interestingly, unsupervised cluster analysis reveals another significant area (cluster cl3, green) which is not recognized in Fig. 8.1d, and which average spectrum (green curve in Fig. 8.1f) can be reconstructed by a linear superposition of AC and FP reference spectra (see chapter 8.2.4). We explain it by either a lateral (illustrated by situation E1 in Fig. 8.1g) or vertical (illustrated by situation E2 in Fig. 8.1g) arrangement of AC and FP within the volume probed by the tip´s near field. For that reason, the green areas indicate interfacial areas without chemical interaction, in contrast to the purple regions where peak shifts indicate significant chemical interaction. Note that polymer chain interactions depend on several factors such as distance between interacting groups, orientation or steric hindrance [134], [135], and thus may occur only partially at the interface between AC and FP.

8.2.4 In depth analysis of nano-FTIR spectra recorded on the polymer blend

To obtain more details about the presence of pure, or "modified", AC and FP components along the sample, we analyzed the contributions of reference nano-FTIR spectra of AC and FP to the average nano-FTIR spectra of clusters shown in Fig. 8.1e. In particular, the reference nano-FTIR phase spectra of AC and FP (bottom solid black lines in Fig. 8.2a) were linearly superimposed in order to reproduce the average nano-FTIR phase spectra of the clusters. For each cluster, a best fitting spectrum was obtained by multiplication of the reference spectra by factors K_{AC} and K_{FP}, and subsequent addition. Average nano-FTIR phase spectra of the clusters are shown by the colored lines in Fig. 8.2a, and the corresponding fits by the dashed black lines. The factors K_{AC} and K_{FP} (see Fig. 8.2b) were manually adjusted in order to fit both the height of the peak at 1735 cm^{-1} (exclusive contribution of AC, marked by vertical grey line) and the height of the peak in the range of 1100 - 1200 cm^{-1} (contribution of both AC and FP, marked by the grey area).

The average nano-FTIR spectra of most of the clusters (i.e. cl1, cl3-cl5) can be reproduced by a linear superposition of AC and FP reference spectra, which indicates that pure AC and FP components are present at these clusters (i.e. areas). However, the average spectrum of cl2 cannot be reproduced. This finding indicates that the purple spectrum originates from the presence of components that are modified compared to the corresponding reference samples. We explain the modified infrared spectral response by a chemical interaction between AC and FP (see chapter 8.2.2 for more detailed discussion).

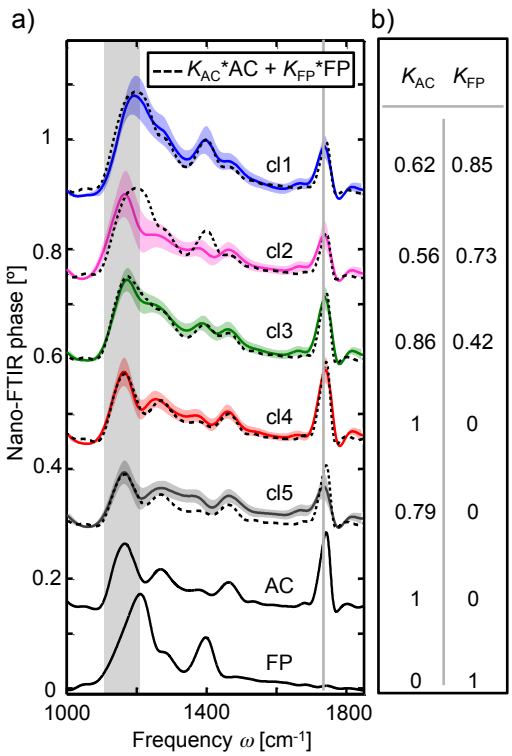

Fig. 8.2: **Reproducing cluster average nano-FTIR spectra of Fig. 8.1. (a)** Average nano-FTIR phase spectra and standard deviation of the clusters cl1 to cl5 (colored thin and thick lines, respectively), corresponding fitted nano-FTIR phase spectra (dashed black curves) and reference nano-FTIR phase spectra of AC and FP (bottom, solid black curves). **(b)** Multiplication factors applied for fitting the average spectra of the individual clusters.

8.2.5 Inter-spectral distance mapping using ATR-FTIR reference spectra

In the following we show that similar compositional maps as the ones shown in Fig. 8.1d can be obtained using far-field infrared reference spectra of the pure AC and FP samples, rather than using nano-FTIR reference spectra. To this end, we take the hyperspectral data cube of the polymer blend (shown in Fig. 7.1d) and apply the inter-spectral distance imaging method (same as applied in chapter 8.2.2) using external reference spectra of AC and FP polymers obtained by ATR-FTIR spectroscopy. The ATR-FTIR reference spectra and the obtained compositional map are shown in Fig. 8.3a. For comparison, external nano-FTIR reference phase spectra and the obtained compositional map are shown in Fig. 8.3b (same data as in Fig. 8.1d).

The nano-FTIR reference spectra have the same spectral resolution as the nano-FTIR spectra of the hyperspectral data cube (i.e. 35 cm^{-1}, see Fig. 7.7 for higher resolution AC and FP nano-FTIR phase spectra). In order to test the general approach of using standard far-field FTIR reference spectra (i.e. taken from a standard FTIR spectroscopy database), we used ATR-FTIR reference spectra with a spectral resolution of 4 cm^{-1} typically used in standard far-field FTIR spectroscopy.

Most important, we observe that the compositional maps shown in Fig. 8.3a and Fig. 8.3b are very similar and reveal the same blue, red, black and purple areas, demonstrating that standard reference spectra can be applied for automatic compositional mapping with the use of hyperspectral data cubes based on nano-FTIR.

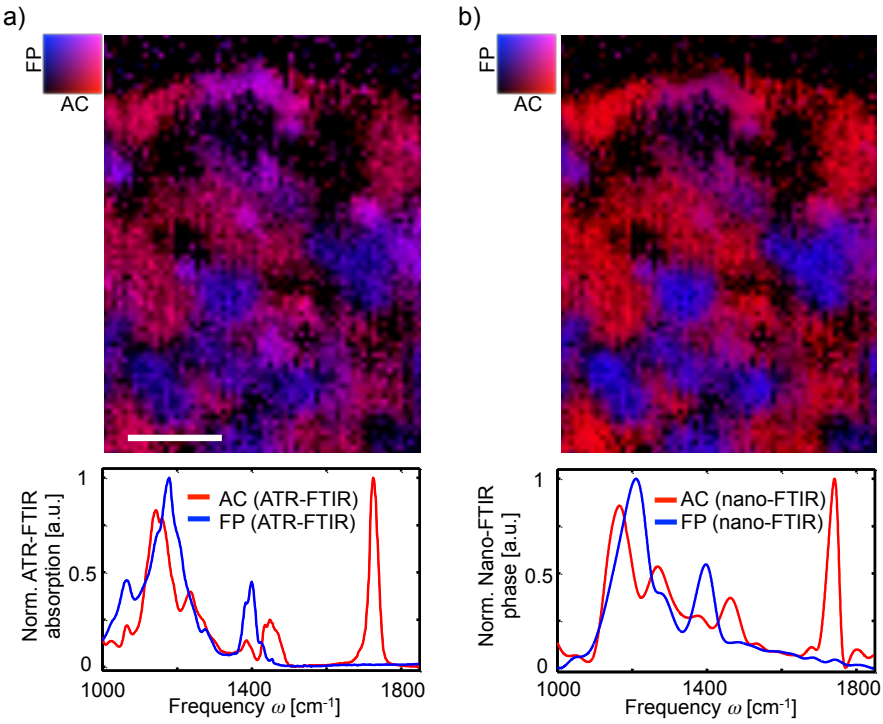

Fig. 8.3: **Compositional maps obtained with different reference spectra**. **(a)** Compositional map (top) of the polymer blend of Fig. 8.1, which was obtained with ATR-FTIR reference spectra (bottom, 4 cm^{-1} spectral resolution) of AC (red line) and FP (blue line). Scale bar, 400 nm. **(b)** Compositional map (top) of the polymer blend of Fig. 8.1, which was obtained with nano-FTIR reference phase spectra (bottom, 35 cm^{-1} spectral resolution). All spectra are normalized to their maximum values.

The SNR and the color contrast in Fig. 8.3a is a bit lower than in Fig. 8.3b, which can be explained by the slight spectral shifts between ATR-FTIR and nano-FTIR spectra [59], [85], [112]. Note that original ATR-FTIR spectra (normalized to their maximum absorbance but without any spectral shifting or other post-processing) were used for the analysis.

The possibility of performing inter-spectral distance mapping and obtaining similar compositional maps with far-field infrared reference spectra enables rapid hyperspectral data analysis (i.e. idendification of specific target components) based on standard references without the need of nano-FTIR reference spectra.

8.3 In-situ chemical mapping of native melanin in human hair medulla

8.3.1 Sample preparation

A clean human hair was cut into small pieces and embedded in epoxy resin (Epon ™ kit substitute embedding medium, Aldrich). The sample was cured during 24 hours at 60 °C. The block containing the human hair was trimmed with fresh glass knife made with Leica knifemakerTM and then ultramicrotomed with Leica UCTTM using DiatomeTM 45 diamond knife. The photograph of the resulting sample, captured by the camera incorporated at the NeaSNOM microscope, is shown in Fig. 8.4 where the resin embedded hair cross-section can be seen.

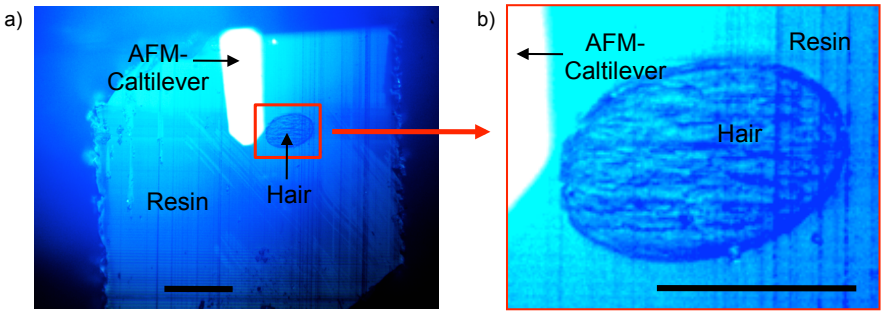

Fig. 8.4: **Hair cross-section sample**. **(a)** Photograph of the sample captured by the camera incorporated at the NeaSNOM microscope, the hair, resin and the AFM cantilever are observed. Scale bar, 100 μm.**(b)** zoomed in image of area marked with a red square in Fig. 8.4a. Scale bar, 50 μm.

8.3.2 Identification and chemical analysis of melanin granules

Fig. 8.5a shows the topography of a resin-embedded cross-section of a human hair. In the infrared near-field image taken with a QCL at 1660 cm^{-1} we observe an enhanced infrared absorption of the cuticle and cortex regions compared to the resin, owing to the strong amide I absorption of the hair proteins (α-keratin microfibrils). Within the cortex region we find disk-shaped areas of about 300 nm diameter, where the infrared absorption is reduced (i.e. the protein content is reduced). Their size and distribution corresponds to that of melanin granules observed in electron microscopy images [139]. However, we find that nano-FTIR phase spectra of the individual granules can differ significantly from each other. To elucidate the spectroscopic variations, we performed hyperspectral infrared nanoimaging of the area marked by dashed black line in Fig. 8.5a.

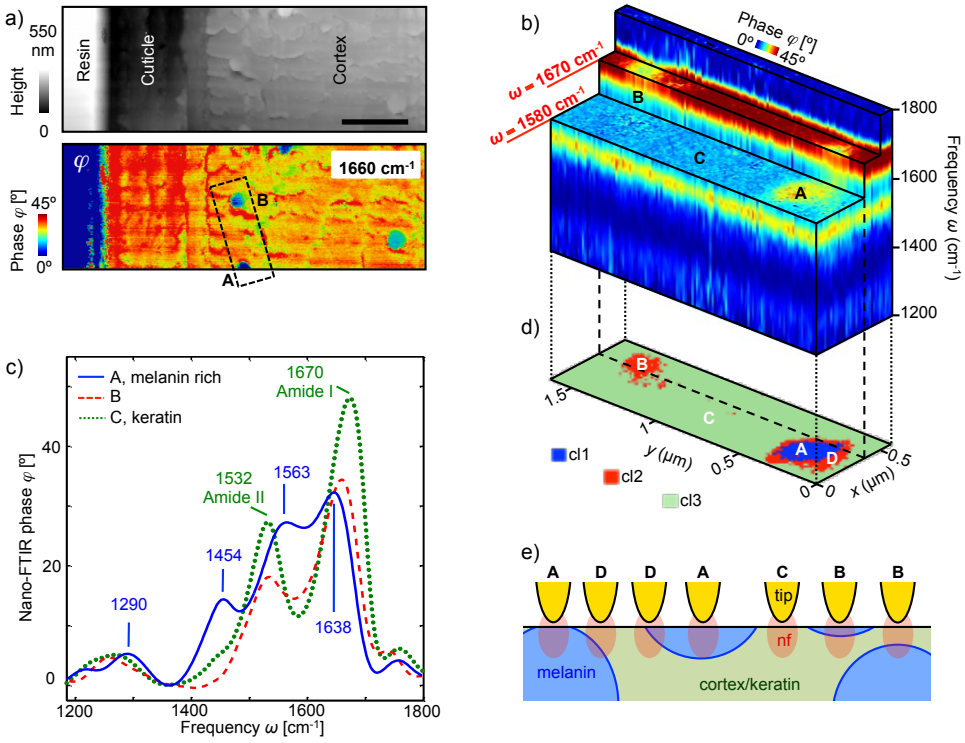

Fig. 8.5: **Identification and chemical analysis of native melanin in human hair**. **(a)** Top: Topography of resin-embedded human hair microtome cross-section. Bottom: Infrared near-field phase image φ at 1660 cm^{-1}. Scale bar, 1 μm. **(b)** Hyperspectral infrared data cube with spectral resolution of 35 cm^{-1} partially cut at different frequencies ω. It shows the phase of the tip-scattered light as a function of position (x,y) and frequency ω. The dashed black rectangle in Fig. 8.5a shows the area where the data cube was recorded. **(c)** Nano-FTIR phase spectra (average over nine neighboring pixels) at positions marked by A, B and C in Fig. 8.5a,b and d, extracted from the data cube shown in Fig. 8.5d. **(d)** Cluster map obtained by multivariate data analysis (HCA algorithm). **(e)** Schematics of near-field probing at positions A-D marked in Fig. 8.5d.

From the hyperspectral data cube (Fig. 8.5b) we extracted spectra at different positions. Within the cortex region (position C, green spectrum in Fig. 8.5c) we observe the well-known amide I and II bands being typical for protein (α-keratin). For particle A (blue curve in Fig. 8.5c) we observe four distinct peaks that are characteristic for melanin: at 1290 cm^{-1} (-C-OH phenolic stretching), 1454 cm^{-1} (C-C aliphatic stretches), 1563 cm^{-1} (indole N-H bending) and 1638 cm^{-1} (C=C, C=O, and/or COO- stretching in aromatic cycle), [140]. On particle B – supposed to be a melanin granule – the nano-FTIR phase spectrum significantly differs from that of particle A. Surprisingly, spectrum B shows more similarity to the keratin spectrum of the cortex region (C), although the amid I and II peaks are shifted by several cm^{-1}. Further, while both particles A and B are seen in the monochromatic image at 1670 cm^{-1}, only particle A exhibits a contrast at 1580 cm^{-1} (see corresponding slices of the data cube in Fig. 8.5b). Obviously, a set of images and local spectra is not sufficient to clarify the identity of particle B. However, having acquired a

full hyperspectral data cube, we can take advantage of multivariate data analysis. Since there are no reference spectra available for natural melanin in hair, we performed unsupervised hierarchical cluster analysis of the hyperspectral data. The segmentation map resulting from cluster analysis with three clusters (Fig. 8.5d) reveals well-defined features, thus corroborating the applicability and robustness of cluster analysis to the nano-FTIR spectra.

In the segmentation map the particles A and B appear as homogenous, although as distinct clusters (circular blue and red areas, respectively). Most important, we find a red ring (D) around the blue central area of particle A, revealing that the corresponding spectra belong to the same cluster as those of particle B. It can be shown that the spectra of the red cluster (B and D) are a linear superposition of spectra A and C (see chapter 8.3.3). For the width of the red ring (D) we measure about 50 nm, which is in the range of the lateral spatial resolution. We thus conclude that the red ring highlights a steep interface between melanin and keratin (see illustrations D in Fig. 8.5e). The red area B, in contrast, is a closed disk-shaped area of about 200 nm diameter (i.e. larger than the spatial resolution). We thus conclude that spectra B of this area are due to a vertical arrangement of melanin and keratin, i.e. a horizontally oriented interface between them. Indeed, near-field probing can be sensitive to subsurface components [141], which lets us conclude that particle B is either a subsurface melanin granule or a thin slice of a melanin granule (see illustrations B in Fig. 8.5e) (note that melanin granules are elliptical vesicle of an aspect ratio of about 3:1).

In Fig. 8.6 we compare segmentation maps resulting from cluster analysis with three (Fig. 8.6a, identical to that of Fig. 8.5d) and four (Fig. 8.6b) clusters. The fourth cluster does not reveal any well-defined features. It rather yields a random segmentation of the keratin cluster due to noise-induced spectral variations. Segmentation of the data in more than 3 clusters thus does not provide any additional useful information.

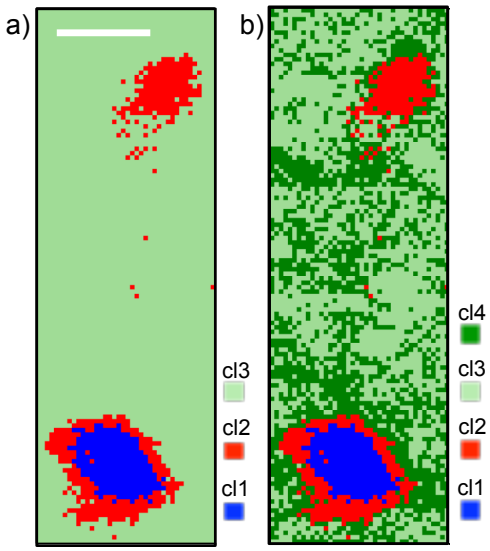

Fig. 8.6: **Comparison of cluster maps of the hair cross-section**. Segmentation maps of hair cross-section resulting from cluster analysis (HCA algorithm) for **(a)** 3 clusters and **(b)** 4 clusters. Scale bar, 300 nm.

8.3.3 In depth analysis of the nano-FTIR spectrum of particle B

In Fig. 8.7 we show that the nano-FTIR phase spectrum of particle B (cluster cl2, red spectrum) can be reproduced by a linear superposition of the nano-FTIR phase spectra of melanin (particle A, cluster cl1, blue spectrum) and keratin (cluster cl3, green spectrum). To that end, the nano-FTIR phase spectra of particle A and keratin were multiplied by the factors $K_{\text{particleA}} = 0.36$ and $K_{\text{keratin}} = 0.57$, respectively, and then added. The resulting spectrum is shown by the black curve in Fig. 8.7. It matches well the nano-FTIR phase spectrum (red) of particle B. We conclude that at position B the near field of the tip probes both keratin and melanin.

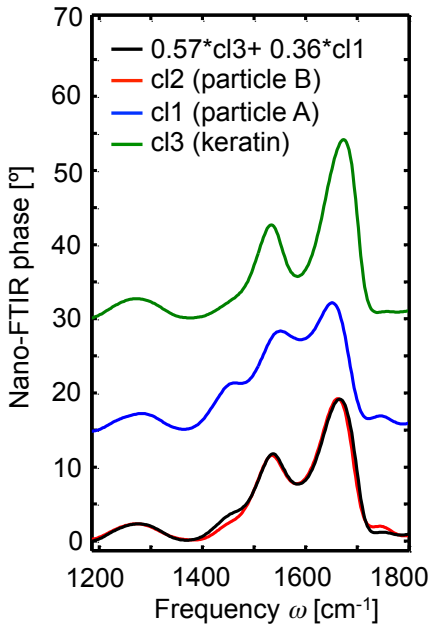

Fig. 8.7: **Analysis of spectrum of cluster cl2 of Fig. 8.5.** Average nano-FTIR phase spectra of the clusters cl1 to cl3 (blue, red and green, respectively), which were found in the hair cross-section by cluster analysis (data from Fig. 8.5b). The black spectrum shows a fit of the nano-FTIR phase spectrum of cluster cl2, which is based on a linear superposition of the nano-FTIR phase spectra of the clusters cl1 and cl3. For better visibility, we show the spectra with different offsets.

8.4 Conclusion

The results presented in this chapter clearly demonstrate that hyperspectral data cubes of several 1000 infrared spectra can be reliably obtained by nano-FTIR using a bandwidth-limited laser continuum. The hyperspectral data allow for multivariate analysis,

providing nanoscale maps of the spatial distribution of organic materials. Most important, multivariate analysis reveals two types of spectral peak shifts within the individual nano-FTIR phase spectra of the polymer and hair samples. In the simplest case, individual nano-FTIR phase spectra exhibit peak shifts, which can be reproduced by a linear superposition of the nano-FTIR phase spectra of the pure reference samples (for example on position D (blue area) on the polymer blend of Fig. 8.1, or on particle B in the hair sample of Fig. 8.5). It can be concluded that the spectra originate from the presence of the pure components (identical to that of the reference samples) in the volume probed by the near field below the tip. This can be the case, for example, at a sharp interface between pure components. In the second case, individual nano-FTIR phase spectra exhibit anomalous peak shifts, which cannot be reproduced by a linear superposition of the spectra of the pure reference samples. We conclude that the spectra originate from the presence of components, which are modified compared to the reference samples. We explain the modified spectral response by a chemical interaction between the adjacent components. Anomalous peak shift have been found on the purple areas in Fig. 8.1e, which most likely occurred due to chemical interaction between the FP and AC components of the polymer blend.

Our studies of the hair cross-section demonstrate the capacity of hyperspectral infrared nanoimaging to identify and chemically analyze melanin molecules within their granula, without requiring deleterious extraction or tagging processes. Through the analysis of the melanin-specific infrared peak position and intensity in the future one could estimate the impact of various cosmetic treatments (like bleaching, ironing, or coloring) on the chemical structure of the melanin polymer. Furthermore, analyzing the protein secondary structure [112] could allow for nanoscale spatial mapping of the impact of cosmetic treatments on the keratin fibrils and thus on the hair mechanical resistance.

We foresee a wide application potential of hyperspectral infrared nanoimaging in various fields of science and technology, ranging from materials sciences and pharmaceutical applications to biomedical imaging, and from fundamental research to quality control. In combination with multivariate data analysis, hyperspectral infrared nanoimaging yields nanoscale-resolved chemical and compositional maps, including the detection of nanoscale localized chemical interaction.

9 References

[1] A. Gutberlet, G. Schwaab, O. Birer, M. Masia, A. Kaczmarek, H. Forbert, M. Havenith, and D. Marx, "Aggregation-Induced Dissociation of HCl(H2O)4 Below 1 K: The Smallest Droplet of Acid" *Science*, vol. 324, no. 5934, pp. 1545–1548, 2009.

[2] Z. Q. Li, E. A. Henriksen, Z. Jiang, Z. Hao, M. C. Martin, P. Kim, H. L. Stormer, and D. N. Basov, "Dirac charge dynamics in graphene by infrared spectroscopy" *Nat. Phys.*, vol. 4, no. 7, pp. 532–535, 2008.

[3] F. Huth, "Nano-FTIR - Nanoscale Infrared Near-Field Spectroscopy" University of the Basque Country, 2015.

[4] P. R. Griffiths and J. A. de Haseth, "Fourier Transform Infrared Spectrometry". Wiley, 2007.

[5] A. A. Michelson, "XXVIII. Visibility of interference-fringes in the focus of a telescope" *London, Edinburgh, Dublin Philos. Mag. J. Sci.*, vol. 31, no. 190, pp. 256–259, 1891.

[6] A. A. Michelson, "Light waves and their uses". University of Chicago Press, 1903.

[7] A. A. Michelson, "On the application of interference-methods to spectroscopic measurements" *London, Edinburgh, Dublin Philos. Mag. J. Sci.*, vol. 31, no. 191, pp. 338–346, 1891.

[8] E. O. Brigham, "The Fast Fourier Transform and its applications" 1988.

[9] J. Connes, "Computing Problems in Fourier Spectroscopy" in *Aspen International Conference on Fourier Spectroscopy, 1970*, 1971, no. 114, p. 83.

[10] R. N. Bracewell and R. N. Bracewell, "The Fourier transform and its applications", vol. 31999. McGraw-Hill New York, 1986.

[11] G. M. Hale and M. R. Querry, "Optical Constants of Water in the 200-nm to 200-um Wavelength Region" *Appl. Opt.*, vol. 12, no. 3, pp. 555–563, 1973.

[12] R. G. Greenler, "Infrared study of adsorbed molecules on metal surfaces by reflection techniques" *J. Chem. Phys.*, vol. 44, p. 310, 1966.

[13] K. Nishikida, E. Nishio, and R. W. Hannah, "Selected applications of modern FT-IR techniques" 1995.

[14] H. A. Bethe, "Theory of diffraction by small holes" *Phys. Rev.*, vol. 66, no. 7, 8, p. 163, 1944.

[15] F. J. G. de Abajo, "Light transmission through a single cylindrical hole in a metallic film" *Opt. Express*, vol. 10, no. 25, pp. 1475–1484, 2002.

[16] S. E. Glassford, L. Govada, N. E. Chayen, B. Byrne, and S. G. Kazarian, "Micro ATR FTIR imaging of hanging drop protein crystallisation" *Vib. Spectrosc.*, vol. 63, pp. 492–498, 2012.

[17] S. M. Ali, F. Bonnier, H. Lambkin, K. Flynn, V. McDonagh, C. Healy, T. C. Lee, F. M. Lyng, and H. J. Byrne, "A comparison of Raman, FTIR and ATR-FTIR micro spectroscopy for imaging human skin tissue sections" *Anal. Methods*, vol. 5, no. 9, pp. 2281–2291, 2013.

[18] A. J. Sommer, L. G. Tisinger, C. Marcott, and G. M. Story, “Attenuated total internal reflection infrared mapping microspectroscopy using an imaging microscope” *Appl. Spectrosc.*, vol. 55, no. 3, pp. 252–256, 2001.

[19] E. N. Lewis, P. J. Treado, R. C. Reeder, G. M. Story, A. E. Dowrey, C. Marcott, and I. W. Levin, “Fourier transform spectroscopic imaging using an infrared focal-plane array detector” *Anal. Chem.*, vol. 67, no. 19, pp. 3377–3381, 1995.

[20] R. Salzer and H. W. Siesler, “Infrared and Raman spectroscopic imaging” John Wiley & Sons, 2009.

[21] K. L. A. Chan and S. G. Kazarian, “New opportunities in micro-and macro-attenuated total reflection infrared spectroscopic imaging: spatial resolution and sampling versatility” *Appl. Spectrosc.*, vol. 57, no. 4, pp. 381–389, 2003.

[22] C. Ricci, S. Bleay, and S. G. Kazarian, “Spectroscopic imaging of latent fingermarks collected with the aid of a gelatin tape” *Anal. Chem.*, vol. 79, no. 15, pp. 5771–5776, 2007.

[23] T. Ideguchi, S. Holzner, B. Bernhardt, G. Guelachvili, N. Picqué, and T. W. Hänsch, “Coherent Raman spectro-imaging with laser frequency combs” *Nature*, vol. 502, no. 7471, pp. 355–358, 2013.

[24] J. A. Timlin, A. Carden, M. D. Morris, J. F. Bonadio, C. E. Hoffler, K. M. Kozloff, and S. A. Goldstein, “Spatial distribution of phosphate species in mature and newly generated mammalian bone by hyperspectral Raman imaging” *J. Biomed. Opt.*, vol. 4, no. 1, pp. 28–34, 1999.

[25] R. F. Egerton, “Electron energy-loss spectroscopy in the electron microscope” Springer Science & Business Media, 2011.

[26] P. Geladi and H. F. Grahn, “Multivariate image analysis” Wiley Online Library, 1996.

[27] H. Grahn and P. Geladi, “Techniques and applications of hyperspectral image analysis” John Wiley & Sons, 2007.

[28] P. W. T. Krooshof, G. J. Postma, W. J. Melssen, and L. M. C. Buydens, “Evaluation of Spectroscopic Images” *Biomed. Imaging Princ. Appl.*, p. 1, 2012.

[29] T. N. Tran, R. Wehrens, and L. M. C. Buydens, “Clustering multispectral images: a tutorial” *Chemom. Intell. Lab. Syst.*, vol. 77, no. 1, pp. 3–17, 2005.

[30] A. Huber, “Nanoscale surface-polariton spectroscopy by mid-and far-infrared near-field microscopy” TU Munich, 2009.

[31] N. Ocelic, “Quantitative near-field phonon-polariton spectroscopy” TU Munich, 2007.

[32] J. M. Stiegler, “Infrared spectroscopic near-field microscopy of nanoparticles and semiconductor nanowires” University of the Basque Country, 2012.

[33] I. Amenabar, “Infrared near-field imaging and near-field spectroscopy of biological nanostructures” 2013.

[34] L. Novotny and B. Hecht, “Principles of Nano-Optics” Cambridge University Press, 2006.

[35] E. Meyer, H. J. Hug, and R. Bennewitz, “Scanning probe microscopy: the lab on a tip” Springer, 2004.

[36] E. A. Ash and G. Nicholls, “Super-resolution aperture scanning microscope” *Nature*, vol. 237, pp. 510–512, 1972.

[37] B. Hecht, B. Sick, U. P. Wild, V. Deckert, R. Zenobi, O. J. F. Martin, and D. W. Pohl, “Scanning near-field optical microscopy with aperture probes: Fundamentals and applications” *J. Chem. Phys.*, vol. 112, no. 18, pp. 7761–7774, 2000.

[38] T. Taubner, R. Hillenbrand, and F. Keilmann, “Performance of visible and mid-infrared scattering-type near-field optical microscopes” *J. Microsc.*, vol. 210, pp. 311–314, 2003.

[39] R. Hillenbrand, T. Taubner, and F. Keilmann, “Phonon-enhanced light--matter interaction at the nanometre scale” *Nature*, vol. 418, no. 6894, pp. 159–162, 2002.

[40] F. Keilmann, A. J. Huber, and R. Hillenbrand, “Nanoscale conductivity contrast by scattering-type near-field optical microscopy in the visible, infrared and THz domains” *J. Infrared, Millimeter, Terahertz Waves*, vol. 30, no. 12, pp. 1255–1268, 2009.

[41] A. J. Huber, F. Keilmann, J. Wittborn, J. Aizpurua, and R. Hillenbrand, “Terahertz Near-Field Nanoscopy of Mobile Carriers in Single Semiconductor Nanodevices” *Nano Lett.*, vol. 8, no. 11, pp. 3766–3770, 2008.

[42] F. Keilmann and R. Hillenbrand, “Near-field microscopy by elastic light scattering from a tip”, vol. 362, no. 1817. 2004.

[43] F. Huth, M. Schnell, J. Wittborn, N. Ocelic, and R. Hillenbrand, “Infrared-spectroscopic nanoimaging with a thermal source” *Nat. Mater.*, vol. 10, no. 5, pp. 352–6, 2011.

[44] F. Keilmann and R. Hillenbrand, “Nano-Optics and Near-Field Optical Microscopy” Artech House, Boston/London, 2008.

[45] P. Schunk, “Untersuchung von Oberflächen und Oberflächenprozessen mit dem Rasterkraftmikroskop” Universität Karlsruhe (TH), 1998.

[46] M. Salerno, J. R. Krenn, B. Lamprecht, G. Schnider, H. Ditlbacher, N. Felidj, A. Leitner, and F. R. Aussenegg, “Plasmon polaritons in metal nanostructures: the optoelectronic route to nanotechnology” *Optoelectron. Rev.*, vol. 10, pp. 217–224, 2002.

[47] J. R. Krenn and J. C. Weeber, “Surface Plasmon polaritons in metal stripes and wires” *Philos. Trans. R. Soc. London, Ser. A*, vol. 362, pp. 739–756, 2004.

[48] N. Ocelic, A. Huber, and R. Hillenbrand, “Pseudoheterodyne detection for background-free near-field spectroscopy” *Appl. Phys. Lett.*, vol. 89, no. 10, 2006.

[49] B. Knoll and F. Keilmann, “Enhanced dielectric contrast in scattering-type scanning near-field optical microscopy” *Opt. Commun.*, vol. 182, pp. 321–328, 2000.

[50] R. Hillenbrand, B. Knoll, and F. Keilmann, “Pure optical contrast in scattering-type scanning near-field optical microscopy” *J. Microsc.*, vol. 202, pp. 77–83, 2001.

[51] A. J. Huber, “Nanoscale Surface-polariton Spectroscopy by Mid-and Far-infrared Near-field Microscopy” Verein zur F{ö}rderung des Walter Schottky Inst. der

Techn. Univ. M{ü}nchen eV, 2011.

[52] M. Labardi, S. Patane, and M. Allegrini, "Artifact-free near-field optical imaging by apertureless microscopy" *Appl. Phys. Lett.*, vol. 77, no. 5, pp. 621–623, 2000.

[53] N. Ocelic, A. Huber, and R. Hillenbrand, "Pseudoheterodyne detection for background-free near-field spectroscopy" *Appl. Phys. Lett.*, vol. 89, no. 10, pp. 101124-1-101124–3, 2006.

[54] M. B. Raschke and C. Lienau, "Apertureless near-field optical microscopy: Tip--sample coupling in elastic light scattering" *Appl. Phys. Lett.*, vol. 83, no. 24, pp. 5089–5091, 2003.

[55] A. Cvitkovic, N. Ocelic, and R. Hillenbrand, "Analytical model for quantitative prediction of material contrasts in scattering-type near-field optical microscopy" *Opt. Express*, vol. 15, no. 14, p. 8550, 2007.

[56] S. Amarie, P. Zaslansky, Y. Kajihara, E. Griesshaber, W. W. Schmahl, and F. Keilmann, "Nano-FTIR chemical mapping of minerals in biological materials" *Beilstein J. Nanotechnol.*, vol. 3, pp. 312–323, 2012.

[57] F. Huth, A. Govyadinov, S. Amarie, W. Nuansing, F. Keilmann, and R. Hillenbrand, "Nano-FTIR Absorption Spectroscopy of Molecular Fingerprints at 20 nm Spatial Resolution" *Nano Lett.*, vol. 12, no. 8, pp. 3973–3978, 2012.

[58] F. Keilmann and S. Amarie, "Mid-infrared Frequency Comb Spanning an Octave Based on an Er Fiber Laser and Difference-Frequency Generation" *J. Infrared, Millimeter, Terahertz Waves*, vol. 33, no. 5, pp. 479–484, 2012.

[59] A. A. Govyadinov, I. Amenabar, F. Huth, P. S. Carney, and R. Hillenbrand, "Quantitative Measurement of Local Infrared Absorption and Dielectric Function with Tip-Enhanced Near-Field Microscopy" *J. Phys. Chem. Lett.*, vol. 4, pp. 1526–1531, 2013.

[60] S. Y. Venyaminov and N. N. Kalnin, "Quantitative IR spectrophotometry of peptide compounds in water (H2O) solutions .1. spectral parameters of amino-acid residue absorption-bands" *Biopolymers*, vol. 30, no. 13–14, pp. 1243–1257, 1990.

[61] M. Jackson and H. H. Mantsch, "The use and misuse of FTIR spectroscopy in the determination of protein-structure" *Crit. Rev. Biochem. Mol. Biol.*, vol. 30, no. 2, pp. 95–120, 1995.

[62] F. Garczarek and K. Gerwert, "Functional waters in intraprotein proton transfer monitored by FTIR difference spectroscopy" *Nature*, vol. 439, no. 7072, pp. 109–112, 2006.

[63] K. Ataka, T. Kottke, and J. Heberle, "Thinner, Smaller, Faster: IR Techniques To Probe the Functionality of Biological and Biomimetic Systems" *Angew. Chemie-International Ed.*, vol. 49, no. 32, pp. 5416–5424, 2010.

[64] S. C. Gupta, S. Prasad, J. H. Kim, S. Patchva, L. J. Webb, I. K. Priyadarsini, and B. B. Aggarwal, "Multitargeting by curcumin as revealed by molecular interaction studies" *Nat. Prod. Rep.*, vol. 28, no. 12, pp. 1937–1955, 2011.

[65] M. Mahmoudi, I. Lynch, M. R. Ejtehadi, M. P. Monopoli, F. B. Bombelli, and S. Laurent, "Protein-Nanoparticle Interactions: Opportunities and Challenges" *Chem. Rev.*, vol. 111, no. 9, pp. 5610–5637, 2011.

[66] P. Lasch, W. Haensch, D. Naumann, and M. Diem, “Imaging of colorectal adenocarcinoma using FT-IR microspectroscopy and cluster analysis” *Biochim. Biophys. Acta-Molecular Basis Dis.*, vol. 1688, no. 2, pp. 176–186, 2004.

[67] S. Caine, P. Heraud, M. J. Tobin, D. McNaughton, and C. C. A. Bernard, “The application of Fourier transform infrared microspectroscopy for the study of diseased central nervous system tissue” *Neuroimage*, vol. 59, no. 4, pp. 3624–3640, 2012.

[68] Z. Xia, X. Yu, and M. Wei, “Biomimetic collagen/apatite coating formation on Ti6Al4V substrates” *J. Biomed. Mater. Res. Part B-Applied Biomater.*, vol. 100B, no. 3, pp. 871–881, 2012.

[69] D. M. Byler and H. Susi, “Examination of the secondary structure of proteins by deconvolved FTIR spectra” *Biopolymers*, vol. 25, no. 3, pp. 469–487, 1986.

[70] M. Bouchard, J. Zurdo, E. J. Nettleton, C. M. Dobson, and C. V Robinson, “Formation of insulin amyloid fibrils followed by FTIR simultaneously with CD and electron microscopy” *Protein Sci.*, vol. 9, no. 10, pp. 1960–1967, 2000.

[71] C. Ritter, M. L. Maddelein, A. B. Siemer, T. Luhrs, M. Ernst, B. H. Meier, S. J. Saupe, and R. Riek, “Correlation of structural elements and infectivity of the HET-s prion” *Nature*, vol. 435, no. 7043, pp. 844–848, 2005.

[72] S. Amarie and F. Keilmann, “Broadband-infrared assessment of phonon resonance in scattering-type near-field microscopy” *Phys. Rev. B*, vol. 83, no. 4, p. 45404, 2011.

[73] X. J. G. Xu, M. Rang, I. M. Craig, and M. B. Raschke, “Pushing the Sample-Size Limit of Infrared Vibrational Nanospectroscopy: From Monolayer toward Single Molecule Sensitivity” *J. Phys. Chem. Lett.*, vol. 3, no. 13, pp. 1836–1841, 2012.

[74] M. Brehm, T. Taubner, R. Hillenbrand, and F. Keilmann, “Infrared spectroscopic mapping of single nanoparticles and viruses at nanoscale resolution” *Nano Lett.*, vol. 6, no. 7, pp. 1307–1310, 2006.

[75] G. wollny, E. Bruendermann, Z. Arsov, L. Quaroni, and M. Havenith, “Nanoscale depth resolution in scanning near-field infrared microscopy” *Opt. Express*, vol. 16, no. 10, pp. 7453–7459, 2008.

[76] F. Ballout, H. Krassen, I. Kopf, K. Ataka, E. Bruendermann, J. Heberle, and M. Havenith, “Scanning near-field IR microscopy of proteins in lipid bilayers” *Phys. Chem. Chem. Phys.*, vol. 13, no. 48, pp. 21432–21436, 2011.

[77] M. Paulite, Z. Fakhraai, I. T. S. Li, N. Gunari, A. E. Tanur, and G. C. Walker, “Imaging Secondary Structure of Individual Amyloid Fibrils of a β2-Microglobulin Fragment Using Near-Field Infrared Spectroscopy” *J. Am. Chem. Soc.*, vol. 133, no. 19, pp. 7376–7383, 2011.

[78] J. J. Li and C. M. Yip, “Super-resolved FT-IR spectroscopy: Strategies, challenges, and opportunities for membrane biophysics” *Biochim. Biophys. Acta*, Mar. 2013.

[79] E. C. Theil, R. K. Behera, and T. Tosha, “Ferritins for chemistry and for life” *Coord. Chem. Rev.*, vol. 257, no. 2, pp. 579–586, 2013.

[80] P. Ge and Z. H. Zhou, “Hydrogen-bonding networks and RNA bases revealed by cryo electron microscopy suggest a triggering mechanism for calcium switches”

Proc. Natl. Acad. Sci. U. S. A., vol. 108, no. 23, pp. 9637–9642, 2011.

[81] M. I. Ivanova, S. A. Sievers, M. R. Sawaya, J. S. Wall, and D. Eisenberg, "Molecular basis for insulin fibril assembly" *Proc. Natl. Acad. Sci. U. S. A.*, vol. 106, no. 45, pp. 18990–18995, 2009.

[82] R. Henderson and P. N. T. Unwin, "Three-Dimensional model of Purple Membrane obtained by electron-microscopy" *Nature*, vol. 257, no. 5521, pp. 28–32, 1975.

[83] D. Oesterhelt and W. Stoeckenius, "Isolation of the cell membrane of Halobacterium halobium and its fractionation into red and purple membrane" *Methods Enzymol.*, vol. 31, pp. 667–678, 1974.

[84] O. M. Selivanova and O. V Galzitskaya, "Structural polymorphism and possible pathways of amyloid fibril formation on the example of insulin protein" *Biochemistry-Moscow*, vol. 77, no. 11, pp. 1237–1247, 2012.

[85] S. Mastel, A. A. Govyadinov, T. V. A. G. de Oliveira, I. Amenabar, and R. Hillenbrand, "Nanoscale-resolved chemical identification of thin organic films using infrared near-field spectroscopy and standard Fourier transform infrared references" *Appl. Phys. Lett.*, vol. 106, no. 2, p. 23113, 2015.

[86] K. J. Rothschild and N. A. Clark, "Polarized infrared spectroscopy of oriented purple membrane" *Biophys. J.*, vol. 25, no. 3, pp. 473–487, 1979.

[87] X. Jiang, E. Zaitseva, M. Schmidt, F. Siebert, M. Engelhard, R. Schlesinger, K. Ataka, R. Vogel, and J. Heberle, "Resolving voltage-dependent structural changes of a membrane photoreceptor by surface-enhanced IR difference spectroscopy" *Proc. Natl. Acad. Sci. U. S. A.*, vol. 105, no. 34, pp. 12113–12117, 2008.

[88] R. Salzer and H. W. Siesler, "Infrared and Raman spectroscopic imaging: Second, Completely Revised and Updated Edition" Wiley. com, 2014.

[89] J. L. Jimenez, E. J. Nettleton, M. Bouchard, C. V Robinson, C. M. Dobson, and H. R. Saibil, "The protofilament structure of insulin amyloid fibrils" *Proc. Natl. Acad. Sci. U. S. A.*, vol. 99, no. 14, pp. 9196–9201, 2002.

[90] T. Deckert-Gaudig and V. Deckert, "Tip-enhanced Raman scattering (TERS) and high-resolution bio nano-analysis-a comparison" *Phys. Chem. Chem. Phys.*, vol. 12, no. 38, pp. 12040–12049, 2010.

[91] D. Kurouski, T. Deckert-Gaudig, V. Deckert, and I. K. Lednev, "Structure and Composition of Insulin Fibril Surfaces Probed by TERS" *J. Am. Chem. Soc.*, vol. 134, no. 32, pp. 13323–13329, 2012.

[92] R. Khurana, C. Ionescu-Zanetti, M. Pope, J. Li, L. Nielson, M. Ramirez-Alvarado, L. Regan, A. L. Fink, and S. A. Carter, "A general model for amyloid fibril assembly based on morphological studies using atomic force microscopy" *Biophys. J.*, vol. 85, no. 2, pp. 1135–1144, 2003.

[93] S. Guo and B. B. Akhremitchev, "Packing density and structural heterogeneity of insulin amyloid fibrils measured by AFM nanoindentation" *Biomacromolecules*, vol. 7, no. 5, pp. 1630–1636, 2006.

[94] S. L. G. and A. M. S. Jose C. Rodríguez-Pérez, Ian W. Hamley, "Local orientational disorder in peptide fibrils probed by a combination of residue-

specific 13C-18O labelling, polarised infrared spectroscopy and molecular combing" *Chem. Commun.*, vol. 48, no. 97, pp. 11835–11837, Dec. 2012.

[95] C. M. Cheatum, A. Tokmakoff, and J. Knoester, "Signatures of beta-sheet secondary structures in linear and two-dimensional infrared spectroscopy" *J. Chem. Phys.*, vol. 120, no. 17, pp. 8201–15, May 2004.

[96] W. Dzwolak, A. Loksztejn, and V. Smirnovas, "New Insights into the Self-Assembly of Insulin Amyloid Fibrils : An H-D" *Biochemistry*, no. 45, pp. 8143–8151, 2006.

[97] L. Nielsen, S. Frokjaer, J. F. Carpenter, and J. Brange, "Studies of the structure of insulin fibrils by Fourier transform infrared (FTIR) spectroscopy and electron microscopy" *J. Pharm. Sci.*, vol. 90, no. 1, pp. 29–37, Jan. 2001.

[98] G. T. Webster, J. Dusting, S. Balabani, and E. W. Blanch, "Detecting the Early Onset of Shear-Induced Fibril Formation of Insulin in situ" *J. Phys. Chem. B*, vol. 115, pp. 2617–2626, 2011.

[99] F. Huth, A. Chuvilin, M. Schnell, I. Amenabar, R. Krutokhvostov, S. Lopatin, and R. Hillenbrand, "Resonant antenna probes for tip-enhanced infrared near-field microscopy" *Nano Lett.*, vol. 13, no. 3, pp. 1065–1072, 2013.

[100] A. Fragola, L. Aigouy, P. Y. Mignotte, F. Formanek, and Y. De Wilde, "Apertureless scanning near-field fluorescence microscopy in liquids" *Ultramicroscopy*, vol. 101, no. 2–4, pp. 47–54, 2004.

[101] C. Hoppener, J. P. Siebrasse, R. Peters, U. Kubitscheck, and A. Naber, "High-resolution near-field optical imaging of single nuclear pore complexes under physiological conditions" *Biophys. J.*, vol. 88, no. 5, pp. 3681–3688, 2005.

[102] R. Hillenbrand, T. Taubner, and F. Keilmann, "Phonon-enhanced light-matter interaction at the nanometre scale" *Nature*, vol. 418, no. 6894, pp. 159–162, 2002.

[103] J. M. Hoffmann, B. Hauer, and T. Taubner, "Antenna-enhanced infrared near-field nanospectroscopy of a polymer" *Appl. Phys. Lett.*, vol. 101, no. 19, p. 193105, 2012.

[104] A. J. Huber, J. Wittborn, and R. Hillenbrand, "Infrared spectroscopic near-field mapping of single nanotransistors" *Nanotechnology*, vol. 21, no. 23, p. 235702, 2010.

[105] J. M. Stiegler, A. J. Huber, S. L. Diedenhofen, J. Gómez Rivas, R. E. Algra, E. P. A. M. Bakkers, and R. Hillenbrand, "Nanoscale free-carrier profiling of individual semiconductor nanowires by infrared near-field nanoscopy" *Nano Lett.*, vol. 10, no. 4, pp. 1387–1392, 2010.

[106] T. Taubner, R. Hillenbrand, and F. Keilmann, "Nanoscale polymer recognition by spectral signature in scattering infrared near-field microscopy" *Appl. Phys. Lett.*, vol. 85, no. 21, pp. 5064–5066, 2004.

[107] B. Pollard, E. A. Muller, K. Hinrichs, and M. B. Raschke, "Vibrational nano-spectroscopic imaging correlating structure with intermolecular coupling and dynamics" *Nat. Commun.*, vol. 5, p. 3587, 2014.

[108] A. C. Jones and M. B. Raschke, "Thermal infrared near-field optical spectroscopy" *Nano Lett.*, vol. 12, no. 3, pp. 1475–1481, 2012.

[109] H. a Bechtel, E. a Muller, R. L. Olmon, M. C. Martin, and M. B. Raschke, "Ultrabroadband infrared nanospectroscopic imaging" *Proc. Natl. Acad. Sci. U. S. A.*, vol. 111, no. 20, pp. 7191–6, May 2014.

[110] P. Hermann, A. Hoehl, G. Ulrich, C. Fleischmann, A. Hermelink, B. Kästner, P. Patoka, A. Hornemann, B. Beckhoff, E. Rühl, and G. Ulm, "Characterization of semiconductor materials using synchrotron radiation-based near-field infrared microscopy and nano-FTIR spectroscopy" *Opt. Express*, vol. 22, no. 15, pp. 17948–58, 2014.

[111] E. A. Muller, B. Pollard, H. A. Bechtel, P. van Blerkom, and M. B. Raschke, "Infrared Vibrational Nano-Crystallography and Nano-Imaging" *Sci. Adv.*, vol. 2, no. 10, p. e1601006, 2016.

[112] I. Amenabar, S. Poly, W. Nuansing, E. H. Hubrich, A. A. Govyadinov, F. Huth, R. Krutokhvostov, L. Zhang, M. Knez, J. Heberle, A. M. Bittner, and R. Hillenbrand, "Structural analysis and mapping of individual protein complexes by infrared nanospectroscopy" *Nat. Commun.*, vol. 4, p. 2890, Dec. 2013.

[113] J. Wueppen, B. Jungbluth, T. Taubner, and P. Loosen, "Ultrafast tunable mid IR source" in *Infrared, Millimeter and Terahertz Waves (IRMMW-THz), 36th-International Conference, IEEE,* 2011, pp. 1–2.

[114] S. Bensmann, F. Gaußmann, M. Lewin, J. Wüppen, S. Nyga, C. Janzen, B. Jungbluth, and T. Taubner, "Near-field imaging and spectroscopy of locally strained GaN using an IR broadband laser" *Opt. Express*, vol. 22, no. 19, pp. 22369–22381, 2014.

[115] X. G. Xu, M. Rang, I. M. Craig, and M. B. Raschke, "Pushing the sample-size limit of infrared vibrational nanospectroscopy: From monolayer toward single molecule sensitivity" *J. Phys. Chem. Lett.*, vol. 3, no. 13, pp. 1836–1841, 2012.

[116] S. Amarie, T. Ganz, and F. Keilmann, "Mid-infrared near-field spectroscopy" *Opt. Express*, vol. 17, no. 24, pp. 21794–21801, 2009.

[117] X. G. Xu and M. B. Raschke, "Near-field Infrared Vibrational Dynamics and Tip-Enhanced Decoherence" *Nano Lett.*, vol. 13, pp. 1588–1595, 2013.

[118] W. Herres and J. Gronholz, "Understanding FT-IR data processing" *Part*, vol. 1, pp. 352–356, 1984.

[119] B. S. Salmons, D. R. Katz, and M. L. Trawick, "Correction of distortion due to thermal drift in scanning probe microscopy" *Ultramicroscopy*, vol. 110, no. 4, pp. 339–349, 2010.

[120] V. Mazet, C. Carteret, D. Brie, J. Idier, and B. Humbert, "Background removal from spectra by designing and minimising a non-quadratic cost function" *Chemom. Intell. Lab. Syst.*, vol. 76, no. 2, pp. 121–133, 2005.

[121] P. Lasch, "Spectral pre-processing for biomedical vibrational spectroscopy and microspectroscopic imaging" *Chemom. Intell. Lab. Syst.*, vol. 117, pp. 100–114, 2012.

[122] T. Steinle, F. Mörz, A. Steinmann, and H. Giessen, "Ultra-stable high average power femtosecond laser system tunable from 1 . 33 to 20 μ m" *Opt. Lett.*, vol. 41, no. 21, pp. 4863–4866, 2016.

[123] M. J. Baker, J. Trevisan, P. Bassan, R. Bhargava, H. J. Butler, K. M. Dorling, P.

R. Fielden, S. W. Fogarty, N. J. Fullwood, K. A. Heys, and others, “Using Fourier transform IR spectroscopy to analyze biological materials” *Nat. Protoc.*, vol. 9, no. 8, pp. 1771–1791, 2014.

[124] C. Huang and L. Zhang, “Miscibility of Poly (vinylidene fluoride) and Atactic Poly (methyl methacrylate)” *J. Appl. Electrochem.*, vol. 92, no. 1, pp. 1–5, 2004.

[125] E. Fekete, E. Földes, and B. Pukánszky, “Effect of molecular interactions on the miscibility and structure of polymer blends” *Eur. Polym. J.*, vol. 41, no. 4, pp. 727–736, 2005.

[126] T. Inoue, “Morphology of polymer blends” in *Polymer Blends Handbook*, Springer, 2003, pp. 547–576.

[127] K. Kaniappan and S. Latha, “Certain investigations on the formulation and characterization of polystyrene/poly(methyl methacrylate) blends” *Int. J. ChemTech Res.*, vol. 3, no. 2, pp. 708–715, 2011.

[128] M. Brenner and V. J. Hearing, “The protective role of melanin against UV damage in human skin” *Photochem. Photobiol.*, vol. 84, no. 3, pp. 539–549, 2008.

[129] C. Marcott, M. Lo, K. Kjoller, F. Fiat, N. Baghdadli, G. Balooch, and G. S. Luengo, “Localization of human hair structural lipids using nanoscale infrared spectroscopy and imaging” *Appl. Spectrosc.*, vol. 68, no. 5, pp. 564–569, 2014.

[130] J. Ihssen, A. Braun, G. Faccio, K. Gajda-Schrantz, and L. Thöny-Meyer, “Light harvesting proteins for solar fuel generation in bioengineered photoelectrochemical cells” *Curr. Protein Pept. Sci.*, vol. 15, no. 4, p. 374, 2014.

[131] Y. Liu, V. R. Kempf, J. Brian Nofsinger, E. E. Weinert, M. Rudnicki, K. Wakamatsu, S. Ito, and J. D. Simon, “Comparison of the structural and physical properties of human hair eumelanin following enzymatic or acid/base extraction” *Pigment cell Res.*, vol. 16, no. 4, pp. 355–365, 2003.

[132] Y. Liu, L. Hong, K. Wakamatsu, S. Ito, B. Adhyaru, C.-Y. Cheng, C. R. Bowers, and J. D. Simon, “Comparison of structural and chemical properties of black and red human hair melanosomes” *Photochem. Photobiol.*, vol. 81, no. 1, pp. 135–144, 2005.

[133] J. Feng, M. A. Winnik, R. R. Shivers, and B. Clubb, “Polymer blend latex films: morphology and transparency” *Macromolecules*, vol. 28, no. 23, pp. 7671–7682, 1995.

[134] M. M. Coleman and P. C. Painter, “Hydrogen bonded polymer blends” *Prog. Polym. Sci.*, vol. 20, no. 1, pp. 1–59, 1995.

[135] C. Leonard, J. L. Halary, and L. Monnerie, “Crystallization of poly (vinylidene fluoride)-poly (methyl methacrylate) blends: analysis of the molecular parameters controlling the nature of poly (vinylidene fluoride) crystalline phase” *Macromolecules*, vol. 21, no. 10, pp. 2988–2994, 1988.

[136] S. Mohamadi, “Preparation and Characterization of PVDF/PMMA/Graphene Polymer Blend Nanocomposites by Using ATR-FTIR Technique” in *Infrared Spectroscopy-Materials Science, Engineering and Technology*, T. Theophanides, Ed. InTech, Chapters published, 2012, pp. 213–232.

[137] R. J. Sturgeon, “A re-investigation of the borohydride reduction of carbohydrates” *Carbohydr. Res.*, vol. 227, pp. 375–377, 1992.

[138] G. W. Milligan and M. C. Cooper, “An examination of procedures for determining the number of clusters in a data set” *Psychometrika*, vol. 50, no. 2, pp. 159–179, 1985.

[139] S. Sato, Y. Sasaki, A. Adachi, and T. Omi, “Reduction and Block Staining of Human Hair Shafts and Insect Cuticles by Ammonium Thioglycolate to Enhance Transmission Electron Microscopic Observations” *J. Cosmet. Dermatological Sci. Appl.*, 2013.

[140] M. G. Bridelli and P. R. Crippa, “Infrared and water sorption studies of the hydration structure and mechanism in natural and synthetic melanin” *J. Phys. Chem. B*, vol. 114, no. 29, pp. 9381–9390, 2010.

[141] T. Taubner, F. Keilmann, and R. Hillenbrand, “Nanoscale-resolved subsurface imaging by scattering-type near-field optical microscopy” *Opt. Express*, vol. 13, pp. 8893–8899, 2005.

10 Own Publications

Presented in this thesis:

1 **I. Amenabar**, S. Poly, W. Nuansing, E. H. Hubrich, A. A. Govyadinov, F. Huth, R. Krutokhvostov, L. Zhang, M. Knez, J. Heberle, A. M. Bittner, and R. Hillenbrand, "Structural analysis and mapping of individual protein complexes by infrared nanospectroscopy" *Nat. Commun.*, vol. 4, p. 2890, Dec. 2013.

(Chapter 6)

2 **I. Amenabar**, S. Poly, M. Goikoetxea, W. Nuansing, P. Lasch, and R. Hillenbrand, "Hyperspectral infrared nanoimaging of organic samples based on Fourier transform infrared nanospectroscopy" *Nat. Commun.*, vol. 8, 2017.
(Chapter 7 and chapter 8)

Related publications:

3 F. Huth, A. Chuvilin, M. Schnell, **I. Amenabar**, R. Krutokhvostov, S. Lopatin, and R. Hillenbrand, "Resonant antenna probes for tip-enhanced infrared near-field microscopy" Nano Lett., vol. 13, no. 3, pp. 1065–1072, 2013.

4 A. A. Govyadinov, **I. Amenabar**, F. Huth, P. S. Carney, and R. Hillenbrand, "Quantitative Measurement of Local Infrared Absorption and Dielectric Function with Tip-Enhanced Near-Field Microscopy" J. Phys. Chem. Lett., vol. 4, pp. 1526–1531, 2013.

5 S. Mastel, A. A. Govyadinov, T. V. A. G. de Oliveira, **I. Amenabar**, and R. Hillenbrand, "Nanoscale-resolved chemical identification of thin organic films using infrared near-field spectroscopy and standard Fourier transform infrared references" Appl. Phys. Lett., vol. 106, no. 2, p. 23113, 2015.

11 Acknowledgments

I want to express my gratitude to my supervisor Prof. Rainer Hillenbrand, group leader of the NanoOptics group at CIC NanoGUNE, for giving me the opportunity to join his group, for being so enthusiastic about my conducted projects and for being such a transparent person and supervisor.

I thank Prof. Txema Pitarke, director of CIC NanoGUNE, for giving me the opportunity to perform world-class nanoscience research under my PhD thesis at CIC NanoGUNE.

I am thankful to all present and past members of the NanoOptics group at NanoGUNE, for interesting and helpful discussions and the great atmosphere in the group. Special thanks to Florian Huth, who was my particular teacher and introduced me to the exciting field of near-field optics, providing comprehensive explanations every single time without hesitating. Many thanks also to Dr. Simon Poly (for sample preparation and valuable discussions about biology), to Dr. Wiwat Nuansing (for sample preparation and FTIR measurements), to Dr. Monika Goikoetxea (for sample preparation and helpful scientific discussion on polymers), to Dr. Alexander A. Govyadinov "Sasha" (for the theoretical support) and to Prof. Alex Bittner (for valuable scientific discussions).

I also want to thank all collaborators, especially Peter Lasch and Elmar H. Hubrich, who contributed to the projects within this thesis.

Thanks to NeaSpec for their continuous support on the NeaSNOM microscope.

I also want to thank all members of NanoGUNE for the great environment and for making of NanoGUNE something more than just a working place. Especially to those of you that are not work colleagues any more, but simply friends.

Finally, I would like to thank my family for supporting me in the decision of redirecting my professional career by making this PhD thesis in optics. Very special thanks to Esti for supporting me and for being by my side during almost the whole thesis.